INVESTIGATION OF THE DYNAMICS OF SOLID STATE LASER CRYSTALS

By

MICHAEL L. KLIEWER

Bachelor of Science in Mechanical Engineering
Oklahoma State University
Stillwater, Oklahoma
1983

Master of Science
Oklahoma State University
Stillwater, Oklahoma
1986

Submitted to the Faculty of the
Graduate College of the
Oklahoma State University
in partial fulfillment of
the requirements for
the Degree of
DOCTOR OF PHILOSOPHY
December, 1989

INVESTIGATION OF THE DYNAMICS OF
SOLID STATE LASER CRYSTALS

Thesis Approved:

Richard W. Powell
Thesis Adviser

Larry E. Hallibuton

James P. Wicksted

Richard L. Lowery

Chris McKinstry

Norman N. Durham
Dean of the Graduate College

ACKNOWLEDGMENTS

I would like to express my gratitude to all the people responsible for helping me during my studies at Oklahoma State University and for assisting me in the completion of my thesis. Foremost among these is my adviser, Dr. Richard C. Powell. Dr. Powell gave me the opportunity to work under him in a research assistantship. His instruction, advice, support, and patience proved invaluable throughout my graduate studies. He has been an excellent adviser, committee member, and a good friend. I would also like to thank the other members of my committee, Dr. Larry Haliburton, Dr. Richard Lowery, Dr. Steve McKeever, and Dr. Jim Wicksted. Special thanks are extended to my friends, Mike Scripsick, Dr. Andrzej Suchoki, Major Francis (Rudy) Valentino, Guy Gilliland, Greg Quarles, Roger Reeves, Eddie Behrens, Mark Petrovic, Keith VerSteeg, Faqir Hashmi, Mahendra Jani, and Mike Ferry, for their assistance and friendship and for sharing their knowledge through insightful discussions. I would like to thank Dr. Larry DeShazer for sharing his knowledge and enthusiasm and showing me how exciting the field of physics can be. I am also appreciative to Eddie Behrens, Mark Petrovic, Scott McCollum, Juan Ortiz, and Harold Walters for their assistance with $\LaTeX$ for the preparation of this manuscript.

My thanks and love go to my parents, my brother, and all of my family for their love, support, and understanding throughout my life, and especially while attending Oklahoma State University. Finally, and most of all, I thank God for blessing me with a healthy body and mind, and for always being there when I need Him.

Financial support was provided by the U.S. Army Research Office and NASA Langley Research Center.

TABLE OF CONTENTS

LIST OF TABLES

Table Page

LIST OF FIGURES

CHAPTER I

INTRODUCTION

For the past two decades the development and use of lasers in areas of medicine, engineering, science, and entertainment have expanded rapidly. Since the invention of the laser, lasers have been used as a tool to better understand the interaction between electromagnetic radiation and matter. More specifically, the use of lasers has provided a better understanding of the spectroscopic properties of solids, including the study of the effect of picosecond pulses on solid-state materials, energy migration, multiphoton and multiphonon processes, and the effect of hosts on the energy levels of impurity ions. Characterizing these properties and processes is important from both a basic science and an engineering viewpoint. Obtaining information about the basic physical properties of solids leads to a better understanding of the material and to more innovative solutions to engineering and technological problems. The work presented in this study discusses the use of laser spectroscopy and laser pumping of solid-state laser materials to better characterize the optical properties of solids.

Statement of Problem

With the increased demand for tunable solid-state lasers with specific properties, it is imperative to have techniques avaliable for efficiently evaluating the laser potential for a great number of samples. The parameters for evaluation are the pumping threshold for the onset of stimulated emission, the population inversion density at threshold, the stimulated emision cross section, and the gain

parameter [1]. Since the fundamental physical process of interest is stimulated emission of radiation, the evaluation techniques involve measuring the effects of stimulated emission on the optical spectra of the material. The observable effects include optical gain, a change in the spectral shape of a transmitted beam, and a decrease in the emission time of the radiation.

The most common technique used in material evaluation of this type is measuring the single-pass gain at the peak of the spectral transition. This is the most direct measurement of the stimulated emission properties of the material and works well with large samples having high optical quality and well-polished AR coated surfaces. If zero-phonon lines are observed, the peak stimulated emission cross section and inversion population density at threshold can be determined from the measured peak gain and pumping threshold energy. In some materials with broad vibronic emission bands favorable for tunable solid-state lasers, no zero-phonon lines are observable and the lack of reciprocity between absorption and emission transitions makes peak gain analysis more difficult. For these cases, fitting the spectral shape of the measured gain curve with the predictions of vibronic laser theory can be used to determine the desired stimulated emission parameters. The accuracy of the results of this type of analysis is affected by the sample quality mentioned above in addition to other material properties affecting the spectral band shape. Lifetime shortening measurements should provide similar information concerning stimulated emission properties without the results being adversely affected by sample size and quality. However, methods for analyzing lifetime shortening data to obtain this information are not as well developed and this technique has not been widely used as a quantitative method for laser material evaluation.

In addition to finding techniques for effectively evaluating the laser potential of a large number of samples, it is also important to find vibronic solid-state laser materials that will span the visible and near-infrared regions of the spectrum. Solid-state materials possess the durability needed for many space and military applications. The spectra of transition metal ions are greatly influenced by the host material and this would be the most reasonable place to begin the investigation.

Titanium is a very promising impurity ion for solid-state laser materials and varying the host may improve desirable characteristics such as tunability and laser efficiency. Other transition metal ions doped into the appropriate host materials may also result in the desired spectra and lasing characteristics.

If suitable hosts for transition metals ions cannot be found, it becomes important to improve the efficiency of existing lasers. One method of improving efficiencies is to increase the efficiency of pumping the materials by co-doping the material with another impurity which has better absorption of the pump wavelength. Chromium has a good match between its absorption spectrum and the emission spectrum of flash lamps used to pump many solid-state lasers. By carefully choosing the host material it is possible to shift the emission to a wavelength where energy transfer can occur between the chromium and another impurity ion. If the energy transfer is efficient, it becomes feasible to more efficiently pump the lasing impurities in these materials.

Another way of improving the efficiency of laser materials is to identify and eliminate any losses in the material. Some losses that have been identified in the past are absorption in the lasing spectral region as is the case in Ti:Sapphire and the introduction of impurities and stresses in the material which would increase scattering and thermal damage. Growth techniques are constantly being refined to eliminate these losses mentioned above. Additional complications arise if these and other losses cannot be eliminated or at least minimized with modified crystal growth techniques. It is important to find all loss mechanisms and thus obtain the most efficient solid-state laser material possible.

Summary of Thesis

Chapter II is a comparison of methods used in evaluating materials as tunable vibronic lasers. The three techniques used for determining the effects of stimulated emission on the spectra of solid-state vibronic laser materials are peak single-pass gain, fluorescence band narrowing, and lifetime shortening. Each of these was used to obtain the pump energy density and population inversion at

threshold, the stimulated emission cross section, and the gain coefficient for two potential vibronic laser materials. The difficulty and accuracy of each technique is discussed. Lifetime shortening results were analyzed by using numerical techniques to solve the coupled set of rate equations describing the concentration of photons and population of excited states of ions in an optically pumped material under δ-function pulsed excitation. The solutions predict an effective shortening of the fluorescence lifetime at high excitation levels with a distinct threshold where stimulated emission processes become important. The observed band narrowing for the same type of pumping conditions is shown to be consistent with the theoretical predictions of the model developed by McCumber.

Chapter III contains a comparison of three different potential solid state laser materials: Ti:Al_2O_3, Ti:$BeAl_2O_3$, and Ti:$BaTiAl_6O_{12}$. The spectral properties of each material were examined, and the absorption and fluorescence of titanium in each host is very similar. One difference that was noted was the observance of the no-phonon lines. In Ti:Sapphire, two zero-phonon lines originating from the ^2E level were observed, in Ti:Chrysoberyl a single zero-phonon line was observed, and in Ti:BA no zero-phonon lines were detected. The temperature dependence of the lifetime of the fluorescence and the zero-phonon lines were examined and the configuration coordinate diagram was constructed. A shortening of the fluorescence lifetime in Ti:Chrysoberyl under high pumping conditions was seen. A threshold value for the pump power of 0.224 J/cm^3 for stimulated emission was determined. Ti:BA has a low damage threshold, making lifetime shortening impossible to obtain and its use as a solid state laser material impractical.

Chapter IV looks at the growth and characterization of materials for tunable lasers in the near infrared spectral region. In particular $LiNbO_3$ was examined as a laser host material for transition metal ions. Magnesium was doped into the materials at a concentrantion of greater than 4.5 % to reduce optical damage effects and then either Ni^{2+}, Co^{2+}, or Cr^{3+} was doped into the material to hopefully provide a broad absorption and emission band. Room temperature fluorescence was only detected from $LiNbO_3$:MgO,Cr^{3+} and attempts to lase this material failed

due to slow heat dissipation in the material and subsequent thermal damage to the material before laser threshold could be achieved.

In Chapter V the energy transfer from Cr^{3+} doped into $LiNbO_3$:MgO to rare earth ions is investigated. The broad absorption band of Cr^{3+} ion $LiNbO_3$ is ideal for flashlamp pumping and the spectrally narrow emission lines of the rare earth ions are good for laser emission. Energy transfer from the Cr^{3+} to Tm^{3+}, Ho^{3+}, Nd^{3+}, and Er^{3+} was not observed due to either too low a concentration of the rare earth ion or too small an overlap between absorption of the rare earth and emission of Cr^{3+}. The energy transfer from chromium to ytterbium was observed and it was determined that the energy transfer is not efficient enough to effectively pump ytterbium as a lasing ion.

In chapter VI, the characteristics of optically pumping dynamics occurring in laser-pumped rare earth-doped, solid-state laser materials are discussed. A tunable alexandrite laser was used to pump $Y_3Al_5O_{12}$:Nd^{3+} in an optical cavity and the fluorescence and slope efficiencies were measured. It was found that the slope efficiency of the Nd-laser operation depends strongly on the wavelength of the pump laser. Excited state absorption of the pump photons was found to be the mechanism responsible and involves two types of transitions: resonant transitions originating on levels above the metastable state and non-resonant vibronic transitions originating on the metastable state. A model has been developed to explain the observed variation in the slope efficiencies with pump wavelength and theoretical fits of the experimental data provide information on the cross sections and rates of these transitions. This type of process will be an important loss mechanism for monochromatic pumping of laser systems at specific pump wavelengths.

Chapter VII presents the summary and conclusions for the material given in the thesis. Included in this chapter are suggestions for future work that needs to be undertaken to arrive at a better understanding of the physical properties taking place in solid-state laser materials. Finally, an appendix is included that gives a more complete development and summary of McCumber's theory for vibronic lasers.

CHAPTER II

EVALUATION OF MATERIALS FOR TUNABLE VIBRONIC LASERS

Introduction

In this section we discuss the use of the three techniques described in the evaluation of materials for vibronic laser applications. A comparison is given of the results obtained from the three types of measurements made in two different materials with vibronic emission bands. Emphasis is focused on the analysis of lifetime shortening data for obtaining information on stimulated emission.

The results of peak single-pass gain, band narrowing, and lifetime shortening measurements have been previously reported [2,3] on two different samples: $Li_6GE_8O_{19}$:Ti^{4+} and $RbCaF_3$:Rh^{2+}. A Nd:YAG laser with a mode-locked oscillator, single-pulse selector, amplifier stage, and frequency multiplication crystals was used as the pump source. This provides pulses with Gaussian profiles and durations of approximately 30 ps. The cross section of the pumped region of the samples was approximately 3.2 mm^2. For peak gain and band narrowing measurements the output of a tunable dye laser was used as a probe beam. For lifetime shortening measurements the emission was observed perpendicular to the excitation direction with a 0.25-m monochromator used to filter out scattered light and an RCA C31034 photomultiplier tube used for detection. The lifetimes were recorded by photographic traces on a storage oscilloscope. The relevant sample parameters are given in Table I.

As a check on the validity of the experimental results, it is useful to estimate the peak stimulated emission cross section from spectral parameters. For materials with a large Stokes shift between the absorption and the emission band,

TABLE I

SAMPLE PARAMETERS OF $RbCaF_3:Rh^{2+}$
AND $Li_6Ge_8O_{19}:Ti^{4+}$

Parameter	$RbCaF_3:Rh^{2+}$	$Li_6Ge_8O_{19}:Ti^{4+}$
N (cm^{-3})	2.5×10^{18}	1.5×10^{19}
σ_{21} (cm^2)	1.6×10^{-18}	2.0×10^{-20}
a_o (cm)	0.50	0.075
λ (nm)	710	442
$\Delta\lambda$ (nm)	15	100
μ (nm)	675	390
τ (μs)	9.0	9.0
n	1.4	1.7
τ_{st} ($cm^{-3}s$)	2.4×10^6	2.4×10^7

the stimulated emission cross section is given by

$$\sigma_{21} = (\frac{1}{4\pi^2 \tau_R \Delta\nu})(\frac{\lambda_{em}^3}{\lambda_{ab}})(\frac{g_u}{g_l n_{ab} n_{em}})(\frac{\mid M_{ab} \mid}{\mid M_{em} \mid})^2(\frac{\epsilon_{em}}{\epsilon_{ab}})^2, \quad (1)$$

where λ_{em} is the wavelength of the peak of the emission band and λ_{ab} is the wavelength of the peak of the absorption band; $\Delta\nu$ is the full width at half-maximum of the absorption band; n_{em} and n_{ab} are the indices of refraction of the material at emission and absorption, respectively; τ_R is the radiative lifetime of the material; g_u and g_l are the degeneracies of the upper and lower levels of the transitions; ϵ_{em} and ϵ_{ab} are the effective fields surrounding the ion in the host at the wavelength of the emission and absorption transitions; and M_{ab} and M_{em} are the matrix elements of the absorption and emission transitions. For zero-phonon lines $\lambda_{ab} = \lambda_{em}$, and Eq. (1) becomes the familiar expression for the emission cross section [1]. For the samples of interest to this work, no zero-phonon lines are observed, the shape of the absorption bands are distorted by the band edges of the host crystals, there are large Stokes shifts, and the quantum efficiencies are not known. However, Eq. (1) can still be used to obtain a crude estimate for σ_{21} by approximating the radiative lifetime by the measured fluorescence lifetime, approximating the halfwidth of the absorption band by the measured halfwidth of the emission band, assuming that the effective fields, refractive indices, and matrix elements are the same for absorption and emission wavelengths, and assuming that the degeneracies of the upper and lower levels of the transitions are equal. The emission cross sections estimated from spectral parameters in this way are listed in Table I.

Peak Single-Pass Gain

The gain of an active medium in the absence of any losses can be described as the difference between a stimulated emission term $e = N_2\sigma_{21}$ and an absorption term $\alpha = N_1\sigma_{12}$:

$$g(cm^{-1}) = e - \alpha, \quad (2)$$

where N_2 and N_1 are the total populations of the upper and lower states, respectively, and σ_{12} and σ_{21} are the cross sections for absorption and stimulated emission.

The gain characteristic g can be obtained from experimental measurements and is defined as

$$g(cm^{-1}) = \frac{\ln(1+G)}{d}, \tag{3}$$

where the gain G is defined as $G = (I_p - I_o)/I_o$, I_o is the intensity of the probe beam transmission passing through the unpumped material, I_p is the intensity of the probe beam transmission passing through the pumped material, and d is the length of the pumped region colinear with the probe beam.

The pumping threshold energy density E_{th} is measured by monitoring the spectral properties of the sample as a function of pump energy and determining the level at which the effects of stimulated emission are observed. For zero-phonon transitions between states with the same degeneracies, $\sigma_{21} = \sigma_{12}$. In this case the population inversion at threshold is given by [1]

$$\Delta N_{th} = \frac{E_{th}}{(h\nu)}, \tag{4}$$

where ν is the frequency of the pump photons. Thus measuring the peak gain and obtaining the population inversion through pumping energy threshold measurements allow the stimulated emission cross section to be found through the expression [1]

$$\sigma_{21} = \frac{g}{\Delta N_{th}}. \tag{5}$$

The situation is not as simple for materials exhibiting broadband vibronic emission. For large Stokes shifts the absorption and stimulated emission cross sections are no longer reciprocal and Eq. (2) must be solved for σ_{21} using the measured values for g, α, and N_2 at threshold. For good vibronic laser materials the absorption is negligible in the spectral region of the fluorescence emission and $N_1\sigma_{12}$ becomes negligible. Thus Eq. (2) yields

$$\sigma_{21} = \frac{g}{(N_2)_{th}}, \tag{6}$$

and Eq. (4) becomes

$$(N_2)_{th} = \frac{E_{th}}{h\nu}. \tag{7}$$

The results of single-pass gain and threshold measurements are listed in Table II. The emission cross section obtained from single pass gain measurements generally overestimates the cross section since it is difficult to insure that the measurement of the gain does not include some fluorescence. The accuracy of these measurements is also determined by the sample size and quality.

Band Narrowing

Another spectral change that occurs when stimulated emission processes become important is the narrowing of the emission band due to the frequency dependence of the gain curve [1]. In tunable vibronic laser materials this narrowing is due to both the intrinsic shape of the spectral transition and to the enhanced thermal population of the ground vibrational states due to the phonons emitted in the vibronic lasing process [4]. The spectral narrowing contribution due to frequency selective gain is significant only for high gains and reduced bandwidths are generally measurable only for peak gains of 3dB or more [1]. For the type of materials investigated in this work, the highest gain obtainable was only 1.05 dB, and thus this contribution to the band narrowing is negligible. Band narrowing due to enhanced population of the vibrational states of the ground state is the dominant process for these materials and can be described by McCumber's theory for phonon-terminated lasers [4–6]. The development of McCumber's theory for phonon terminated lasers is given in the Appendix.

For broadband spectra in which the emission bandwidth is large compared to kT, a generalization of the Einstein relations gives the following relation [5]:

$$\sigma_{12} = \sigma_{21} \exp\left[\hbar(\omega - \mu)/kT\right] \tag{8}$$

where μ is the energy of the zero-phonon line. The gain coefficient is then given by

$$g(\omega) = (N_2 - N_1 \exp\left[\hbar(\omega - \mu)/kT\right])\sigma_{21} \tag{9}$$

TABLE II

SPECTRAL PARAMETERS IN THE PRESENCE OF STIMULATED EMISSION

Parameter	Measurement Method		
	Single-Pass Gain	Band Narrowing	Lifetime Shortening
$RbCaF_3 : Rh^{2+}$			
$(N_2)_{th}(cm^{-3})$	3.0×10^{17}	2.6×10^{17}	2.4×10^{17}
$\sigma_{21}(cm^2)$	1.8×10^{-18}	1.2×10^{-18}	3.0×10^{-18}
$E_{th}(J/cm^3)$	0.17	0.15	0.14
g (cm^{-1})	0.54	0.54	0.83
$Li_6Ge_8O_{19} : Ti^{4+}$			
$(N_2)_{th}(cm^{-3})$	2.5×10^{18}	2.1×10^{18}	2.4×10^{18}
$\sigma_{21}(cm^2)$	1.7×10^{-19}	5.7×10^{-19}	2.5×10^{-19}
$E_{th}(J/cm^3)$	1.8	1.6	1.8
g (cm^{-1})	0.42	0.42	0.63

The stimulated emission cross section can be related to the fluorescence spectrum by

$$\sigma_{21} = f(\omega, \lambda) C_1 (\frac{2\pi c}{\omega n})^2, \tag{10}$$

where $f(\omega, \lambda)$ is the normalized fluorescence spectrum and the absolute strength of this spectrum is contained in C_1. $C_1 f(\omega, \lambda)$ is the fluorescence intensity in photons/s per unit frequency interval of radiation of polarization λ and frequency ω. Combining Eqs. (8), (9), and (10) yields McCumber's expression for the gain coefficient,

$$g(\omega) = A[p - (1-p)\exp[\hbar(\omega - \mu)/kT]] f(\omega, \lambda)/\omega^2, \tag{11}$$

where $p = N_2/(N_1 + N_2)$, and N_i is the population of the i^{th} level of a two-level atomic system. The constant A is given by $(2\pi c)^2 C_1 N/n^2$, where N is the total number of active atoms, and n is the index of refraction of the material. The magnitude of C_1 was estimated by relating it to the spontaneous emission lifetime through [4]

$$\tau^{-1} = (\frac{C_1}{2\pi}) \sum_{\lambda} \int_0^{4\pi} d\Omega \int_0^{\infty} f(\omega, \lambda) d\omega. \tag{12}$$

The ω^{-2} factor in Eq. (11) causes an asymmetric narrowing of the emission band in the presence of gain.

Treating p and μ as adjustable parameters and using the measured value of the fluorescence emission as a function of frequency, Eq. (11) was fit to the experimentally measured gain characteristic curves. An example of the best fit to one set of data is shown in Fig. 1 along with the fluorescence emission below threshold [3]. The parameters obtained from this fit are given in Table II. Changes in the values of p and μ move the peak of the gain curve, change the magnitude of the maximum gain, and greatly affect the slope of the gain curve on the high energy side. As the value of the zero-phonon line is moved to a higher energy the gain curve shifts to a higher energy, the peak gain increases, and the slope of the gain curve on the high energy side decreases. As the inversion parameter p increases, the gain curve shifts to a higher energy, the peak gain increases, and the slope of the gain curve on the high energy side increases. The slope of the

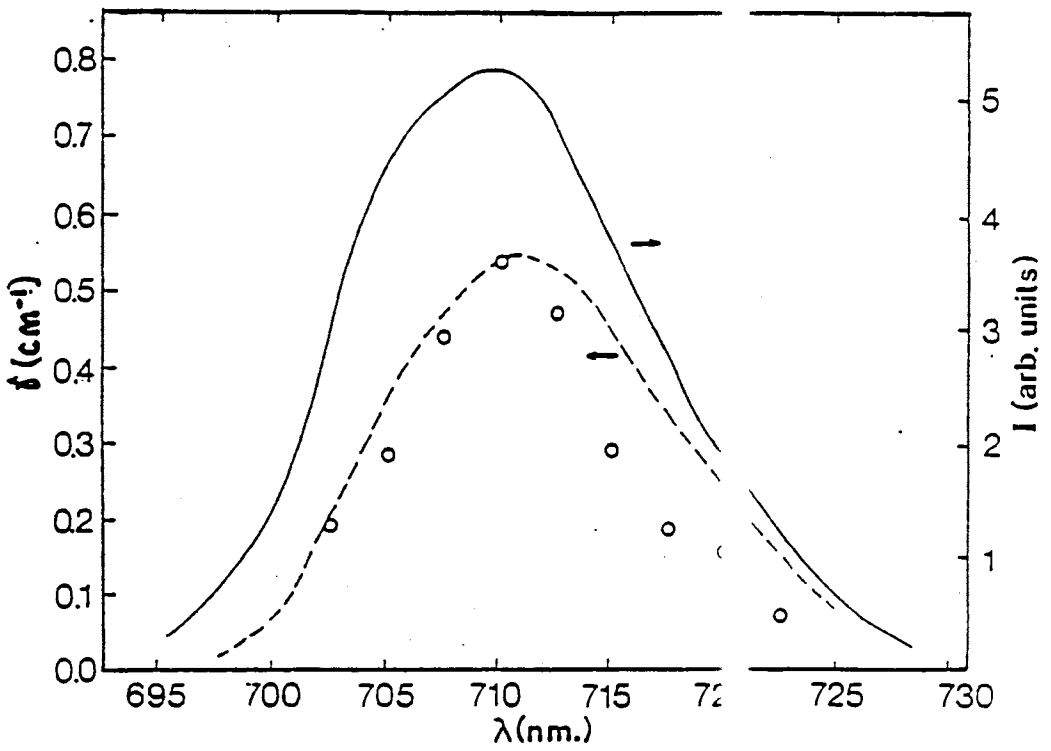

Figure 1. Fluorescence Band of $RbCaF_3:Rh^{2+}$ at L v Excitation Power

gain curve on the low energy side does not change significantly with changes in either the inversion parameter or the location of the zero-phonon line. A good fit is established when the predicted maximum in the gain curve corresponds with the experimentally measured maximum gain in both location and magnitude. The predicted values of gain agree with the measured values on the high energy side of the gain curve, but the predicted values are greater than observed on the low energy side. Spectral structures observed at low temperatures [7] indicate that this fluorescence is the superposition of more than one emission transition which may be the cause of a lack of good agreement between theory and experiment in this spectral region.

Using p obtained from the fit of the narrowed gain curve and the known value of N, the threshold population inversion was obtained. From the value of C_1 obtained from Eq. (12), the stimulated emission cross section can be determined using Eq. (10). The values of $(N_2)_{th}$ and σ_{21} at the peak of the band obtained in this way are listed in Table II. The peak stimulated emission cross sections from the band narrowing technique are in good agreement with those values obtained from Eq. (6). The values for the population inversion at threshold obtained from peak single-pass gain and band narrowing are also in good agreement.

Lifetime Shortening

If the fluorescence lifetime of a material is monitored while the pump power on the material is increased, an effective shortening of the fluorescence lifetime will be observed when the pump power is above the pumping threshold for stimulated emission to occur. This effect is referred to as amplified spontaneous emission (ASE) and it occurs when the spontaneous emission from a distribution of inverted ions is amplified by stimulated emission from these atoms without the benefit of a resonant cavity to provide feedback and mode structure. The lifetime of the atoms undergoing stimulated emission can be orders of magnitude less than the spontaneous lifetime and this short lifetime component becomes visible at a well-defined threshold value of the pump power. When the pump pulses are much

shorter than the fluorescence lifetime and the fluorescence lifetime is monitored at right angles to the input beam, the shortening of the fluorescence lifetime is seen as a spike occurring at the peak of the time evolution of the spontaneous emission and becomes more prominent as the pump power is increased.

In this approach to examining the effects of ASE in a mirrorless system, the dynamics of fluorescence emission in fast pumping conditions are measured and compared to the results of the solution of the rate equations describing a pumped two-level system with the inclusion of a term describing stimulated emission processes. By fitting the pump power threshold for lifetime shortening predicted by the rate equations to the experimentally observed values, the stimulated emission parameter can be determined. This paramenter can then be used to determine the stimulated emission cross section, the population inversion at threshold, and the gain of the material.

The more standard approach for studying the effects of ASE is to measure the transmission of a beam through the cylindrical region of an inverted medium and determine the contribution of ASE to the total intensity emerging from the medium [1,8]. If the stimulated emission parameter and the gain are known, the stimulated emission cross section can be determined. This approach is difficult to use with low gain materials due to the geometry of the ASE optical power flow. Because we are working with low gain and have no prior knowledge of the gain coefficient, this approach is not applicable in the work described here.

The spectral dynamics of a laser material including the prediction of lifetime shortening can be adequately described by a coupled set of rate equations establishing the relationship between the number of photons in the medium and the number of ions in the metastable state [9]. In using a single set of rate equations, longitudinal and radial variations of the radiation within the laser medium are ignored. This simplification does not significantly affect the solutions if a small, uniformly pumped sample is used. The solutions for these equations in cw pumping conditions are found in standard textbooks dealing with lasers [1]. To find the solutions of these equations for fast pumping conditions, a δ-function excitation

pulse is assumed. This approximation is simulated by assuming that the upper level of a two-level system is initially populated. The coupled rate equations then have the form

$$\frac{dN_2}{dt} = \frac{-N_2}{\tau_2} - \frac{N_2 P}{\tau_{st}}, \tag{13}$$

$$\frac{dP}{dt} = \frac{N_2 P}{\tau_{st}} + \frac{N_2}{\tau_2} - \frac{P}{\tau_t}, \tag{14}$$

where N_2 is the population density of the metastable state, P is the concentration of photons in the material due to both spontaneous and stimulated emission, τ_2 is the fluorescence decay of the metastable state, τ_{st} is the stimulated emission parameter, and τ_t is the transit time of the photons of the material. The first term on the right-hand side of Eq. (14) represents the increase in photon density due to stimulated emission. The second term represents the increase in radiation due to a small amount of spontaneous emission. τ_t can be thought of as the average lifetime of photons in the material before they are absorbed or travel out of the sample. τ_t is needed in this analysis because in a mirrorless system with no feedback the photons have a finite time during which they can effectively contribute to ASE. For our study, τ_t is approximated by the time it takes light to travel through the pumped region of the sample which is 10^{-11} s. The values of τ_2 are measured in weak pumping conditions and are given in Table I.

Equations (13) and (14) are a set of coupled first-order differential equations which cannot be solved analytically. A fourth-order Runge-Kutta method was used to obtain solutions to these equations. To simulate the δ-function excitation, the initial condition was no photons in the sample, $P(0) = 0$, and a specific value for the initial population of the metastable state, $N_2(t) = N_2(0)$. This latter quantity is directly proportional to the power of the pump pulse. To overcome the numerical instability inherent in the solutions and obtain reliable results, a small step size of 10^{-11} s was used. Since the measured fluorescence intensity I is

proportional to the number of photons escaping the material and this in turn is proportional to the number of photons in the material, P, the relationship between theory and experiment is given by

$$I \propto P \tag{15}$$

Typical results of this theoretical analysis are shown in Fig. 2. Equations (13) and (14) are solved to give the time evolution of the number of photons in the sample for different values of the initial population of the metastable state. For this example, the pertinent parameters are $\tau_t = 10^{-11}$ s, $\tau_{st} = 3 \times 10^6$ s/cm^3, and $\tau_2 = 9 \times 10^{-6}$ s. For low levels of excitation power, the photons in the sample are predominantly those generated by spontaneous emission and their concentration is essentially negligible on the scale in Fig 2. As the pump power is increased above a certain level for $N_2(0)$, stimulated emission processes become important and the number of photons in the sample increases by several orders of magnitude for a brief amount of time. The time at which the concentration of photons in the sample reaches a maximum decreases, and the increment of time during which contributions from stimulated emission are important becomes smaller with increasing values of $N_2(0)$. Since the rate of decay of the concentration of the photons in the sample depends on the concentration of photons the decay curves are nonexponential with the degree of nonexponentiality depending on the initial population of the metastable state. After long times, the decays approach an exponential behavior with the decay rate τ_2^{-1}. Typical decay curves are shown in Fig. 3 with the intensities of the peaks dependent on the initial power of the pump pulse. The different curves in this figure are for $N(0) = 2.3 \times 10^{17}$ (solid line); $N(0) = 1.0 \times 10^{17}$ (dashed line); and $N(0) = 0.5 \times 10^{17}$ (broken line).

Since the measured fluorescence decay curve follows the same behavior as the population of the metastable state, the observed decay rates can be compared with the decay rates of $P(t)$ obtained from theoretical analysis. Since the decay kinetics are nonexponential, we define the decay time τ as the interval between the maximum and the 1/e of the maximum intensity. Typical results for the

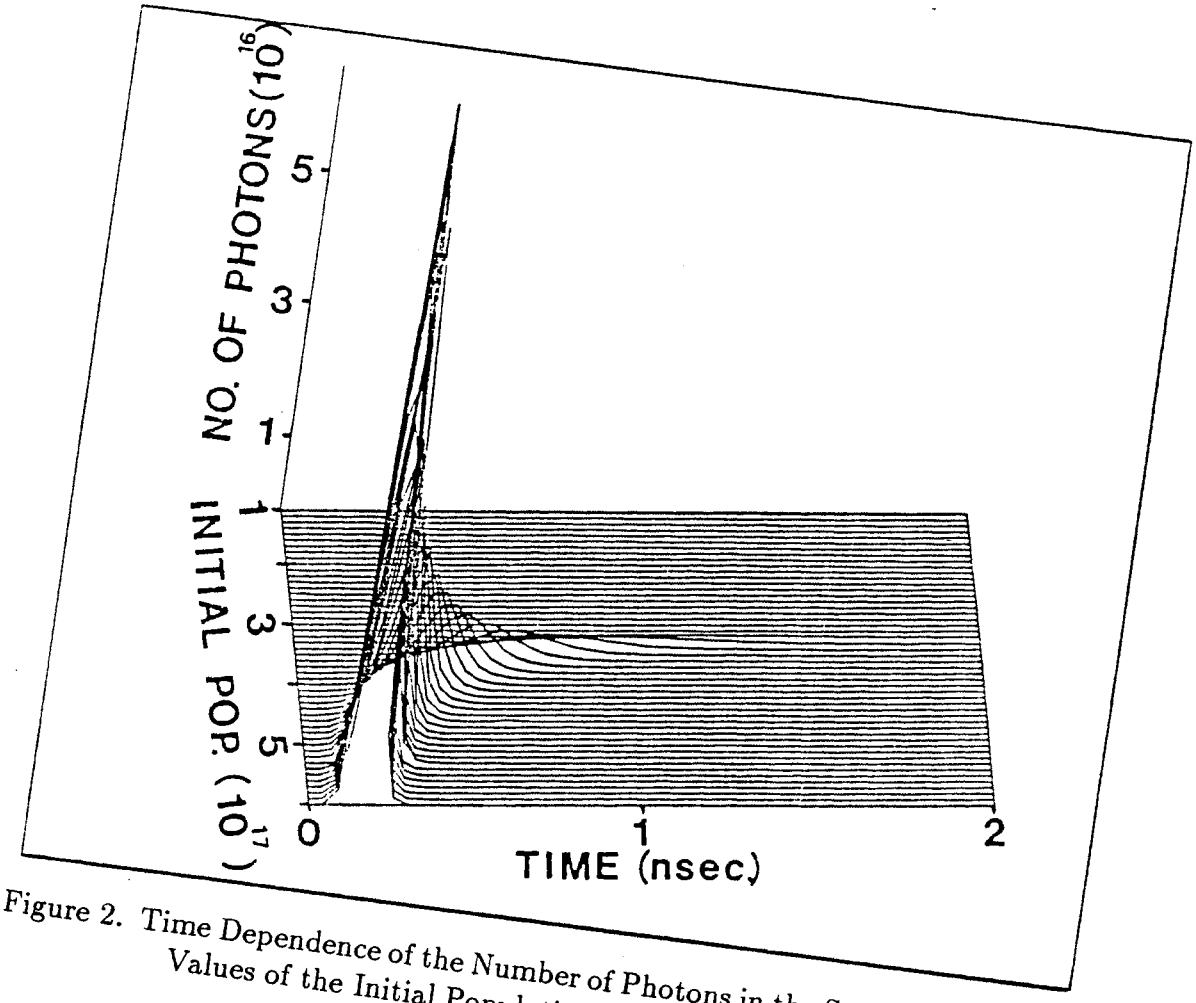

Figure 2. Time Dependence of the Number of Photons in the Sample for Different Values of the Initial Population of the Metastable State

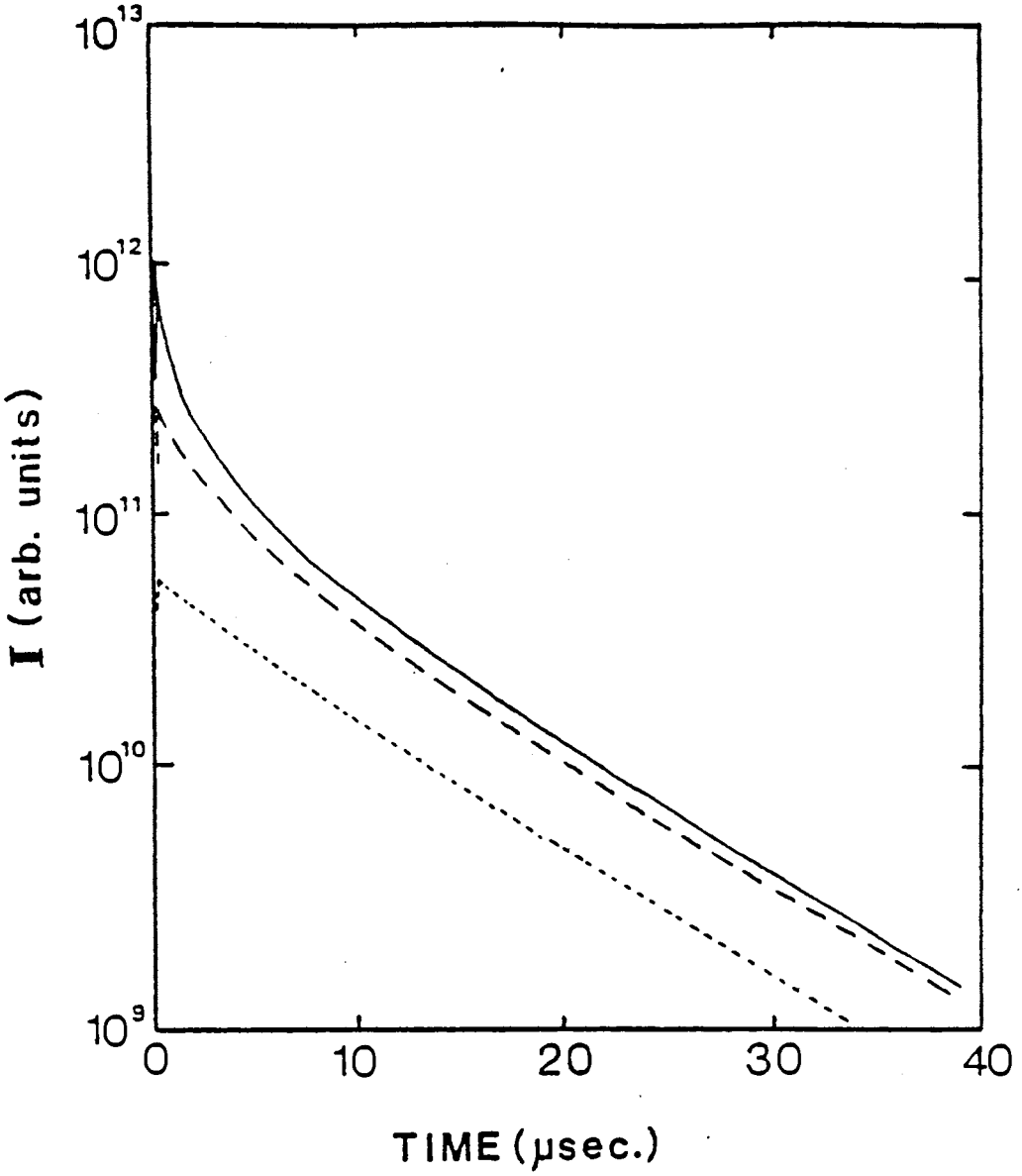

Figure 3. Decay Kinetics of the Fluorescence Emission of a Sample Excited by High Power, Picosecond Pulses

variation of the decay rate as a function of $N_2(0)$ for different values of τ_{st} are shown in Fig. 4. The solid, dashed, and broken lines are for values of τ_{st} of $3.0 \times 10^6, 2.35 \times 10^6$, and 2.0×10^6 cm^{-3} s, respectively. The dotted line and circles represent the experimental data obtained for $RbCaF_3$:Rh^{2+}. The value of the decay parameter is τ_2 at low values of $N_2(0)$ and decreases as higher pump powers increases the initial population of the metastable state. The significant decrease in τ occurs abruptly above a threshold value of $N_2(0)$. The position of this threshold is proportional to the value of τ_{st} and at very high pump powers, τ obtained from theoretical analysis approaches the value of τ_t. Because of the sensitivity of the threshold position to the parameters of the theory, this is the most useful quantity for determining the quality of the fit between experiment and theory.

The results of the measurements of the fluorescence lifetimes as a function of pump power have been reported previously [2,3]. The general shape of the resulting data curve is the same for each case with the main difference being the value of the threshold for each sample. A typical example of the results is shown in Fig. 4. The results show significantly different lifetimes for low power and high power pumping conditions with a distinct threshold joining the two domains. The major difference between the theoretical and experimental curves is the value of the lifetime at high pump powers. The theoretical value is the very short cavity lifetime while the measured value is much longer due to the limitations of the measurement technique. However, the important parameters are the threshold population and the stimulated emission parameter, and as mentioned above the theoretical curves can be varied by adjusting the stimulated emission parameter until the theoretical value for the threshold matches the experimental data. The comparison between the theoretical predictions and experimental results shown in Fig. 4 shows how sensitive this analysis is to the choice of τ_{st}. The parameters obtained from this analysis are listed in Table I. For each of the samples investigated experimentally, single-pass gain measurements were made in the same pumping conditions to verify

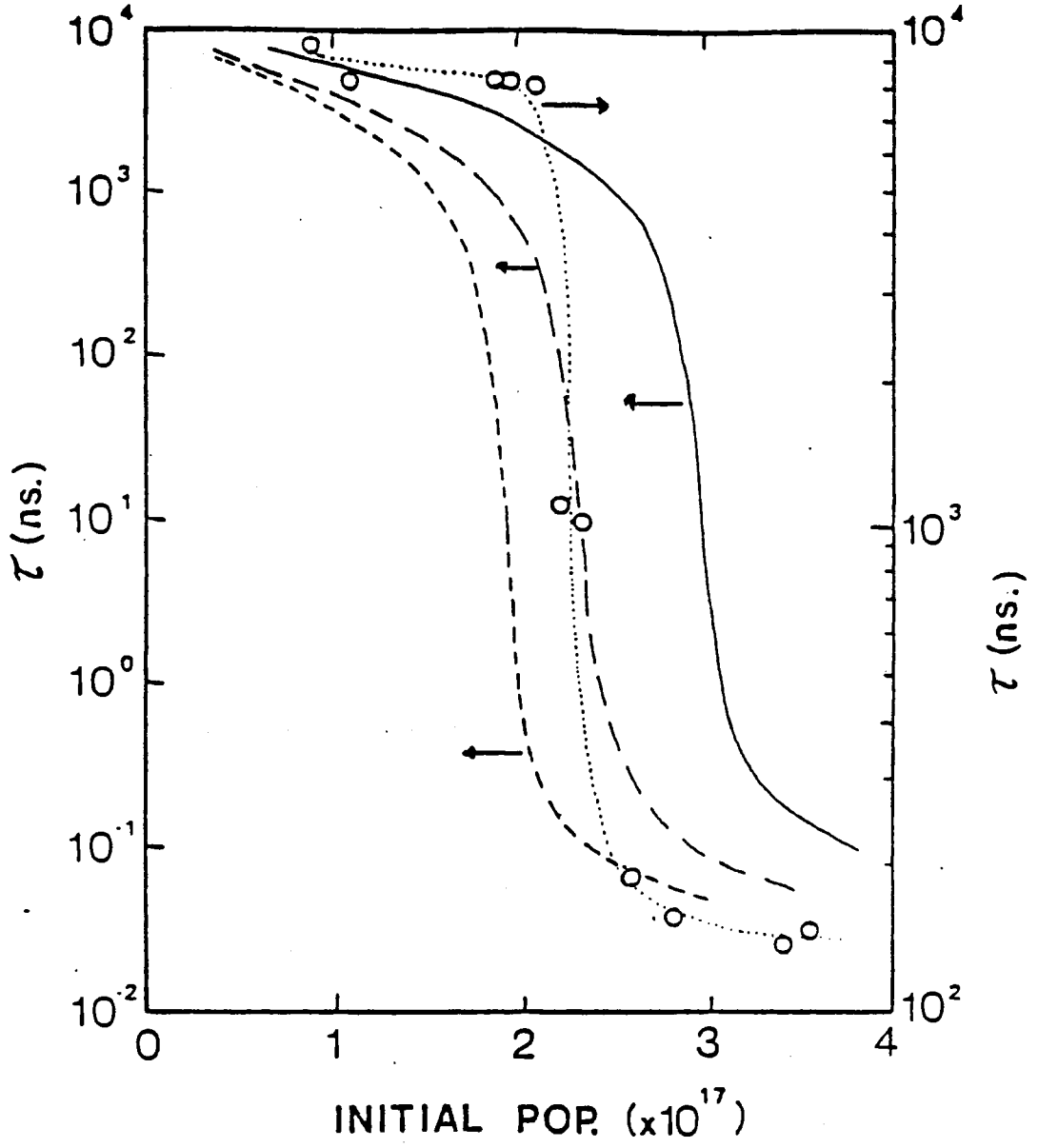

Figure 4. Variation of the Fluorescence Decay Time With Pump Power (the lines represent theoretical predictions for different values of the stimulated emission parameter)

that stimulated emission is the mechansim responsible for the observed lifetime shortening [2,3].

Knowledge of τ_{st} also allows for N_2 to be obtained through the expression

$$N_2 = \frac{\tau_{st}}{\tau_t}. \tag{16}$$

Equation (16) is obtained by setting Eq. (14) equal to zero which gives the peak photon density and then solving for N_2, noting that $\tau_t \ll \tau_2$. The energy density at threshold needed to provide this population inversion is obtained from Eq. (7).

It is possible to estimate values for σ_{21} from the valus of τ_{st}, but the geometry of the medium must be considered because only a portion of the ASE intensity contributes to the measured gain of the material. Assume an inverted cylindrical medium of radius a_o and length L. The stimulated transition rate W_{12} produced by a beam of intensity I is given by [1]

$$W_{12} = (\frac{\pi a_o^2}{4\pi L^2})(\frac{N_2}{\tau_{st}}) = \frac{\sigma I}{h\nu}. \tag{17}$$

This leads to the relationship between the stimulated emission cross section and the stimulated emission parameter:

$$\sigma_{21} = \frac{a_o^2 N_2 h\nu}{4L^2 \tau_{st} I}, \tag{18}$$

where L is the diameter of the pump beam and $2a_o$ is estimated by the $1/e$ value of the beam in the material. The values of the stimulated emission cross sections estimated from Eq. (18) and the pumping energy density at threshold obtained from Eqs. (16) and (7) are listed in Table II.

Discussion

The three experimental methods discussed above give somewhat different values for ΔN, g, and σ_{21} due to the various assumptions made in the theoretical developments and due to differences in experimental accuracies. The values of the population inversions at threshold determined by theoretical fits to the observed band narrowing and from the lifetime shortening technique are in good agreement

with those obtained from single-pass gain measurements. The lifetime shortening method requires an estimate of the transit time of the photons in the sample and the geometry of the gain medium. More accurate values for τ_t and the gain geometry would bring the stimulated emission cross section and the population inversion at threshold more in line with those obtained from other methods. The lifetime shortening technique and the single-pass gain technique generally overestimate g and σ_{21} due to the optical quality of the materials.

Investigating each of the three effects of stimulated emission on the spectral properties of vibronic laser materials described in this work can be useful in evaluating their potential for laser applications. The same parameters can be obtained from each of the three techniques. However, the parameters which are measured directly and which are determined indirectly through theoretical analysis of the data are different for each technique. Monitoring the lifetime shortening as a function of pump power is the easiest way to establish the conditions needed to observe stimulated processes in a material. Analyzing the observed spectral narrowing of the emission provides the simplest method for obtaining estimates of the parameters characterizing the stimulated emission properties of a material. Fitting the band narrowing that takes place above the threshold with a model such as that used to describe vibronic lasers is a more difficult technique than the lifetime shortening measurements but can be more accurate if the transitions giving rise to the emission bands are well understood. Single-pass gain measurements are the most definitive technique for investigating the stimulated emission properties of the material, but they require higher optical quality samples, critical alignment procedures, and more sensitive equipment for determining changes in absolute signal strengths. Finally, it should be mentioned that the effects of stimulated emission observed with fast pulse pumping conditions may be different from those obtained in long pulse pumping conditions due to the presence of time-dependent loss mechanisms. This has been shown to be true for the $Li_6Ge_8O_{19}$:Ti^{4+} crystal studied here. The observed lifetime shortening and gain properties decrease to zero as the pump pulse width is increased from $\approx$ 20 ps to 20 ns [10].

CHAPTER III

SPECTROSCOPY OF VARIOUS TITANIUM-DOPED MATERIALS

Introduction

In a crystal, each ion is subject to an electric field originating from surrounding ions or ligands. The crystal field induced by the surrounding ions will remove the spherical symmetry of a free ion and split the electronic orbital degeneracy outside the closed shell. For transition metal ions with d-orbital electrons (such as Ti^{3+} and Cr^{3+}), the effect of the crystal field can be very large. In contrast, the crystal field effect is small for lanthanide ions with f-orbital electrons (such as Nd^{3+}) because the f-electrons are shielded by outer lying electrons in the s and p orbitals. Thus transition metal ions have electron orbital splittings which are quite sensitive to the crystal symmetry and neighboring ions of the host lattice while lanthanide ions are relatively insensitive [11].

Trivalent titanium is a transition metal ion that has very desireable broad absorption and emission spectra when doped into the correct host. It is therefore of great importance to find an appropriate host material for this impurity ion and thus increase the number of potential tunable solid state lasers. This chapter describes an investigation of the crystals Ti:Sapphire (Al_2O_3:Ti^{3+}), Ti:Chrysoberyl ($BeAl_2O_3$:Ti^{3+}), and Ti:Barahexaluminate ($BaTiAl_6O_{12}$:Ti^{3+}) which will hereafter be referred to as Ti:BA. It was the purpose of this investigation to identify new room temperature laser materials that used Ti^{3+} as the active ion and exhibit the properties of high efficiency and broadband tunability. The spectroscopy of each material was examined and Ti:Sapphire was used as the standard for comparison since many of its spectroscopic properties have been well documented [2,12–25].

The Czochralski method was used to grow each of the three materials. The Ti:Sapphire, Ti:Chrysoberyl, and Ti:BA samples contained Ti^{3+} concentrations of 2.5×10^{20}, 6.2×10^{20}, and 6.1×10^{19} cm^{-3}, respectively, and were 0.95, 0.66, and 0.27 cm thick. Ti^{3+} goes in substitutionally for Al^{3+} in each of the three crystals even though there is a size mismatch with Ti^{3+} being 1.3 times larger than Al^{3+}. Room temperature absorption spectra were obtained using a Perkin-Elmer Model 330 Spectrometer. Fluorescence spectra and fluorescence decays of Ti^{3+} in different hosts at different temperatures were obtained using a cryogenic refrigerator and the 520 nm emission of a dye laser that was pumped with the emission of a nitrogen laser. A 1 meter Spex monochromator with either an RCA C31034 photomultiplier tube sensitive in the visible or a 7102 photomultiplier tube sensitive in the near infrared and an EGG-PAR boxcar integrator were used to measure the fluorescence and decay of the fluorescence. The slits on the monochromator were opened to 0.1 mm to insure good resolution and that an adequate signal could be obtained when measuring the strength and position of the zero-phonon lines.

Ti:Sapphire

Trivalent titanium in Al_2O_3 consists of a closed shell plus a single 3d electron and the splittings of the energy levels when the free ion is introduced into the crystal field are shown in Fig. 5. The single 3d electron gives a free ion ^2D term which splits due to an octahedral crystal field into a $^2T_{2g}$ ground state and a ^2E_g excited state. The trigonal distortion of the crystal field at the Al^{3+} site further splits the $^2T_{2g}$ level into a lower ^2E and an upper $^2A_1$ level. Spin-orbit interaction splits the ^2E ground state into two sets of Kramer's degenerate pairs, the lower state designated as $E_{3/2}$ and the upper as $E_{1/2}$. The $^2A_1$ level becomes an $E_{1/2}$ Kramer's doublet with spin-orbit interaction. Jahn-Teller distortion dominates the excited state and splits the ^2E_g level into an upper $E_{1/2}$ and a lower $E_{3/2}$ level [19].

The polarized absorption spectra of Ti:Sapphire is shown in Fig. 6(A) and consist of a broad band with three peaks located at 300, 488, and 540 nm and a long absorption tail in the near infrared region. Ti:Sapphire is uniaxial, meaning

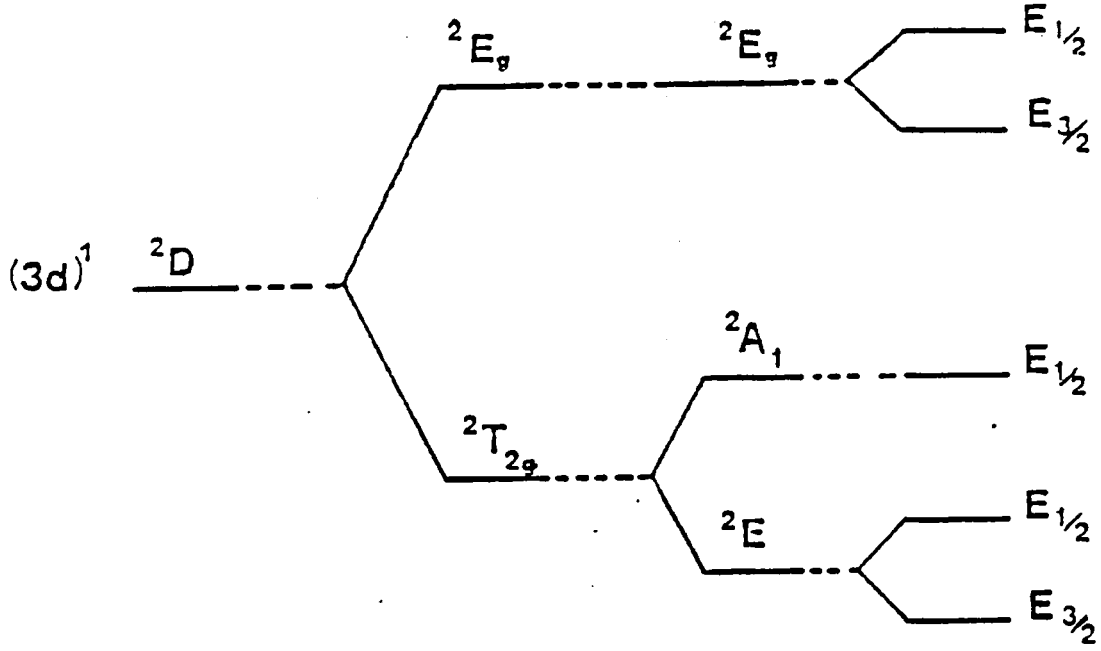

Figure 5. Energy Diagram for the Splitting of the Energy Level of a Single d Electron When the Free Ion is Introduced Into the Crystal Field

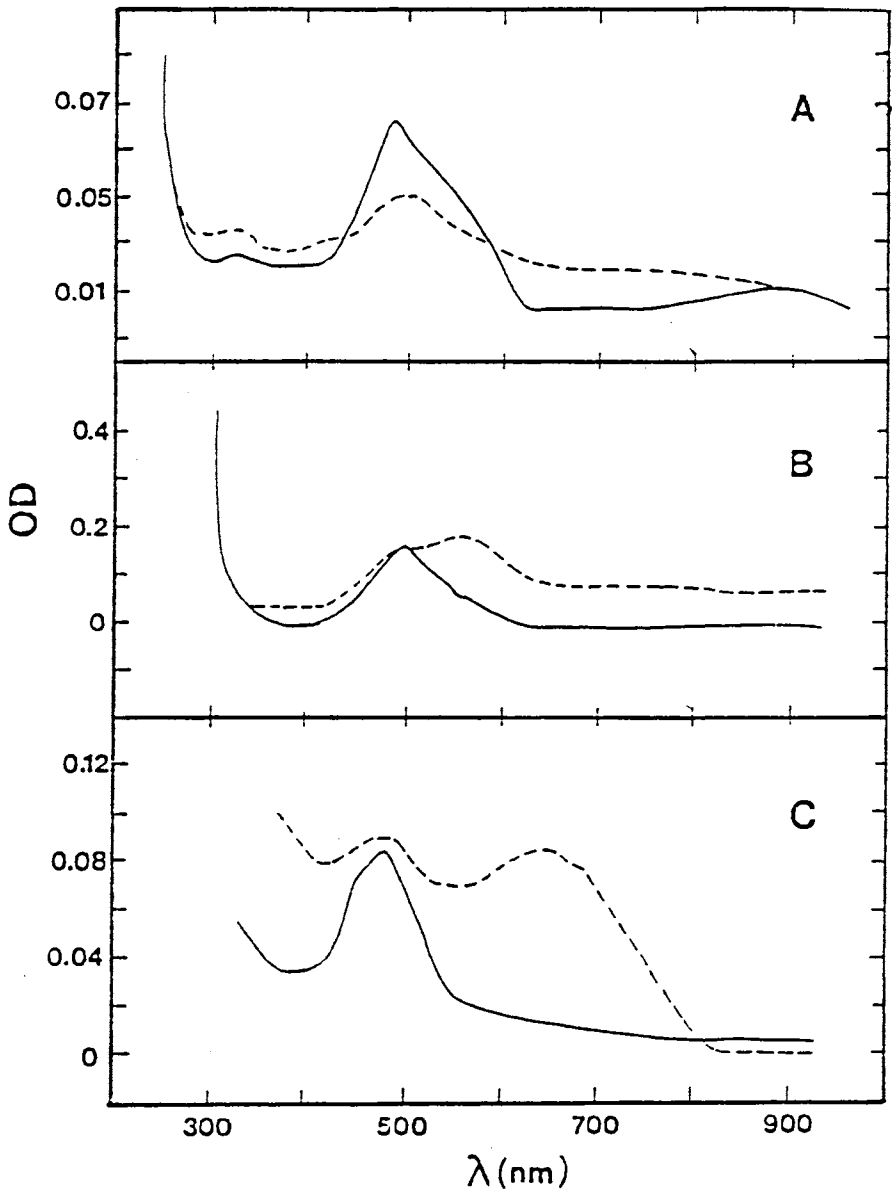

Figure 6. Room Temperature Absorption Spectra of (A) Ti:Sapphire, (B) Ti:Chrysoberyl, and (C) Ti:BA

it has an optic axis called the c-axis. This implies that the absorption spectrum measured with the electric field E of the excitation beam parallel to the c-axis of the crystal (π-polarization) will differ from the absorption spectrum measured with E perpendicular to the c-axis of the crystal (σ-polarization). The absorption spectrum for π-polarization is shown as the solid line and for σ-polarization is shown as the dashed line. Both spectra exhibited the same characteristic shape of Ti^{3+} absorption and only the strength of the absorption transitions differed. The major absorption at 540 nm is due to the transition from the $^2T_{2g}$ ground state to the ^2E excited state of a single d electron occupying an aluminum site in the corundrum lattice. The double peaks at 488 and 540 nm are representative of the Jahn-Teller splitting of the excited state due to the strong vibronic splitting. The absorption tail in the near infrared is located spectrally in the lasing region of Ti:Sapphire and it is associated with the concentration of titanium and impurity ions in the crystal and Ti^{3+} - Ti^{4+} pairs [19]. The absorption tail could be removed with an annealing treatment.

The unpolarized fluorescence spectra of Ti:Sapphire is shown in Fig. 7(A) and the broad fluorescence band is due to the ^2E_g to $^2T_{2g}$ transition of Ti^{3+}. Polarized fluorescence spectra measurements revealed that the spectral shapes of the π and σ fluorescence bands are very similar and the π fluorescence band was 2.6 times greater than the σ fluorescence band [11]. The dashed fluorescence band peaked at 740 nm is the fluorescence measured at 12 K and the solid line peaked at 763 nm is the room temperature fluorescence. The lifetimes of the ^2E_g to $^2T_{2g}$ transition was measured to be 3.1 μs and 3.3 μs at room temperature and 12 K, respectively. A noticeable spectral shift of the fluorescence peak to lower energy was observed as the temperature was increased. This spectral shift is in general due to the emission and reabsorption of virtual phonons [26]. Zero-phonon transitions were found to lie spectrally at 616.7 and 618.1 nm with an energy difference between the two lines of 37.8 cm^{-1} and are attributed to the transitions from the lower component of the excited state to the two spin-orbit split components of the ground state. The zero-phonon line located spectrally at

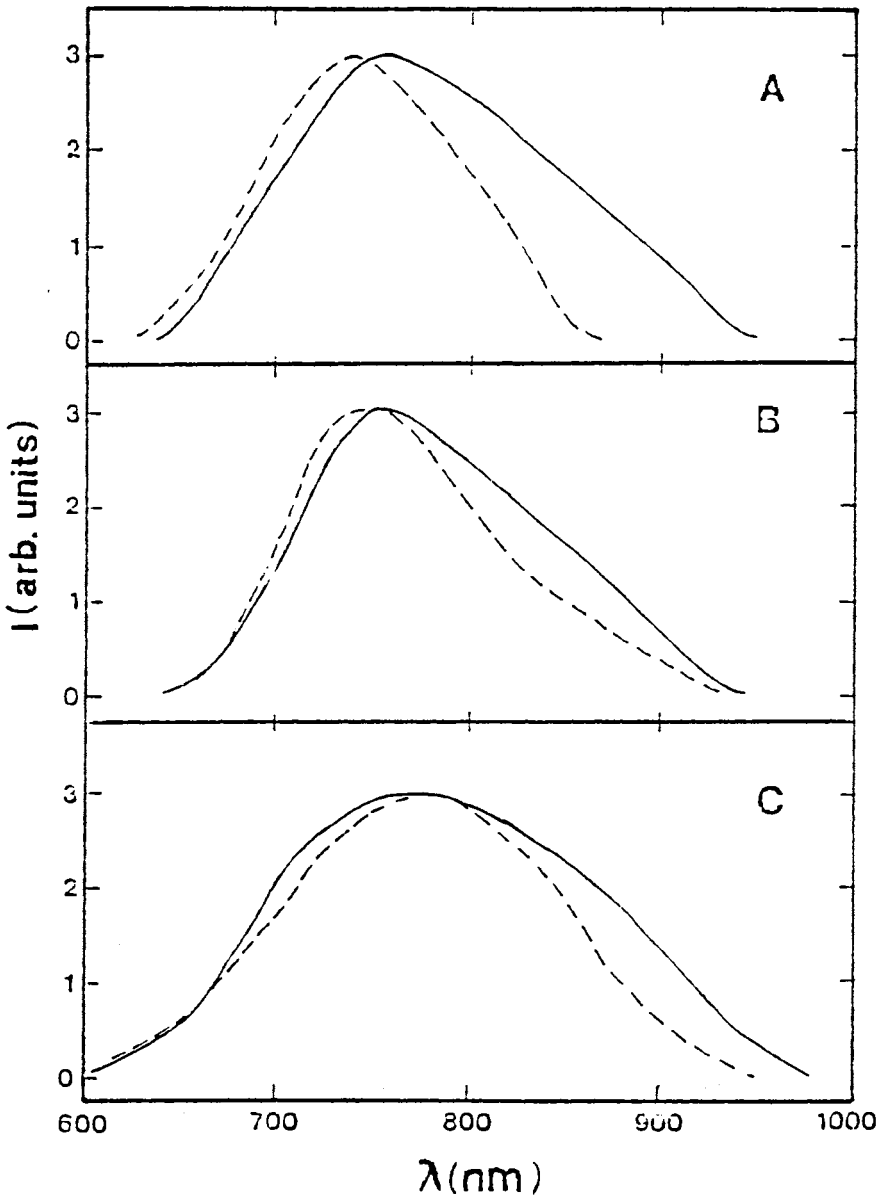

Figure 7. Room Temperature Fluorescence Spectra of (A) Ti:Sapphire, (B) Ti:Chrysoberyl, and (C) Ti:BA

616.6 nm will be referred to in this chapter as R_1 and the zero-phonon line located spectrally at 618.1 nm will be referred to in this chapter as R_2. Both R_1 and R_2 transitions had the same 3.3 μs lifetime at room temperature and this value for the lifetime was the same as was measured for the broad emission band at room temperature. The peak emission cross section (σ_{21}) for the ^2E_g level was determined from spectral parameters using Eq. (1) and the peak emission cross section as well as the sample parameters are listed in Table III.

Ti:Chrysoberyl

Ti:Chrysoberyl consists of a hexagonal closed packed crystal structure with an orthorombic *Pmna* space group. The space group consists of four molecules per unit cell with lattice parameters a=0.9404, b=0.5476, and c=0.4427 nm. The Al^{3+} sites are octahedrally coordinated by the oxygen ions and occur in two inequivalent crystal sites in the lattice. The Al^{3+} sites lying in the mirror-symmetry planes of the lattice have the site symmetry of the C_s point group, while the other Al^{3+} sites possess inversion symmetry and belong to the C_i point group. The O_h crystal field splits the free ion wave function of Ti^{3+}. C_s symmetry causes a distortion in the field which splits the degenerate $^2T_{2g}$ and ^2E_g orbital levels but not the singlet $^2A_1$ level. The spin orbit interaction causes further splitting forming the Kramers' degenerate doublet [24]. This is the same splitting of the energy levels that occurs in Ti:Sapphire.

The polarized absorption spectra of Ti:Chrysoberyl consisted of two broad bands centered at 500 and 564 nm and are shown in Fig. 6(B). Ti:Chrysoberyl is also uniaxial and both polarized absorption spectra of Ti:Chrysoberyl exhibit the same features. The major absorption at 564 nm was due to the transition between the $^2T_{2g}$ ground state and the ^2E_g excited state. These double peaks are representative of the Jahn-Teller splitting of the excited state due to the strong vibronic splitting and the Jahn-Teller splitting determined from the absorption spectra was determined to be 2270 cm^{-1}. The absorption tail in the near infrared was observed not to be as prevalent as that seen in Ti:Sapphire.

TABLE III

SAMPLE PARAMETERS OF TI:SAPPHIRE
TI:CHRYSOBERYL, AND TI:BA

Parameter	Ti:Sapphire	Ti:Chrysoberyl	Ti:BA
N (cm^{-3})	2.49×10^{20}	6.16×10^{20}	6.10×10^{19}
Δ z (cm)	0.95	0.66	0.27
"R" lines of Ti^{3+}			
R_1 (nm)	616.6	629.1	
R_1 (nm)	618.1		
"R" lines of Cr^{3+}			
R_1 (nm)	694	679.1	679.0
R_1 (nm)	693	677.4	677.0
λ_{peak} (nm)	763	755	780
$\Delta\lambda$ (nm)	170	148	190
$\sigma_{21}(cm^2)$	1.8×10^{-19}	1.3×10^{-18}	3.3×10^{-19}
JT splitting (cm−1)	1973	2270	5635

Fig. 7(B) shows the fluorescence spectra of Ti:Chrysoberyl at room temperature and 12 K. The peak of the broad fluorescence band was due to the ^{2}E to $^2T_{2g}$ transition. The peaks in the fluorescence spectrum occurred spectrally at 733 nm when measured at room temperature and 745 nm when measured at 12 K. The lifetimes for the ^2E to $^2T_2$ transition were 5.9 and 7.0 μs when measured at room temperature and 12 K, respectively. There were no shoulders on the fluorescence band at 550 nm as was observed in Ti:Sapphire but a much broader fluorescence band was observed in the near infrared region. There was only a single zero-phonon line observed for the ^2E to $^2T_{2g}$ transition in Ti:Chrysoberyl, so there was either no spin orbit splitting or the splitting was covered by the inhomogeneous broadening of the ground state. This single zero-phonon line in Ti:Chrysoberyl will be referred to in this chapter as the R line of Ti:Chrysoberyl. The explanation of the inhomogeneous broadening of the ground state is more probably due to the Gaussian shape of the zero-phonon line and a large full width at half maximum of 1.3 nm for this single zero-phonon line. Chromium "R" lines were seen indicating that chromium was present in the material and were due to the ^2E to $^4A_2$ transition of Cr^{3+}. R_1 and R_2 lines for Ti:Chrysoberyl were located spectrally at 679.1 and 677.4 nm with lifetimes of 1.1 μs for R_1 and 1.2 μs for R_2. The peak emission cross section for the ^2E_g level of Ti^{3+} was determined from spectral parameters by Eq. (1) and the peak emission cross section as well as the sample parameters for Ti:Chrysoberyl are given in Table III.

Ti:BA

The space group of barahexaluminate is orthorombic *Pnnm* with unit cell spacing of a=0.4862, b=0.7136, and c=1.3598 nm. The structure of Ti:BA consists of octahedral (mixed Ti and Al occupancy) symmetry and tetrahedra (all Al) symmetry in a three-dimensional array forming tunnels in which barium ions are located. The octahedra form ribbons or strings by edge sharing to one another and are corner shared to tetrahedra [25]. The splitting of the levels of the free

ion for Ti^{3+} that occurred due to the crystal field are very similar to that of both Ti:Sapphire and Ti:Chrysoberyl.

Ti:Ba is also uniaxial and the absorption spectra of Ti:BA in Fig. 6(C) showed two peaks centered spectrally at 480 and 658 nm for π-polarization and only one peak centered spectrally at 480 nm for σ-polarization. The major peak centered at 480 nm is due to the $^2T_{2g}$ to ^2E_g transition in Ti^{3+} and the double peaks are representative of the Jahn-Teller splitting of the excited state. The Jahn-Teller splitting was determined from the absorption spectra to be 5635 cm^{-1} and the absorption band located spectrally in the near infrared was much weaker than that of Ti:Sapphire.

The broad fluorescence band was measured at room temperature and 12 K and is shown in Fig. 7(C). The broad band fluorescence band was associated with the ^2E_g to $^2T_{2g}$ transition in Ti^{3+}. The peak of the fluorescence band occurred spectrally at 780 nm and was measured to have a lifetime of the transition of 1.8 μs when measured at room temperature and 3.4 μs when measured at 12 K. There was no observable spectral shift of the fluorescence emission with temperature. Broad shoulders were again observed in the fluorescence band and a large region of the fluorescence lies within the absorption band. There were no zero-phonon lines for Ti^{3+} seen but the chromium "R" lines were observed and located spectrally at 679 and 677 nm. The peak emission cross section for the ^2E_g level in Ti:BA was determined from spectral parameters by Eq. (1) and given in Table III.

Temperature Dependence of the Fluorescence Lifetime

In all three of the Ti^{3+}-doped materials investigated, the measured fluorescence decay lifetime decreased as the temperature of the host increased. This change in the value of the fluorescence lifetime with temperature was fit with an equation of the form

$$\tau^{-1} = \tau_r^{-1} + A[\exp^{(\Delta E/k_B T)} - 1]^{-1} \tag{19}$$

where τ_r represents the radiative decay rate of the level and the second term on the right-hand side of the equation describes radiationless quenching due to phonon absorption to a higher level. A is the rate constant for the radiationless transition and ΔE is the potential barrier for the process. In Ti:Sapphire, the fluorescence lifetime remains constant at about 3.2 μs below 250 K. At higher temperatures the lifetime began to decrease, indicating that other processes were occurring. For Ti:Chrysoberyl and Ti:BA this decrease in lifetime with increasing temperature began occurring at lower temperatures. The values from fits of the above equation to the experimentally measured lifetimes are listed in Table IV and the fits to the data are shown in Fig. 8.

If the observed fluorescence band was due to vibronic emission between the lowest Jahn-Teller component and the split components of the ground state manifold, then as the temperature was raised, thermal population to the upper Jahn-Teller component of the excited state became possible. If this is the process responsible for the observed shortening of the fluorescence lifetime with change in temperature, then the activation energy (ΔE) is greater by two orders of magnitude in Ti:Sapphire than in Ti:Chrysoberyl and Ti:BA and thermal quenching of the lifetime will take place earlier in Ti:Chrysoberyl and Ti:BA.

Influence of Temperature on the Zero-Phonon Lines

As the temperature is raised, the spectral widths of the zero-phonon lines of Ti^{3+} in sapphire and chrysoberyl increase while their lifetimes remain constant. The zero-phonon lines cannot be observed above 80 K for Ti:Sapphire and 90 K for Ti:Chrysoberyl because of the dominant vibronic emission. Fig. 9 shows the change in the integrated fluorescence intensities of the zero-phonon lines with temperature of Ti:Sapphire [19] and Ti:Chrysoberyl. The solid lines in the figure represent the best fits to the data using an expression of the form

$$I = [A + B \exp^{-\Delta E'/k_B T}] - 1. \tag{20}$$

TABLE IV

PARAMETERS FROM FITTING TEMPERATURE DEPENDENCE OF THE FLUORESCENCE LIFETIME

Parameter	Ti:Sapphire	Ti:Chrysoberyl	Ti:BA
$\tau(\mu s)$	3.2	6.2	3.4
$\tau_r(\mu s)$	8.0	3.1	1.3
A (μs^{-1})	2.6×10^6	1.0×10^4	1.4×10^5
$\Delta E(cm^{-1})$	4000	31.9	54.0

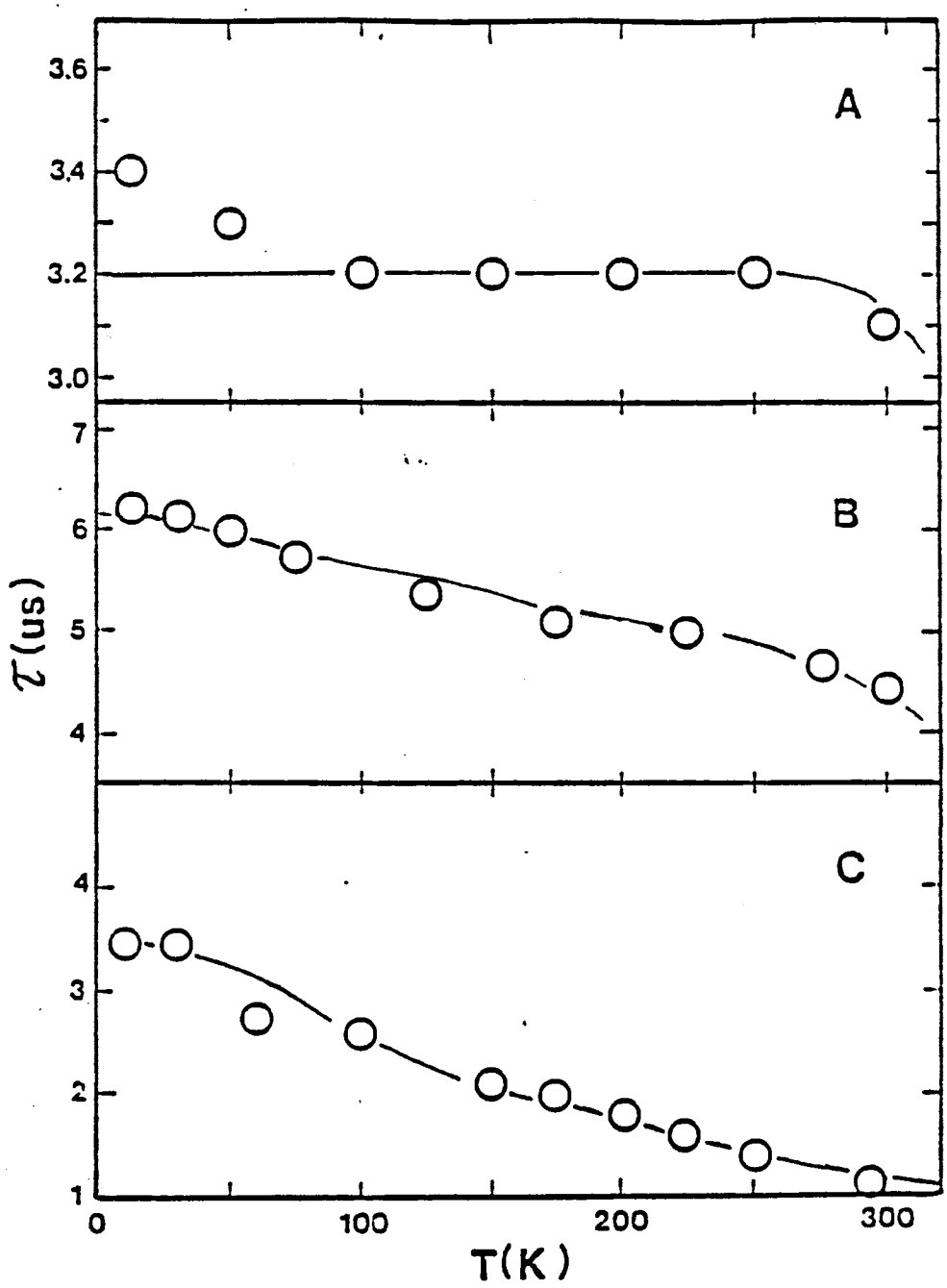

Figure 8. Lifetime vs. Temperature of (A) Ti:Sapphire, (B) Ti:Chrysoberyl, and (C) Ti:Ba

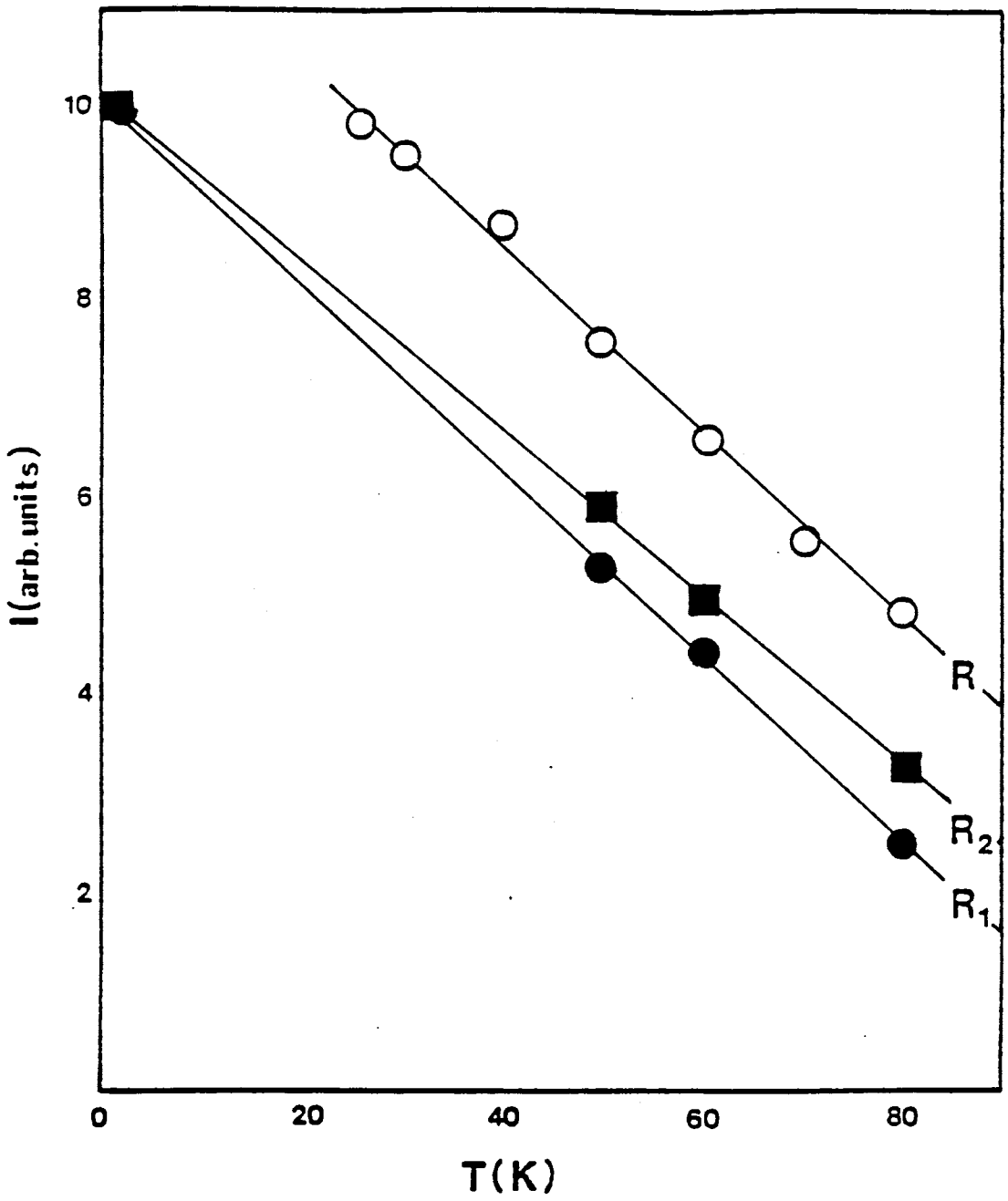

Figure 9. Integrated Intensity of Zero-Phonon Lines Versus Temperature of Ti:Chrysoberyl and Ti:Sapphire

This equation describes the decrease in the fluorescence from an excited level to a lower level due to phonon absorption processes from a lower level to a level located higher in energy by an amount $\Delta E'$. The constants A and B involve parameters such as radiative decay rates and degeneracies of the two levels and the concentration of ions. The values of these parameters from fitting the data are listed in Table V. From reference [19], the activation energies for R_1 and R_2 in Ti:Sapphire were determined to be 125 and 83 cm^{-1}, respectively. These energies represent the phonon energies needed to enhance vibronic emission relative to zero-phonon emission.

The activation energy of the R line for Ti:Chrysoberyl was found to be 126 cm^{-1}. This value is about the same value for the activation energy of R_1 in Ti:Sapphire.

Configuration Coordinate Diagram

General characteristics of the electron-lattice interaction in Ti:Sapphire have been deduced by fitting information from the absorption and emission spectra to a simple harmonic model for vibrations in the electronic levels [20]. These configuration coordinate curves, first introduced by von Hippel [27] and Seitz [28], were used to describe and compare Ti:Chrysoberyl and Ti:BA to Ti:Sapphire. The energy of the system was plotted versus the totally symmetric "breathing" mode of the system. Δq is a measure of the deviation of the mean nearest-neighbor separation from its equilibrium value.

Assuming that the excited state (^2E_g) can be modeled by a parabola with force constant k_e and the ground state ($^2T_{2g}$) can be modeled with a parabola with force constant k_g, the configuration coordinate diagram was constructed and is shown in Fig. 10. Each of the states was treated as a harmonic oscillator with a set of equally spaced vibrational levels and a zero-point vibrational energy. There was a difference in energy minimum for the two different energy levels because the higher energy wavefunction had a different symmetry and thus had a different equilibrium position for the surrounding ion [11]. The curves were displaced with

TABLE V

INTENSITY OF ZERO-PHONON LINES PARAMETERS

Ti:Chrysoberyl	Ti:Sapphire	
R	R_1	R_2
A = 1.03	0.0058	0.007
B = 10.31	0.13	0.04
$\Delta E'(cm^{-1}) = 126$	125	83

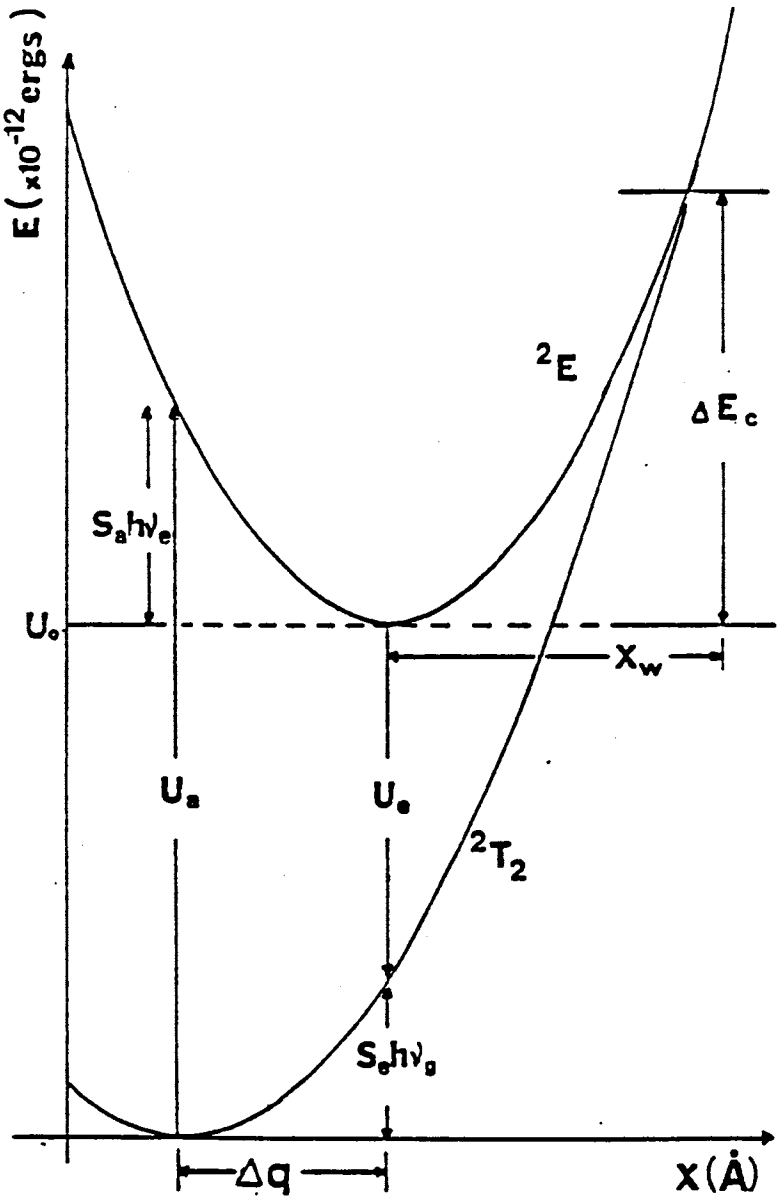

Figure 10. Configuration Coordinate Diagram for Ti:Chrysoberyl

respect to each other along the coordinate axis by the Frank-Condon shift X_o so that optical transitions are made from the minimum of one curve to a portion of the side of the second curve. The transition from the top curve to the lower curve may be to a point that is many vibrational levels above the lower curve's minimum. In order to obtain some useful information from this model, a set of simplifying approximations were made. First, as described by Williams and Hebb [29] and Lax [30], the correspondence principle was used which states that in the limit that quantum effects decrease in importance, quantum effects must reduce to classical theory. This principle allowed the portion of the configuration or potential energy curve to which transitions occur to be replaced with a classical potential energy curve. Next the portion of the configuration coordinate to which transitions are made was approximated with a straight line. This was a good approximation as long as the region of interest was not close to the minimum of the potential energy curve [31].

Fig. 10 shows the classical configuration coordinate where the ground and excited states are displaced by an amount U_o in energy and X_o in the configuration coordinate. The difference between the energy of the zero-phonon energy(U_o) and the absorption(U_a) and emission(U_e) transitions can be described easily in terms of k_e, k_g, and X_o as follows:

$$U_a - U_e = \frac{1}{2}(k_e + k_g)X^2 \tag{21}$$

$$U_o - U_e = \frac{1}{2}k_g X^2 = S_e h\nu_g \tag{22}$$

$$U_a - U_o = \frac{1}{2}k_g X^2 = S_a h\nu_e \tag{23}$$

where S_a and S_e are the average number of phonons in absorption and emission,

respectively, and $h\nu_g$ and $h\nu_e$ are the vibrational energies of the ground and excited state. The vibrational energy of the system in its ground state and of the system in its excited state are given by

$$\nu_g = (\frac{1}{2\pi})(\frac{k_g}{M})^{1/2} \tag{24}$$

$$\nu_e = (\frac{1}{2\pi})(\frac{k_e}{M})^{1/2} \tag{25}$$

where M is the effective mass of the system. The assumption was made that the effective mass of the system in the ground state is equal to the effective mass of the system when the system is in the excited state. Ti^{3+} sits substitutionally in an Al^{3+} site in Ti:Sapphire and is surrounded by six oxygen atoms. From this the effective mass for the Ti^{3+} and its nearest neighbors was calculated to be 2.4×10^{-22} gm. The effective mass for Ti:Chrysoberyl and Ti:BA was approximated with the effective mass of Ti:Sapphire.

A connection can be made between the value of ν_g and the experimental results. If ΔE_{abs} is defined as the band width of the absorption band at wavelengths where the absorption coefficient has decreased to one-half of its maximum value, a general relation between the band width and the absolute temperature T is [31]

$$\Delta E_{abs}(ergs) = A \cdot [(\frac{h\nu_g}{2k_B})\coth(\frac{h\nu_g}{2k_BT})]^{1/2}, \tag{26}$$

where A is a constant, h is Planck's constant, and k_B is Boltzmann constant. A similar expression can be derived for ΔE_{emis} and is

$$\Delta E_{emis}(ergs) = A \cdot [(\frac{h\nu_e}{2k_B})\coth(\frac{h\nu_g}{2k_BT})]^{1/2}. \tag{27}$$

Equation (27) was fit to the time dependence of the full width at half maximum of the fluorescence curve to determine the value of ν_e.

A relation may also be obtained between the width of the low temperature fluorescence band at the full width at half maximum and the constants of the potential energy curves. At the lowest temperature, the temperature at which

essentially all the vibrating systems in question are in the lowest vibrational level, the probability distribution in X follows a Gaussian curve. Using the assumption that this portion of the excited state curve may be replaced by a straight line allows for the multiplication of the probability distribution in X to the slope of the excited state curve at X equal to zero. Using this procedure the width of the low temperature emission band at the half maximum points is given by [31]

$$\Delta E_{emis}(0K) = (1.905 \times 10^{-13}) k_g X_o (\frac{\nu_e}{k_e})^{1/2}. \tag{28}$$

When k_e is greater than k_g, the crossover ΔE_c will be large and consequently, the probability of nonradiative transitions will be low. This is the case for Ti:Sapphire, Ti:Chrysoberyl and Ti:BA. There is no real crossover point of the two parabolas because $k_e > k_g$. A crossover energy can be insured if a model is adopted in which the excited state coupling equals the ground state coupling($k_e = k_g$). This occurs at a position (relative to the excited state minimum) of the crossover point X_w given by

$$\frac{X_w}{\Delta q} = \frac{U_o}{(U_a - U_e)} = \gamma, \tag{29}$$

and has a value

$$\Delta E_c = \gamma^2 (U_a - U_e). \tag{30}$$

The configuration coordinate diagram parameters for Ti:Sapphire, TiChrysoberyl, and Ti:BA are given in Table VI. For high energy thresholds one does not expect that nonradiative transitions will be a dominant process. From the configuration coordinate diagram parameters it appears that Ti:Chrysoberyl is the most promising vibronic laser because it has the lowest probability of nonradiative transitions inhibiting radiative transitions from the $^2T_{2g}$ to ^2E_g level.

Lifetime Shortening

Lifetime shortening is an effective shortening of the fluorescence lifetime at high excitation levels with a distinct threshold for the input power where stimulated emission processes become important [32]. Lifetime shortening measurements were

TABLE VI

CONFIGURATION COORDINATE DIAGRAM PARAMETERS

	Ti:Sapphire	Ti:Chrysoberyl	Ti:BA
U_o (cm^{-1})	16234	15896	16037
U_a (cm^{-1})	20408	20000	20831
U_e (cm^{-1})	13515	13424	12820
$\nu_e(sec^{-1})$	7.0×10^{12}	10.0×10^{12}	10.0×10^{12}
$\nu_e(sec^{-1})$	4.6×10^{12}	6.0×10^{12}	8.2×10^{12}
M (grams)	2.4×10^{-22}	2.4×10^{-22}	2.4×10^{-22}
X_o (cm)	2.4×10^{-9}	1.3×10^{-9}	1.4×10^{-9}
S_e	17.8	12.3	11.5
S_a	19.6	12.3	14.3
ΔE_c(ergs)	13240	13701	10257

attempted on Ti:Chrysoberyl and Ti:BA using a picosecond, passively mode locked Nd:YAG laser doubled to 532 nm. An RCA 7102 photomultiplier tube was used to detect the signal and photographs were taken of the trace with use of a storage scope to determine if lifetime shortening was occurring. The lifetime traces were digitized with the use of a Houston Instruments Hipad digitizer and the lifetimes of the fluorescence were then calculated with an IBM-PC.

Lifetime shortening and lasing have already been demonstrated for Ti^{3+} in sapphire over the wavelength range 660-986 nm [13,14]. The threshold energy for population inversion in Ti:Sapphire has been determined previously to be 2 J/cm^3 and the threshold energy was concentration dependent.

Lifetime shortening has also been seen in Ti:Chrysoberyl and a plot of the power versus 1/e value of the lifetime is shown in Fig. 11. The beginning of the curve is at powers where stimulated emission processes were not occurring and spontaneous emission processes were the dominant processes. As the input power was increased, stimulated emission became the dominant process. Power limitations of the picosecond Nd:YAG laser made it impossible to obtain points higher in input power but Fig. 11 demonstrates that lifetime shortening was occurring. Attempts were made to observe lasing of Ti:Chrysoberyl but were unsuccessful and is probably due to high losses from the surfaces of the sample. Lasing of Ti:Chrysoberyl has been observed recently by longitudinally pumping the sample with a frequency-doubled Q-switched YAG laser. The threshold energy for laser emission to occur was measured to be 15 mJ [33].

Ti:BA had a low damage threshold making it difficult to see lifetime shortening. Surface damage occurs at powers lower than what is needed for stimulated emission processes to be seen.

Other Ti^{3+}-Doped Materials

Ti^{3+} ions in sapphire have been shown to lase over a broadband, continuously tunable wavelength range. Since the crystal field of the host material greatly affects the spectral locations of the absorption and fluorescence and the value of

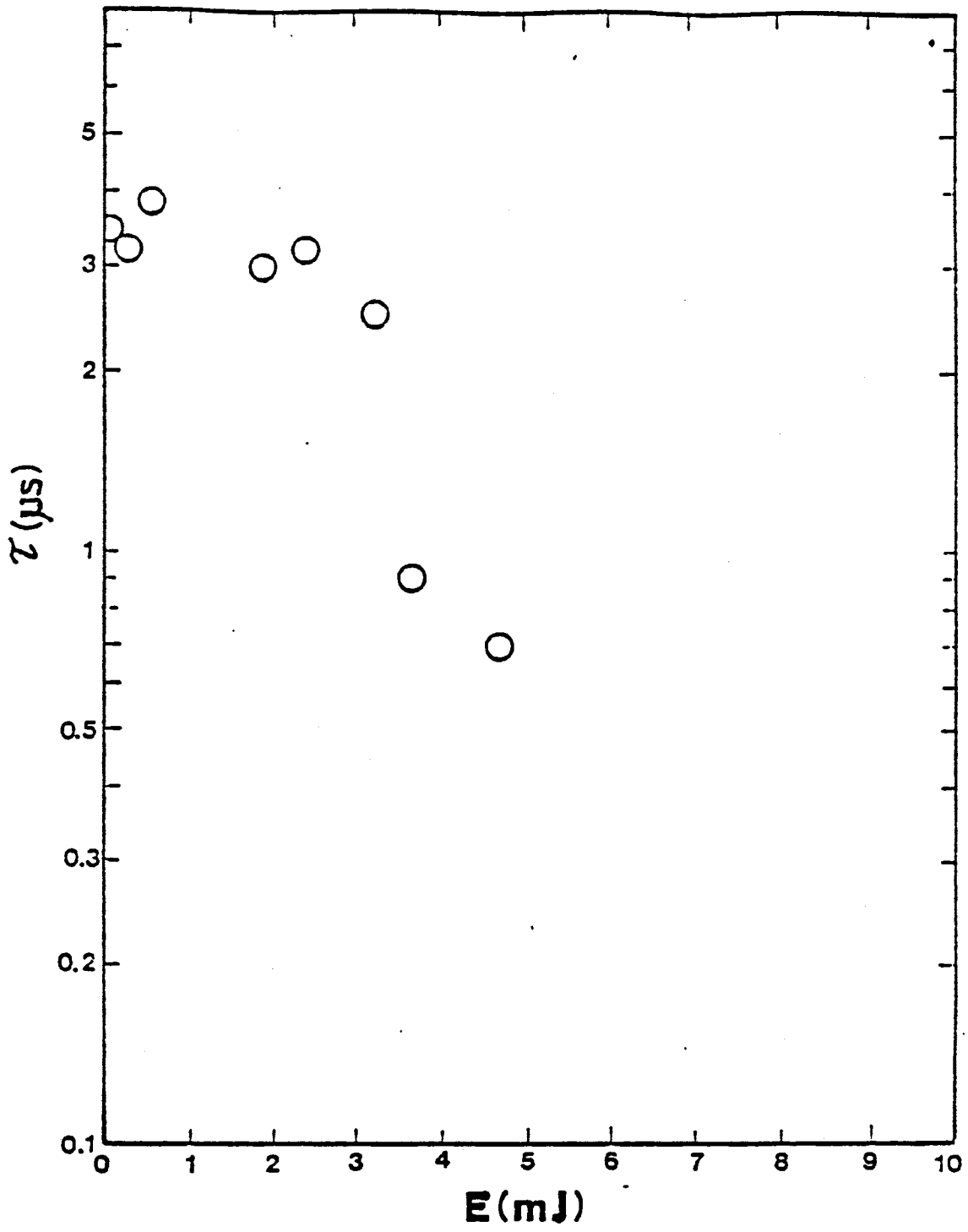

Figure 11. 1/e Value of the Fluorescence Versus Pump Energy of Ti^{3+} in Chrysoberyl

the fluorescence lifetime, a great deal of additional research has taken place in an effort to find an additional host materials for Ti^{3+} ions that produce the desired spectroscopic characteristics. This section gives a brief overview of some of the materials recently investigated.

Ti^{3+}:$YAlO_3$

The absorption spectrum of Ti^{3+}:$YAlO_3$ [11] exhibits two absorption peaks similar to Ti:Sapphire. These peaks are at 435 and 490 nm and are shifted spectrally to shorter wavelengths than Ti:Sapphire. The absorption spectra did not significantly depend upon the field orientation and the shift of the peaks of the absorption spectrum indicates that the crystal field in $YAlO_3$ is larger than it is in Ti:Sapphire. The broadband peak in the near infrared is similar to the Ti^{3+}-Ti^{4+} pair absorption observed in Ti:Sapphire but much larger.

The peak of the fluorescence of Ti^{3+}:$YAlO_3$ occurs at 610 nm and has been shifted to lower wavelengths. There is a single zero-phonon line located spectrally at 540 nm observable at low temperatures. If the splitting of the $^2T_{2g}$ ground state is less than the zero-phonon linewidth, then only one zero-phonon line would be seen. The fluorescence lifetime has been measured to be 12 μs at room temperature and Ti:$YAlO_3$ has a longer lifetime than Ti:Sapphire. The integrated intensity of the fluorescence of Ti:$YAlO_3$ does not change significantly with temperature until after room temperature has been reached. It is possible that the larger crystal field in Ti:$YAlO_3$ prevents nonradiative losses.

Attempts to observe lasing in Ti:$YAlO_3$ are as of yet unsuccessful and the lack of lasing has been attributed to color centers which are being created and destroyed by the pump beam. Stimulated emission has been observed in Ti:$YAlO_3$[34] but better growth techniques are needed before Ti:$YAlO_3$ can become a viable laser material.

Ti^{3+}:YAG

Ti^{3+}:YAG [11] has absorption peaks centered at 505 and 585 nm and these peaks are at longer wavelengths than in Ti:Sapphire, indicating a smaller crystal

field in Ti:YAG. The infrared absorption peak located spectrally at 800 nm is not as strong as Ti:Sapphire.

The fluorescence of Ti^{3+}:YAG is shifted to longer wavelengths with a maximum at 766 nm and the room temperature fluorescence is less intense than the low temperature fluorescence. At low temperatures, zero-phonon lines were observed at 650.6, 651.4, and 653.3 nm. The fluorescence lifetime has been measured to be 48 μs at 11 K and quenches rapidly with increasing temperature, indicating that nonradiative relaxation begins to occur at temperatures well below room temperature. This rapid quenching of the fluorescence lifetime with increasing temperature will make room temperature laser operation of this material highly unlikely.

Ti^{3+}:GSGG

Attempts have been made to grow Ti^{3+}:GSGG (gadolinium-scandium-gallium garnet) by Airtron but only Ti^{4+}:GSGG could be grown [11]. Annealing was attempted in an effort to reduce titanium from Ti^{4+} to Ti^{3+} but efforts were unsuccessful. Ti:GSGG must therefore be eliminated as a potential laser material until titanium can be introduced into the crystal as Ti^{3+}.

Ti^{3+}:GSAG

The absorption spectrum of Ti:GSAG (gadolinium-scandium-aluminum garnet) exhibits two broadband absorption peaks that are located spectrally at 520 and 620 nm [11]. Broadband emission of Ti^{3+} can also be observed from 690 to beyond 1150 nm and peaked at 840 nm. The lifetime of the fluorescence is 5.5 μs at 11 K but decreased rapidly as the temperature of the host increased. The integrated fluorescence intensity also decreased rapidly as the temperature is increased and at room temperature the fluorescence emission is almost totally quenched by nonradiative relaxation. Ti:GSAG is not a viable room temperature laser material since the fluorescence emission is quenched at room temperature but it does have possibilities at lower temperatures.

Ti^{3+}:PNA glass

The absorption spectrum of PNA (P_2O_5 - Na_2O - Al_2O_3) glass is very similar to the absorption spectrum of Ti:Sapphire [35]. The absorption spectrum extends from 560 to 696 nm and is broader than the spectrum of Ti:Sapphire and is shifted to lower energies. The fluorescence of Ti:PNA glass exhibits a broad band centered at 860 nm and is associated with the ^2E_g to $^2T_{2g}$ transition of Ti^{3+}.

Ti^{3+}:$MgAl_2O_4$

The absorption spectrum of Ti^{3+} in $MgAl_2O_4$ exhibits a broad band with peaks located spectrally at 450 and 716 nm [36]. The fluorescence of Ti:$MgAl_2O_4$ is a broad band centered at 740 nm.

Ti^{3+}:Phosphate Glass

The room temperature absorption spectrum of Ti^{3+} -doped phosphate glass shows a broad band with two components peaked at 560 and 685 nm [37]. These peaks lie spectrally at a longer wavelength than the peaks of Ti:Sapphire, indicating that the crystal field in the glass is less than that of Sapphire. The emission of Ti^{3+}:phosphate glass is broadband peaked at 860 nm and the intensity of the fluorescence decreases with increasing temperature.

Summary and Conclusions

Two materials have been investigated in an attempt to find an alternative to Ti:Sapphire as a tunable room temperature laser material. The two materials, Ti:Chrysoberyl and Ti:Ba, exhibit the characteristic absorption and fluorescence bands of Ti^{3+}. The fluorescence decay and the single zero-phonon line of Ti:Chrysoberyl were examined. A configuration coordinate diagram for Ti:Chrysoberyl was constructed in an attempt to explain its spectroscopic properties. Lifetime shortening measurements were attempted on both Ti:Chrysoberyl and Ti:BA with less than satisfactory results. Ti:BA had a low surface damage

power threshold and Ti:Chrysoberyl had a high power threshold for the onset of stimulated emission to occur. A brief literature search of other potential Ti^{3+} hosts reveal that Sapphire is still the best choice for a room temperature laser material that utilizes Ti^{3+} as the lasing ion.

CHAPTER IV

SPECTROSCOPIC STUDY OF $LiNbO_3$:MgO,TM

Introduction

Materials exhibiting broadband vibronic emission are particularly interesting as laser materials because of the capability of continuously tuning the emission of these materials over a broad spectral range. Earlier studies of one of these materials considered $LiNbO_3$ as a laser host [38–42] but this host was rejected because of the photorefractive effect occurring in this material under optical pumping. More recent studies however reveal that magnesium when doped into this material can quench the photorefractive effect [43] and can alleviate the crystal-cracking during the growth of the crystal [44]. The purpose of the study described in this chapter was to investigate $LiNbO_3$:MgO doped with various transition metal ions in an attempt to find a new vibronic room temperature laser material. The materials investigated were $LiNbO_3$:MgO,Co^{2+}, $LiNbO_3$:MgO,Ni^{2+}, and $LiNbO_3$:MgO,Cr^{3+}.

$LiNbO_3$:MgO,Co^{2+}

The first material studied was $LiNbO_3$:MgO,Co^{2+}. Co^{2+} is a transition metal ion and has lased in other host materials at a temperature of 77 K [6,45–47]. The crystal was of good optical quality and contained 4.5 % magnesium and 0.2 % cobalt. The concentration of Co^{2+} in the sample was calculated to be 7×10^{19} ions/cm^3 and the sample was 0.165 cm thick.

The room temperature absorption spectrum of $LiNbO_3$:MgO,Co^{2+} was measured using a Model 330 Perkin-Elmer Spectrometer and is shown as the solid line in Fig. 12. The energy level assignments for Co^{2+} are given in Table VII and

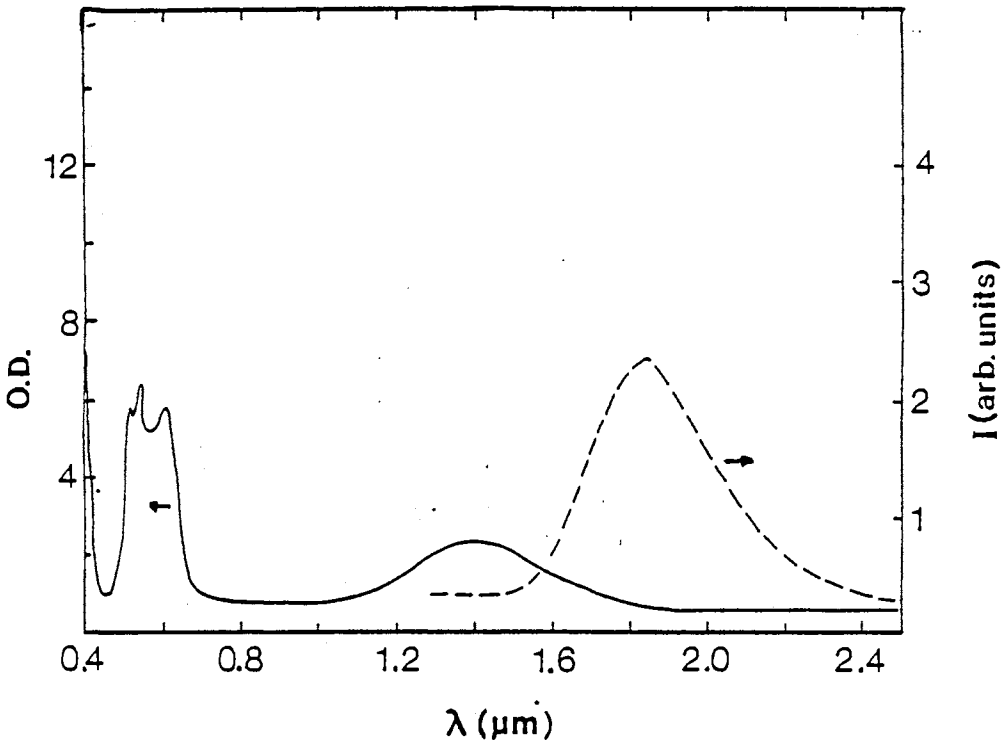

Figure 12. Room Temperature Absorption (solid line) and Fluorescence (broken line) Spectrum of $LiNbO_3$:MgO,Co^{2+}

TABLE VII

ENERGY LEVEL ASSIGNMENTS OF Co^{2+}
IN $LiNbO_3$:MgO,Co^{2+}

λ (nm)	Energy (cm^{-1})	Energy Level Assignment
	0	$^4T_1$
		^2E
1400	7142	$^4T_2$
610	16393	$^2T_1$
590	16949	$^2T_2$
548	18248	$^4T_1$

correspond to the peaks of the absorption spectra. The Tunabe-Sugano diagram for Co^{2+} having a d^7 electronic configuration is shown in Fig 13 and the Racah B parameter for Co^{2+} has a value of 970 cm^{-1} [48]. The crystal field splitting Δ was determined to be 17266 cm^{-1} by matching the energies of the peaks of the absorption spectum to the energy splittings in the Tunabe-Sugano diagram for Co^{2+}.

The fluorescence of Co^{2+} in $LiNbO_3$:MgO at 77 K is shown as the broken line in Fig. 12. The 454 nm emission of an argon laser was used to pump ions into the $^4T_1$ level of Co^{2+} located spectrally at 548 nm and the resulting fluorescence obtained at 12 K was a broad band peaked at 1.8 μm and was due to the $^4T_2$ to $^4T_1$ transition. The lifetime of the transition was measured with an InAs infrared detector, a signal averager, and the excitation beam from the argon laser was chopped with an optical chopper. The lifetime of this transition was measured to be less than 282 μs and this upper limit was equipment limited. An intensity versus temperature plot of the fluorescence is shown in Fig. 14 and the intensity was quenched to 10 % of its initial value at a temperature of 200 K. There was no room temperature fluorescence and this was due to thermally activated non-radiative transitions quenching the fluorescence. Since there was no room temperature fluorescence, this material was eliminated as a new vibronic room temperature laser material.

$LiNbO_3$:MgO,Ni^{2+}

The second material studied was $LiNbO_3$:MgO,Ni^{2+}. Ni^{2+} is a transition metal ion and it has been shown to lase in other hosts at temperatures ranging from 77 to 240 K [6,49]. The crystal was of good optical quality and contained 4.5 % magnesium and 1.0 % nickel. The sample was 0.16 cm thick and the concentration of Ni^{2+} was calculated to be 3.6×10^{20} ions/cm^3.

The room temperature absorption spectrum of $LiNbO_3$:MgO,Ni^{2+} is shown as the solid line in Fig. 15. The energy level assignments for the absorption spectrum are given in Table VIII. The Tunabe-Sugano diagram for Ni^{2+} having a

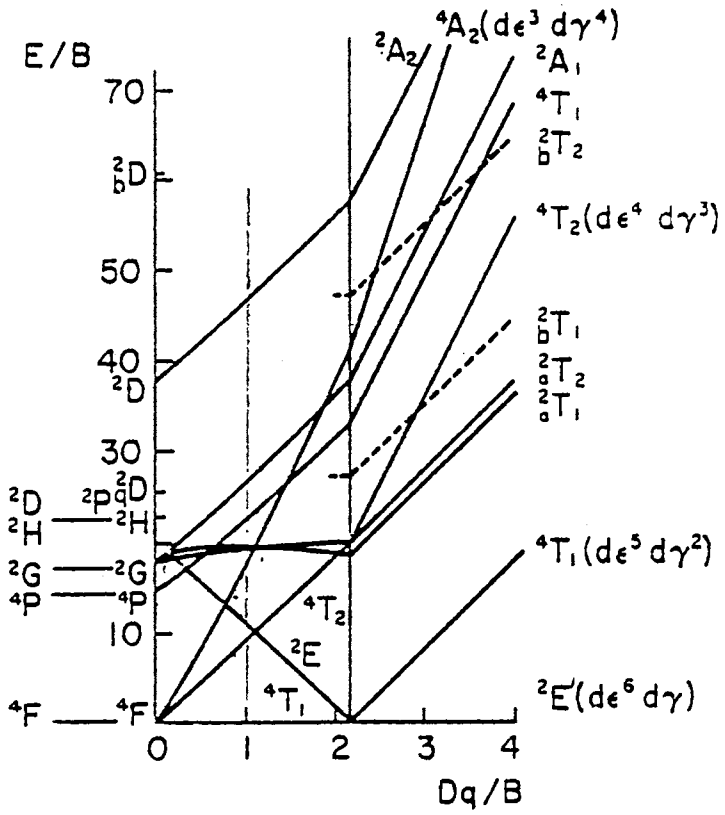

Figure 13. Tunabe-Sugano Diagram for Co^{2+}

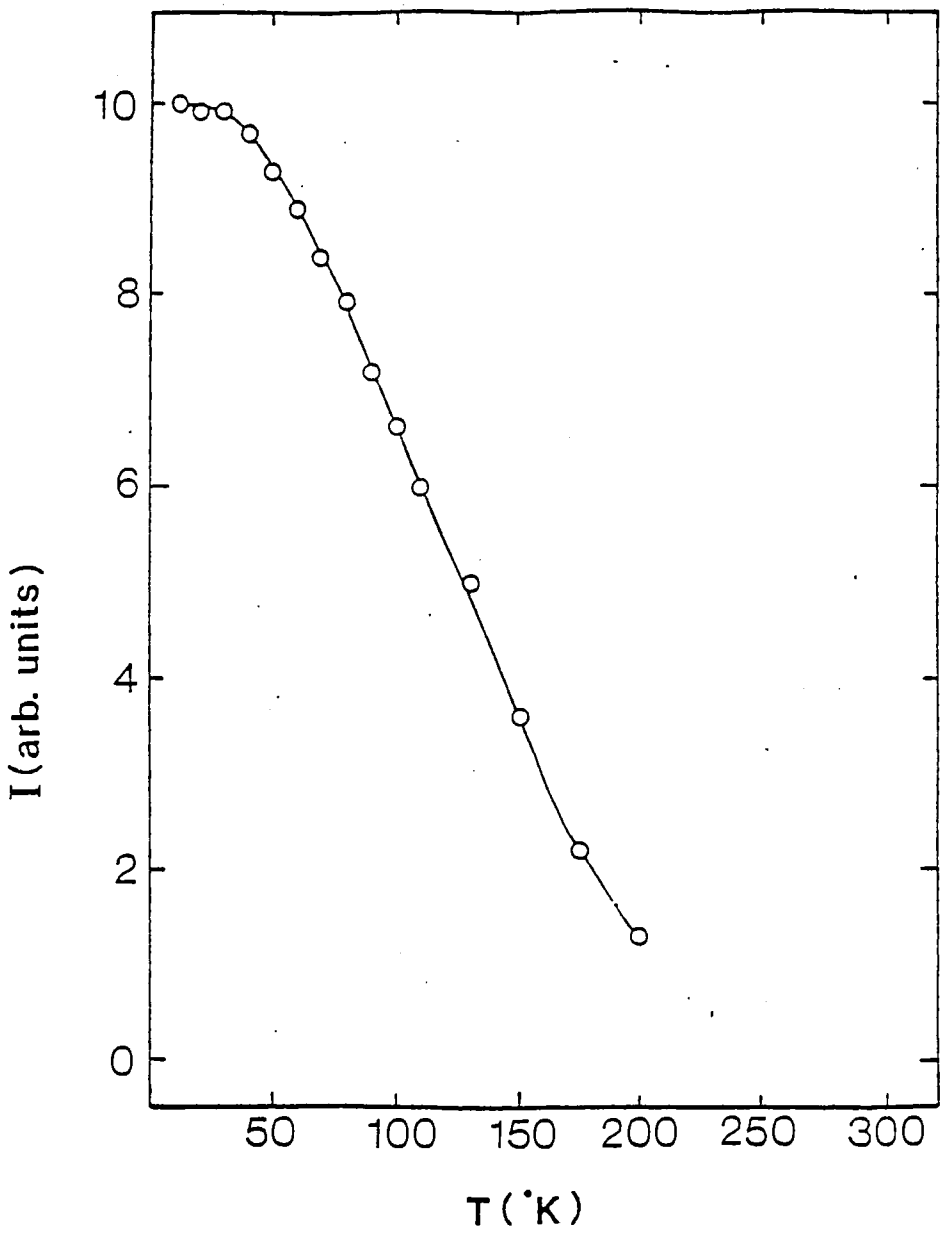

Figure 14. Temperature Dependence of the Fluorescence of Co^{2+} in $LiNbO_3$:MgO,Co^{2+}

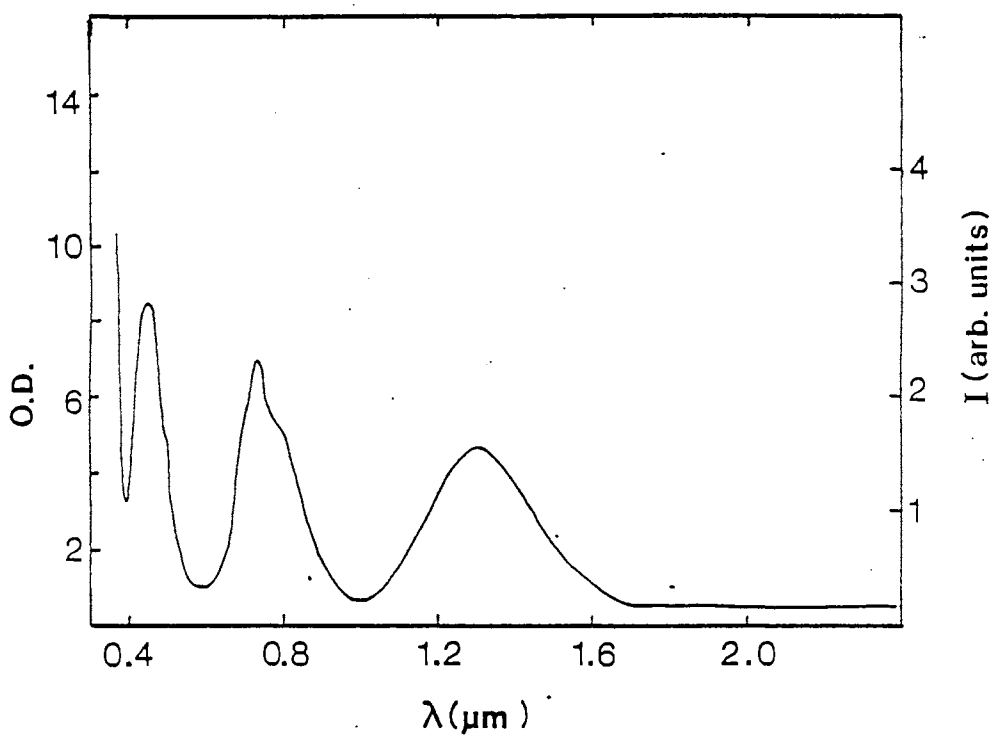

Figure 15. Room Temperature Absorption Spectrum of $LiNbO_3$:MgO,Ni^{2+}

TABLE VIII

ENERGY LEVEL ASSIGNMENTS OF Ni^{2+}
IN $LiNbO_3$:MgO,Ni^{2+}

λ (nm)	Energy (cm^{-1})	Energy Level Assignment
	0	$^3A_{2g}$
1300	7692	$^3T_{2g}$
		^1E_g
730	13698	$^3T_{1g}$
520	19231	$^1T_{2g}$
488	20492	$^1A_{1g}$
450	22222	$^3T_{1g}$
424	235848	$^1T_{1g}$

d^8 electronic configuration is shown in Fig 16 and the Racah B parameter for Ni^{2+} is 1080 cm^{-1} for Ni^{2+} in octahedral symmetry [48]. The crystal field splitting Δ was determined to be 8100 cm^{-1} by matching the energies of the peaks in the absorption spectrum to the Tunabe-Sugano diagram. There was no detectable fluorescence of Ni^{2+} at low temperatures (12 K) and two possibile reasons for this are concentration quenching or radiationless decay. This material was also eliminated as a room temperature laser material since there was no room temperature fluorescence.

$LiNbO_3$:MgO,Cr^{3+}

The third material studied was a single crystal of $LiNbO_3$ doped with 4.5% MgO and 0.05 % Cr_2O_3. The concentration of Cr^{3+} in the crystal was 3.6×10^{19} cm^{-3}. The Cr^{3+} ions most likely occupy the Nb^{5+} sites of $LiNbO_3$ [50,51]. Below the ferroelectric Curie temperature of 1190°C, $LiNbO_3$ is rhombohedral, belonging to the space group R3c at room temperature. The Li^+ ion lies in the oxygen plane at the growth temperature and down to the Curie temperature, so the only octahedral site is the Nb^{5+} site. Since the Cr^{3+} ions prefer octahedral coordination, the Nb^{5+} sites are more probable than the Li^+ sites [52]. On the basis of size (Cr^{3+} radius = 0.063 nm, Li^+ radius = 0.068 nm, Nb^{5+} radius = 0.067 nm) and charge misfits, the Cr^{3+} ion is as likely to enter the Li^+ sites as the Nb^{5+} sites but less likely to enter the vacancy sites. The electronegativity of Cr^{3+} is 1.6, while that of Li^+ and Nb^{5+} is 0.95 and 1.7, respectively. So on the basis of substitutional sites, Nb^{5+} is preferred. In light of the above discussion, the most probable site for the Cr^{3+}-ion impurity in $LiNbO_3$ is the Nb^{5+} site [52].

The room temperature absorption spectrum of $LiNbO_3$:MgO,Cr^{3+} is shown as the solid lines in Figures 17. The energy assignments of Cr^{3+} are given in Table IX and the wavelengths listed correspond to the absorption spectra. The absorption spectrum exhibits the characteristic transitions seen in Cr^{3+} materials. The transition from the $^4A_2$ level to the $^4T_1$ level is peaked spectrally at 480 nm and the transition from the $^4A_2$ level to the $^4T_2$ level is peaked spectrally at 650

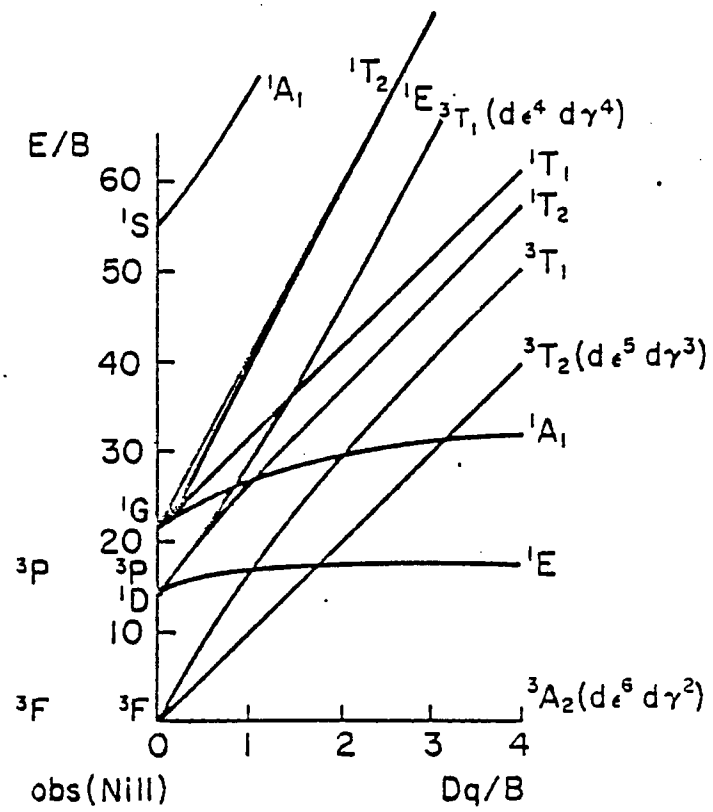

Figure 16. Tunabe-Sugano Diagram for Ni^{2+}

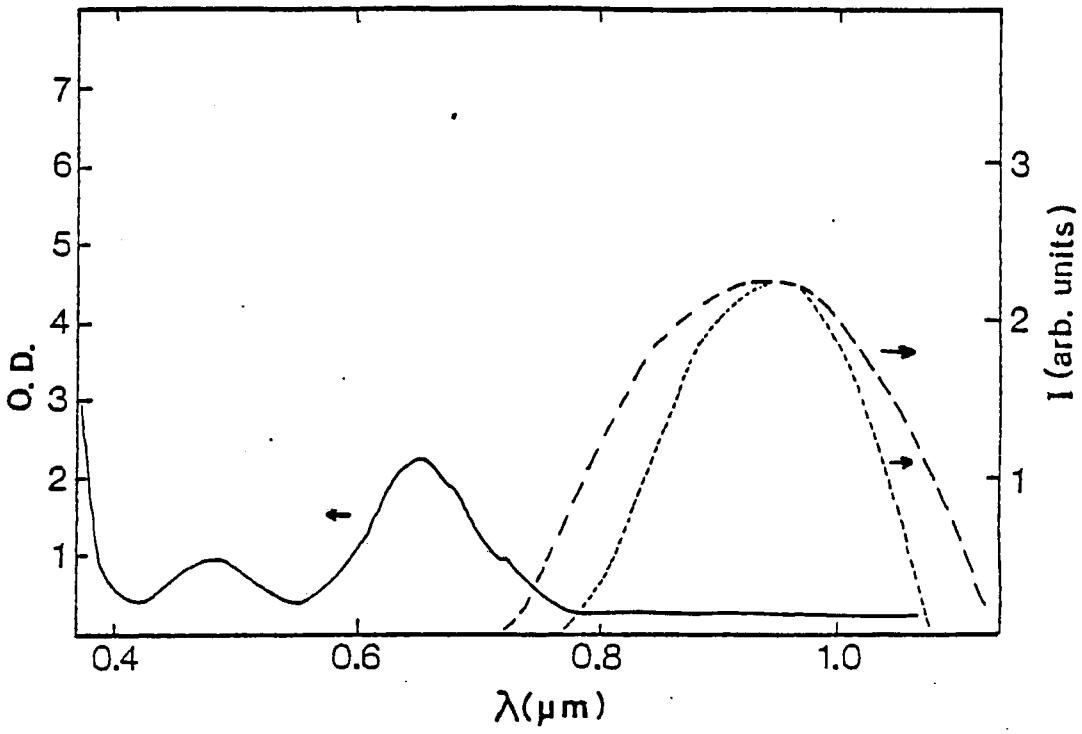

Figure 17. Room Temperature Absorption (solid line) and Fluorescence (broken line) Spectra of Cr^{3+} in $LiNbO_3$:MgO,Cr^{3+}

TABLE IX

ENERGY LEVEL ASSIGNMENTS OF Cr^{3+}
IN $LiNbO_3$:MgO,Cr^{3+}

λ (nm)	Energy (cm^{-1})	Energy Level Assignment
	0	$^2A_2$
720	13888	^2E
680	14705	$^2T_1$
650	15385	$^2T_2$
480	20833	$^4T_1$

nm. The Tunabe-Sugano diagram for Cr^{3+} which has a d^3 electronic configuration is shown in Fig. 18.

The fluorescence spectrum of $LiNbO_3$:MgO,Cr^{3+} was obtained by pumping ions into the $^4T_1$ level of chromium with the emission of a Coumarin 500 dye that is pumped with the emission of a N_2 laser. Figure 17 shows the low temperature (12 K) and room temperature fluorescence of $LiNbO_3$:MgO,Cr^{3+}. The broadband emission that peaks at 925 nm is due to the transition from the $^4T_2$ level to the $^4A_2$ level in chromium. Using the Tanabe-Sugano diagram for d^3 ions [48] and the absorption spectrum, the crystal field splitting was determined to be 14942 cm^{-1}. This crystal field splitting was calculated using the Racah parameter value for B of 482 cm^{-1} [52]. No "R" lines were seen in the room temperature luminescence because the probability of nonradiative decay from the ^{2}E state is much greater than the probability of radiative decay by approximately 10 orders of magnitude [52]. The $^4T_2$ level drops below the ^{2}E level and decreases the probability of radiative decay from the ^{2}E level. The emission cross section for chromium estimated from spectral parameters is listed in Table X.

The 1/e value of the fluorescence lifetime is plotted versus temperature for $LiNbO_3$:MgO,Cr^{3+} and is shown in Fig. 19. Below room temperature, the lifetime of chromium in $LiNbO_3$ was double exponential and this may be due to the Cr^{3+} ion occupying both the Li and the Nb sites in the host. When room temperature was reached, the fluorescence decay became single exponential. The 1/e value of the fluorescence lifetime was constant up to a temperature of 100 K and began to decrease with temperature up to a temperature of 300 K. This rapid decrease in lifetime was attributed to nonradiative processes.

If the pump power is increased and the fluorescence lifetime is monitored, an effective "lifetime shortening" of the fluorescence decay is sometimes seen. This lifetime shortening takes place due to either stimulated emission or excited state absorption. Lifetime shortening was seen in $LiNbO_3$:MgO,Cr^{3+} and Fig. 20 shows the definite threshold that occurs at the onset of stimulated processes. The lifetime shortening occurs at a definite threshold value of the pump pulse energy referred

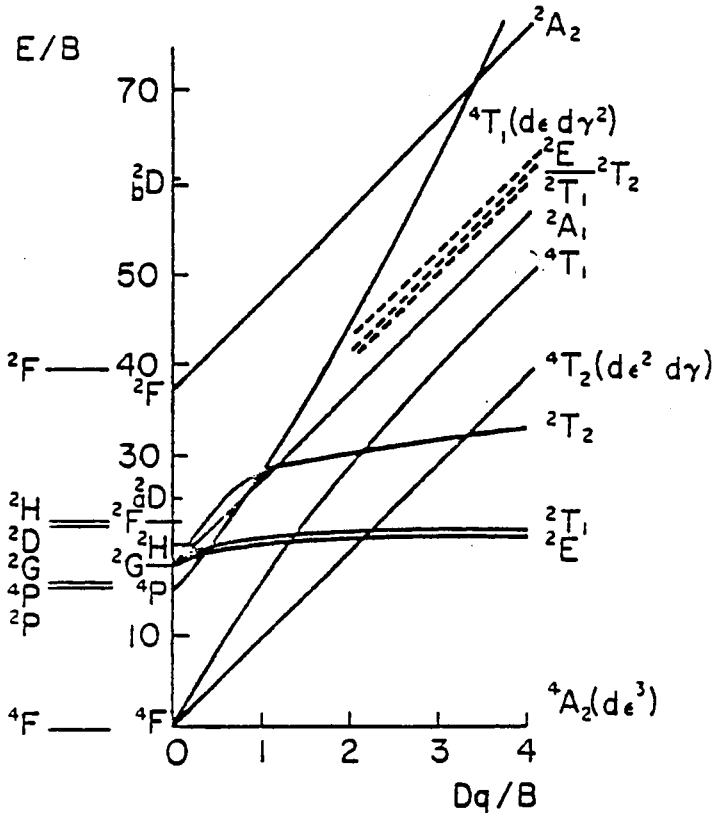

Figure 18. Tunabe-Sugano Diagram for Cr^{3+}

TABLE X

SAMPLE PARAMETERS OF $LiNbO_3$:MgO,Cr^{3+}

Parameter	$LiNbO_3$:MgO,Cr^{3+}
σ_{21} (cm^{-3})	1.4×10^{-19}
E_{th} (J)	0.1
$(N_2)_{th}$ (cm^{-3})	3.4×10^{18}
g (cm^{-1})	0.48

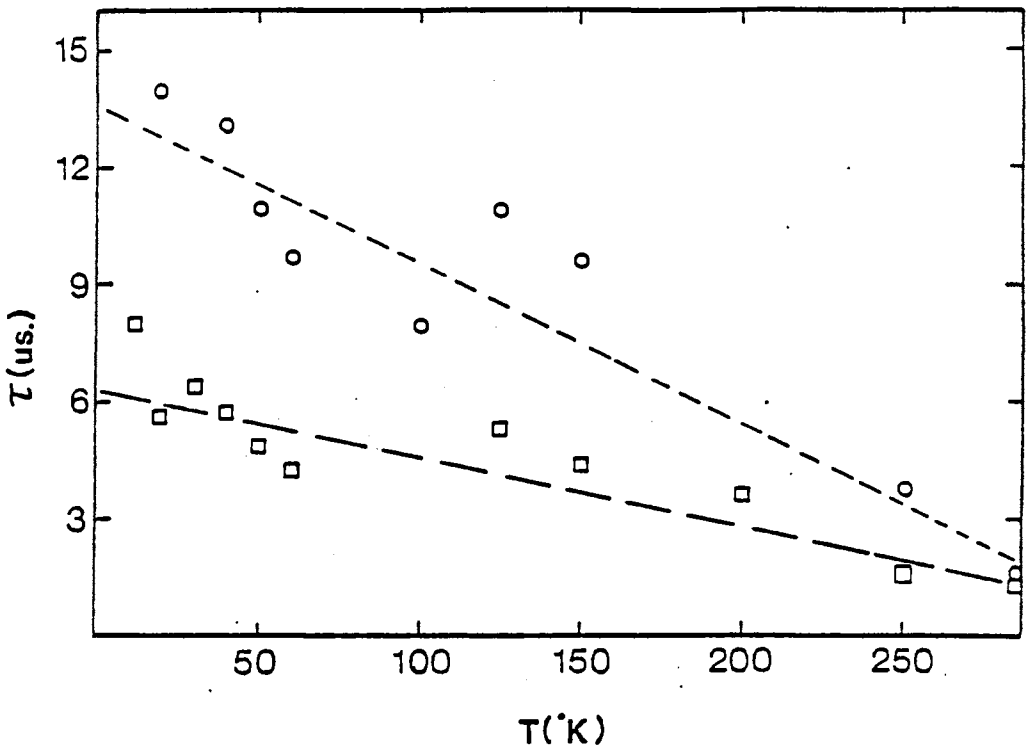

Figure 19. 1/e Value of the Fluorescence Decay Versus Temperature of Cr^{3+} in $LiNbO_3$:MgO

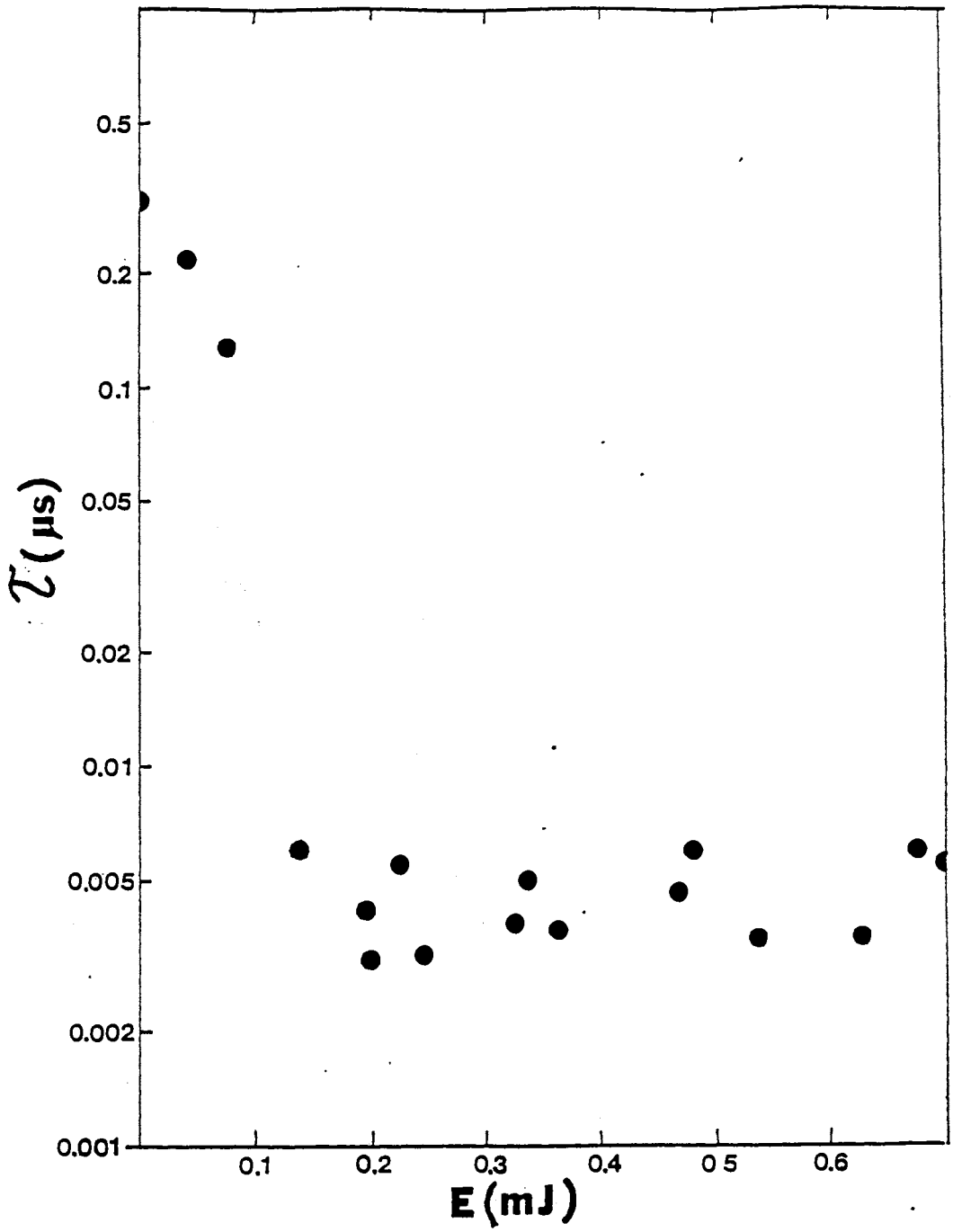

Figure 20. Lifetime Shortening in $LiNbO_3$:MgO,Cr^{3+}

to as E_{th} [32]. If the lifetime shortening takes place due to stimulated emission, then the population of the upper state at threshold is given from Eq. (4) as [32]

$$(N_2)_{th} = \frac{E_{th}}{h\nu}, \tag{31}$$

where ν is the frequency of the pump pulse.

With the stimulated emission cross-section obtained from the spectral parameters given from Eq. (1) and the population inversion at threshold from Eq. (4), the peak gain of the material is given by Eq. (6) as [32]

$$g = \sigma_{21}(N_2)_{th}. \tag{32}$$

The peak gain was estimated in this manner and is given in Table X.

An attempt was made to lase $LiNbO_3$:MgO,Cr^{3+} by placing it into a cavity consisting of a 97 % output coupler and a high reflecter coated from 800 nm to 1100 nm and then side pumping the system with the second harmonic of a nanosecond Nd:YAG laser. Fluences of 2.5 J/cm^2 were obtained with surface damage occurring on the pumped material at fluences greater than 650 mJ/cm^2. Lasing of the material was not achieved because the material was not able to absorb a large amount of the pump energy at 532 nm and damage to the crystal occurred around the energy density needed for gain to be seen. The samples were AR coated and again placed in a cavity and side-pumped with the emission of an alexandrite laser operating at 735 nm. Thermal cracking in each sample was observed before lasing could be achieved. $LiNbO_3$:MgO,Cr^{3+} did not lase at low temperatures even though the number of phonon processes that caused the heating of the crystal were minimized [53]. At this time, even though $LiNbO_3$:MgO,Cr^{3+} has a very desirable broad absorption band for flashlamp pumping and a very broad fluorescence band in the near infrared giving it good tunability, the use of it as a room temperature laser material is very doubtful and the growth techniques might be improved to allow it to handle the heat load required of laser host materials.

Discussion and Conclusions

Three materials were investigated as possible new room temperature laser materials. They were $LiNbO_3$:MgO doped with Co^{2+}, Ni^{2+}, and Cr^{3+}. Each material exhibited a broad absorption band characteristic of the absorption transitions of transition metal ions. There was no room temperature fluorescence from $LiNbO_3$:MgO,Co^{2+} or $LiNbO_3$:MgO,Ni^{2+} eliminating them as possible room temperature laser materials. From the initial spectroscopy, $LiNbO_3$:MgO,Cr^{3+} appears to be a very promising room temperature laser material. The broad absorption of the Cr^{3+} ion in $LiNgO_3$:MgO makes flash lamp pumping possible and the broad fluorescence band peaked at 925 nm allows the possibility of tunability over a wide spectral range in the near IR. Thermal effects cause the material to crack during laser pumping at room temperature making this material impractical as a room temperature laser material.

CHAPTER V

SPECTROSCOPIC STUDY OF $LiNbO_3$:MgO,Cr^{3+},RE

Introduction

$LiNbO_3$:MgO,Cr^{3+} has been doped with a variety of rare earth ions to investigate the use of lithium niobate as a laser host material. The magnesium was introduced in the crystals to reduce optical damage effects and the Cr^{3+} ions provide broad absorption bands for pumping and a broad emission band for energy transfer to rare earth ions. The rare earth ions provide the sharp emission transitions for laser action and their energy levels are shown in Fig. 21 in the host $LaCl_3$. The rare earth ions investigated were Tm^{3+}, Ho^{3+}, Nd^{3+}, Er^{3+}, and Yb^{3+}. Figure 22 shows the absorption spectrum of Cr^{3+} in $LiNbO_3$:MgO (solid line) and the emission spectrum (broken line) along with the positions of several of the rare earth energy levels whose transitions are in resonance with the emission band of Cr^{3+}. The energy transfer from Cr^{3+} to R.E. was investigated and the results are discussed in this chapter.

The samples investigated below were of good optical quality and were grown by the Czochralski technique in the crystal growth facility at Oklahoma State University. As reported earlier, the magnesium quenches the photorefractive effect that takes place in $LiNbO_3$ and also alleviates the crystal-cracking problem during growth [44]. The samples consisted of a single crystal of $LiNbO_3$ doped with 4.5 % MgO, 0.05 % Cr_2O_3, and different concentrations of the rare earth ion.

$LiNbO_3$:MgO,Cr^{3+},Tm^{3+}

$LiNbO_3$:MgO,Cr^{3+} was doped with 0.05 % of Tm_2O_3. Tm^{3+} has been shown to lase in $LiNbO_3$ in the past at 77 K at an emission wavelength of 1.82

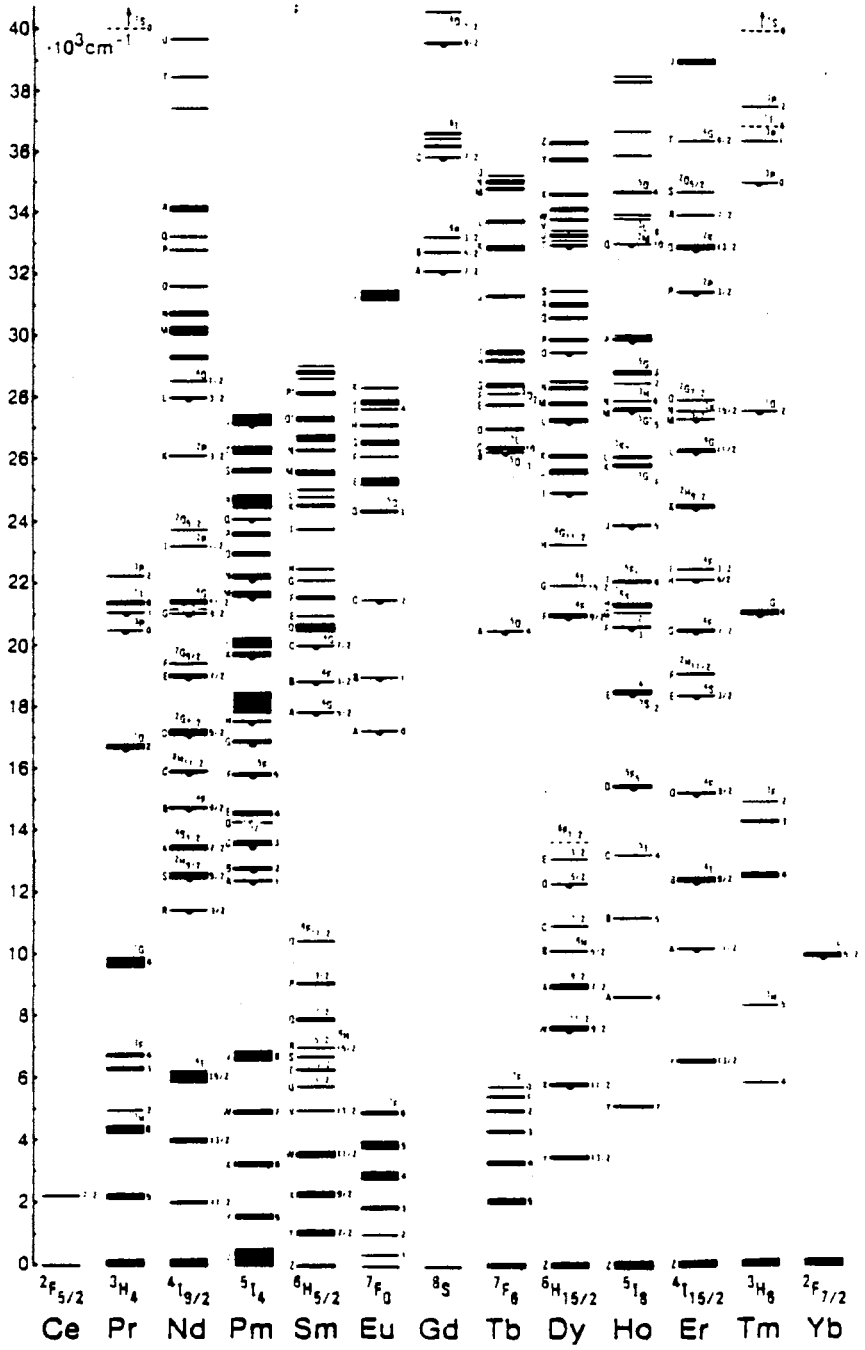

Figure 21. Energy Levels of the Triply Ionized Rare Earths in $LaCl_3$

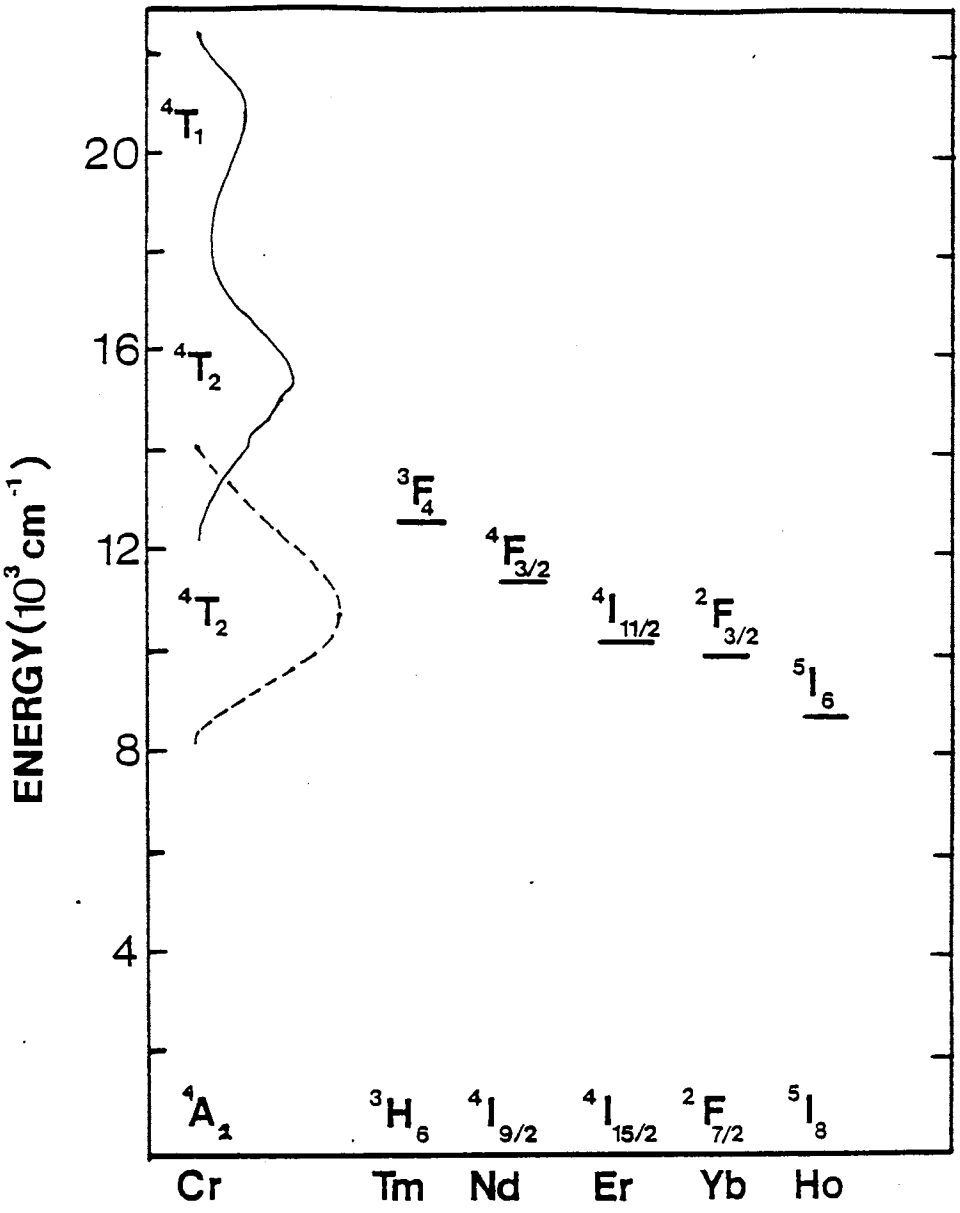

Figure 22. Spectrum of Cr^{3+} in $LiNbO_3$:MgO and Resonant RE Energy Levels

μm in the pulse mode of operation [54] and Tm^{3+} has lased in YAG and $YAlO_3$ at room temperature [55]. The focus of this investigation was to pump the broad absorption band of Cr^{3+} in $LiNbO_3$ and then via energy transfer attempt to lase the Tm^{3+}.

$LiNbO_3$:MgO,Cr^{3+},Tm^{3+} was grown and contained a concentration of Cr^{3+} of 1.7×10^{19} cm^{-3} and of Tm of 3.4×10^{19} cm^{-3}. The sample was 0.2 cm thick. The room temperature absorption spectrum of $LiNbO_3$:Mgo,Cr^{3+},Tm^{3+} was measured with a Perkin-Elmer Spectrophotometer Model 330 and is shown as a solid line in Fig. 23. The absorption spectrum was measured in optical density and the thickness of the material was 0.12 cm. The broad structure in the absorption spectrum was due to Cr^{3+} and the sharp features were due to Tm^{3+}. The energy levels were assigned to the peaks and are given in Table XI. An attempt was made to measure the room temperature fluorescence of Tm^{3+} by pumping ions into the $^4T_1$ level of chromium. It was anticipated that there would be energy transfer from the emission of the $^4T_2$ level of chromium to the $^3H_6$ to $^3F_4$ absorption transition in Tm^{3+}. There was no detectable thulium emission from the $^3F_4$ level and it was concluded that there was no energy transfer from the chromium to the thulium. This was probably due to insufficient thulium concentration in the material. It is also possible that there is too small of an overlap between the chromium emission and the absorption transition of the thulium. Since there was no thulium emission and no energy transfer, this material with its present concentration of impurities was eliminated as a possible laser material.

$LiNbO_3$:MgO,Cr^{3+},Ho^{3+}

$LiNbO_3$:MgO,Cr^{3+} was doped with 0.20 % of Ho_2O_3. Ho^{3+} has also been shown to lase in $LiNbO_3$ at 77 K at an emission wavelength of 2.08 μm in the pulse mode of operation [54] and Ho^{3+} has also lased in YAG [55]. The focus of this investigation was to optically pump the broad absorption band of Cr^{3+} in $LiNbO_3$ and then via energy transfer attempt to lase the Ho^{3+}.

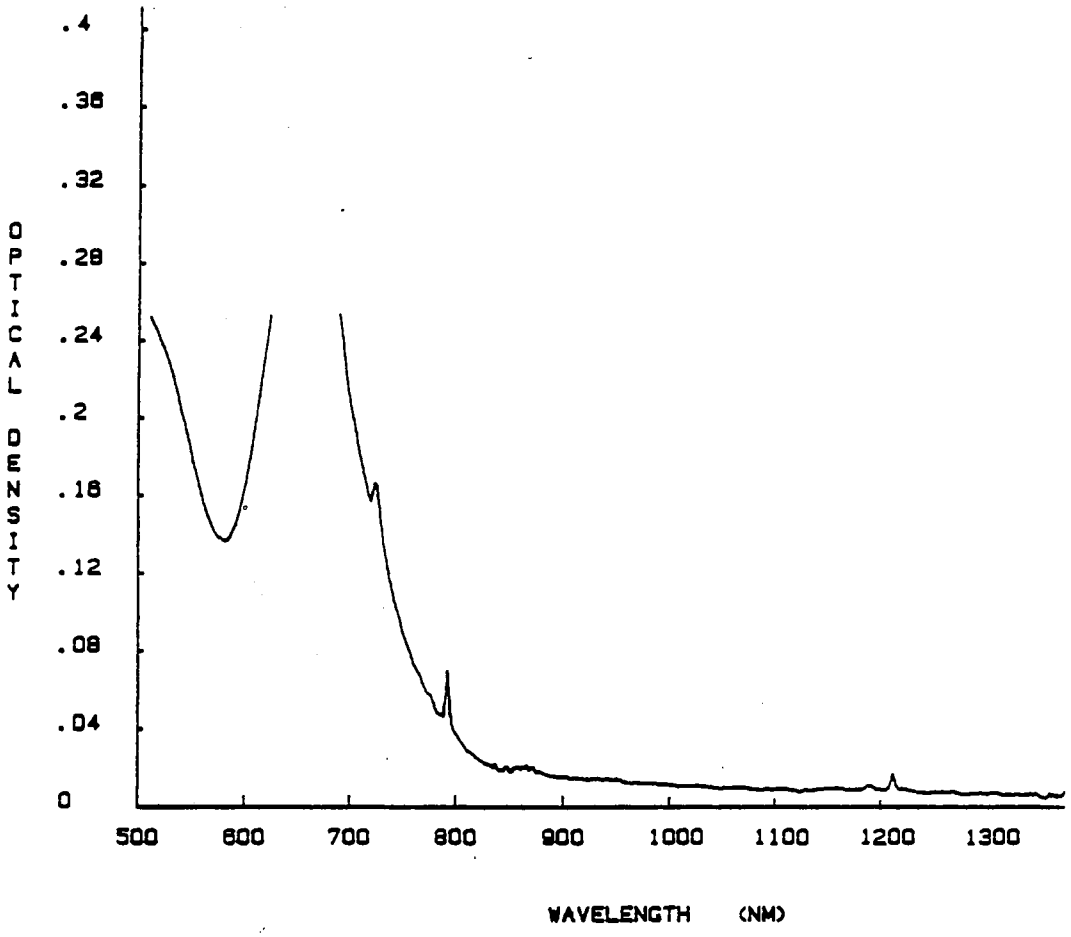

Figure 23. Room temperature Absorption of $LiNbO_3$:MgO,Cr^{3+},Tm^{3+}

TABLE XI

ENERGY LEVEL ASSIGNMENTS OF Tm^{3+} IN $LiNbO_3$:MgO,Cr^{3+},Tm^{3+}

λ (nm)	Energy (cm^{-1})	Energy Level Assignment
	0	$^3H_6$
1672	5980	$^3H_5$
1183	8453	$^3H_4$
794	12594	$^3F_4$

$LiNbO_3$:MgO,Cr^{3+},Ho^{3+} was grown and contained a concentration of Cr^{3+} of 9×10^{18} cm^{-3} and of Ho^{3+} of 1.5×10^{19} cm^{-3}. The room temperature absorption spectrum of $LiNbO_3$:MgO,Cr^{3+},Ho^{3+} was measured on a material of thickness of 0.19 cm with a Perkin-Elmer Spectrophotometer Model 330 and is shown as a solid line in Fig. 24. The broad structure of the absorption spectrum was due to Cr^{3+} and the sharp features were due to Ho^{3+}. The energy levels were assigned to the peaks and are given in Table XII. An attempt was made to measure the room temperature fluorescence of the holmium emission under chromium excitation of the $^4T_2$ level of chromium. There was no measurable Ho^{3+} emission from the $^5I_6$ level and it was assumed that no energy transfer from the chromium to the holmium was taking place. This was probably due to the small overlap of the $^5I_8$ to $^5I_6$ absorption transition in Ho^{3+} with the emission of the $^4A_2$ to $^4T_2$ transition of chromium.

$LiNbO_3$:MgO,Cr^{3+},Nd^{3+}

$LiNbO_3$:MgO,Cr^{3+} was doped with 0.05 % of Nd_2O_3. Nd^{3+} has been shown to lase in $LiNbO_3$ in the past [56,54,57,42] but the focus of this investigation was to optically pump the broad absorption band of Cr^{3+} in $LiNbO_3$ and then via energy transfer attempt to lase the Nd^{3+}. Nd^{3+} is a rare earth with $4f^3$ configuration and the energy levels are shown in Fig. 21. Nd^{3+} can substitute into either the Li^+ or the Nb^{5+} site in $LiNbO_3$ and co-doping the crystal with MgO will increase the distribution coefficient of Nd in $LiNbO_3$ [58,59]. The concentration of Cr^{3+} in the sample was 1.7×10^{19} cm^{-3} and the concentration of Nd^{3+} was 3.8×10^{18} cm^{-3}. The sample thickness was measured to be 0.28 cm.

The room temperature absorption spectrum of $LiNbO_3$:MgO,Cr^{3+},Nd^{3+} was measured on a sample having a thickness of 0.14 cm with a Perkin-Elmer Spectrophotometer Model 330 and is shown as a solid line in Fig. 25. The broad structure of the absorption spectrum was due to Cr^{3+} and the sharp features were due to Nd^{3+}. The energy levels of Nd^{3+} were assigned to the peaks of the absorption spectra and are given in Table XIII.

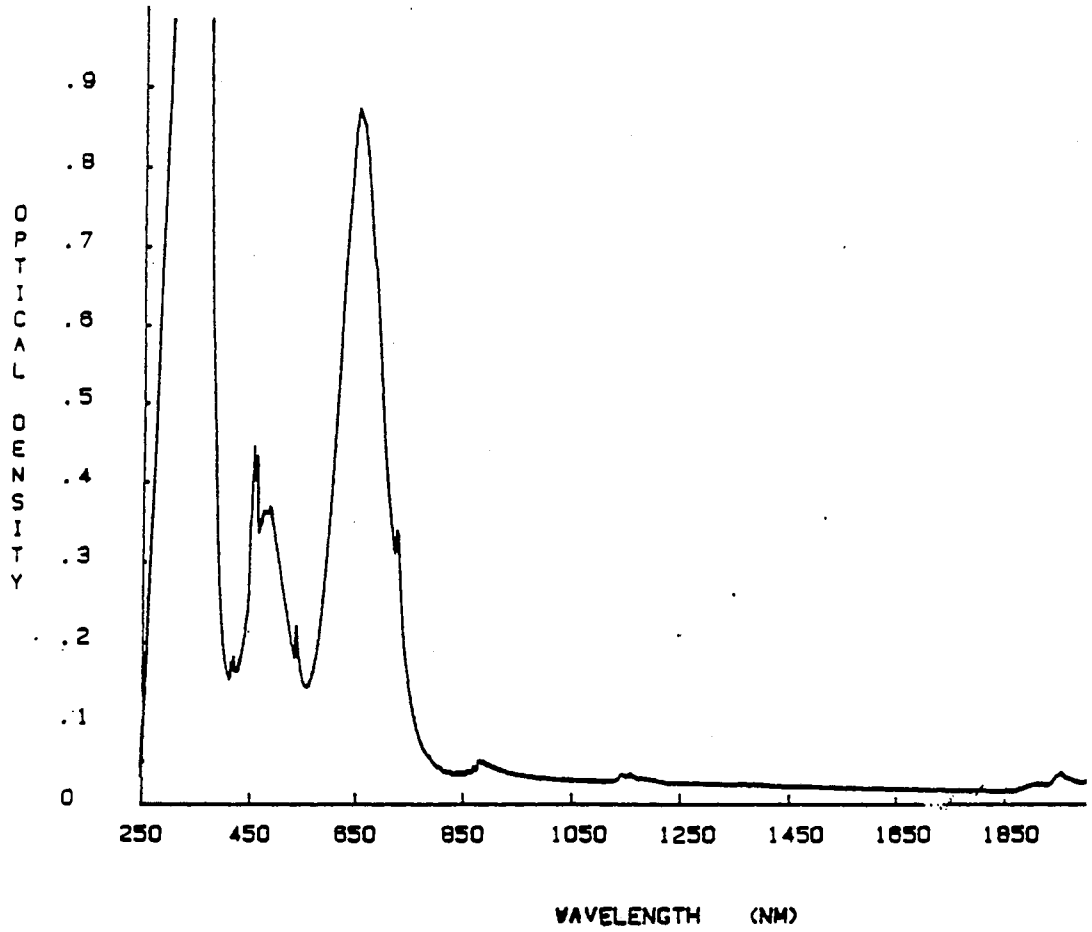

Figure 24. Room Temperature Absorption of $LiNbO_3$:MgO,Cr^{3+},Ho^{3+}

TABLE XII

ENERGY LEVEL ASSIGNMENTS OF Ho^{3+} IN $LiNbO_3$:MgO,Cr^{3+},Ho^{3+}

λ (nm)	Energy (cm^{-1})	Energy Level Assignment
	0	$^5I_8$
1905	5249	$^5I_7$
1143	8748	$^5I_6$
870	11494	$^5I_5$
750	13333	$^5I_4$

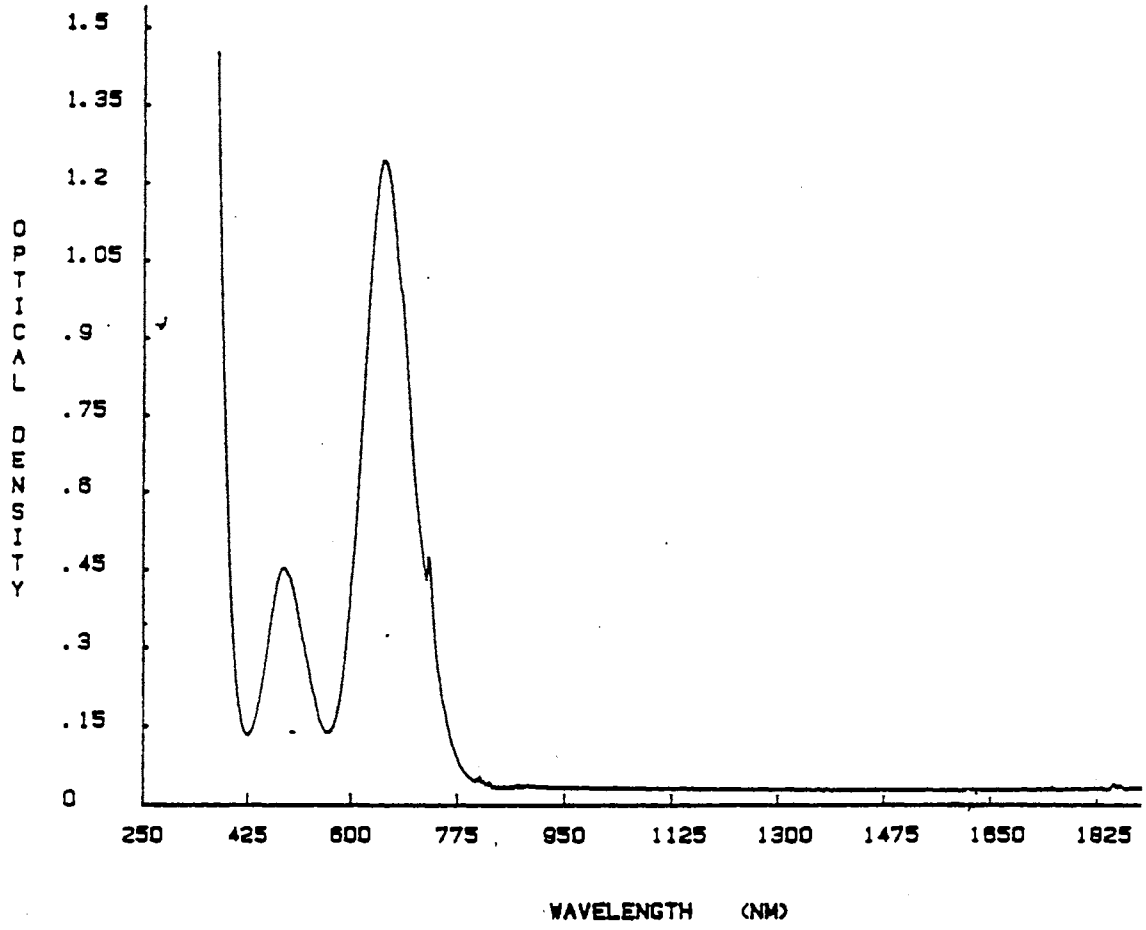

Figure 25. Room Temperature Absorption of $LiNbO_3$:MgO,Cr^{3+},Nd^{3+}

TABLE XIII

ENERGY LEVEL ASSIGNMENTS OF Nd^{3+} IN $LiNbO_3$:MgO,Cr^{3+},Nd^{3+}

λ (nm)	Energy (cm^{-1})	Energy Level Assignment
	0	$^4I_{9/2}$
4926	2030	$^4I_{11/2}$
2532	3950	$^4I_{13/2}$
1704	5870	$^4I_{15/2}$
871	11480	$^4F_{3/2}$
828	12070	$^4F_{5/2} +^2 H_{9/2}$

An attempt was made to measure the room temperature fluorescence of the neodymium emission under chromium excitation of the $^4T_2$ level of chromium. There was no measurable Nd^{3+} emission from the $^4F_{3/2}$ level and it was assumed that no energy transfer from the chromium to the neodymium was taking place. This was probably due to an insufficient neodymium concentration in the sample.

$LiNbO_3$:MgO,Cr^{3+},Er^{3+}

$LiNbO_3$:MgO,Cr^{3+} was doped with 0.20 % of Er_2O_3 and the sample investigated was 0.14 cm thick. The room temperature absorption spectrum of $LiNbO_3$:MgO,Cr^{3+},Er^{3+} was measured with a Perkin-Elmer Spectrophotometer Model 330 and is shown as a solid line in Fig. 26. The broad structure was due to Cr^{3+} and the sharp features were due to Er^{3+}. The energy levels for Er^{3+} were assigned to the peaks of the absorption spectra and are given in Table XIV.

The room temperature fluorescence of the erbium emission under chromium excitation of the $^4T_2$ level of chromium was measured and is shown in Fig. 27. There was no strong erbium emission seen but the absorption of the $^4I_{11/2}$ and $^4I_{13/2}$ levels of Er^{3+} were seen in the spectra of the chromium emission. This material was also eliminated as a possible room temperature laser material since no room temperature fluorescence was detected.

$LiNbO_3$:MgO,Cr^{3+},Yb^{3+}

Spectroscopy

The absorption spectrum of $LiNbO_3$:MgO,Cr^{3+},Yb^{3+} was measured with a Perkin-Elmer Spectrophotometer Model 330 on a sample 0.2 cm thick and is shown as the solid lines in Figure 28. The solid line represents the absorption of the material, the broken line represents the emission of the chromium at short times after the pulse and the ytterbium absorption embedded in the chromium fluorescence, and the dashed line represents the ytterbium emission at long times after the excitation pulse. The energy levels of Yb^{3+} were assigned to the peaks

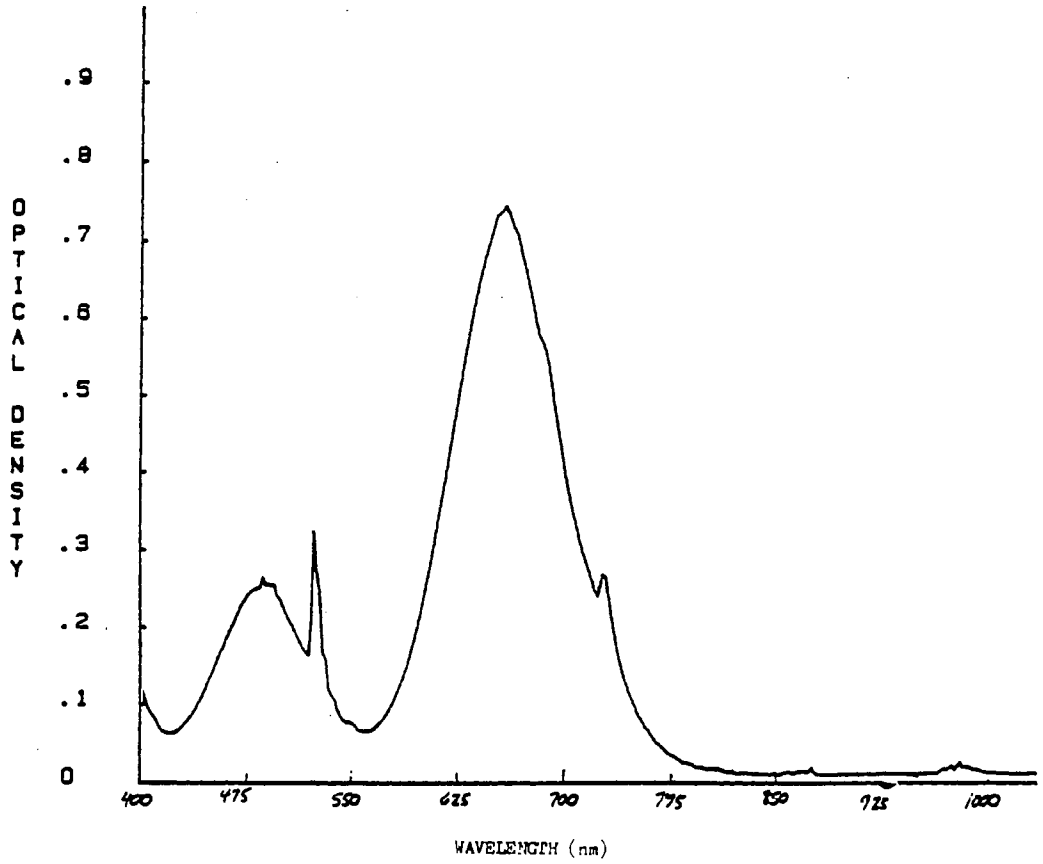

Figure 26. Room Temperature Absorption of $LiNbO_3$:MgO,Cr^{3+},Er^{3+}

TABLE XIV

ENERGY LEVEL ASSIGNMENTS OF Er^{3+} IN $LiNbO_3$:MgO,Cr^{3+},Er^{3+}

λ (nm)	Energy (cm^{-1})	Energy Level Assignment
	0	$^4I_{15/2}$
1517	6592	$^4I_{13/2}$
977	10235	$^4I_{11/2}$
809	12361	$^4I_{9/2}$

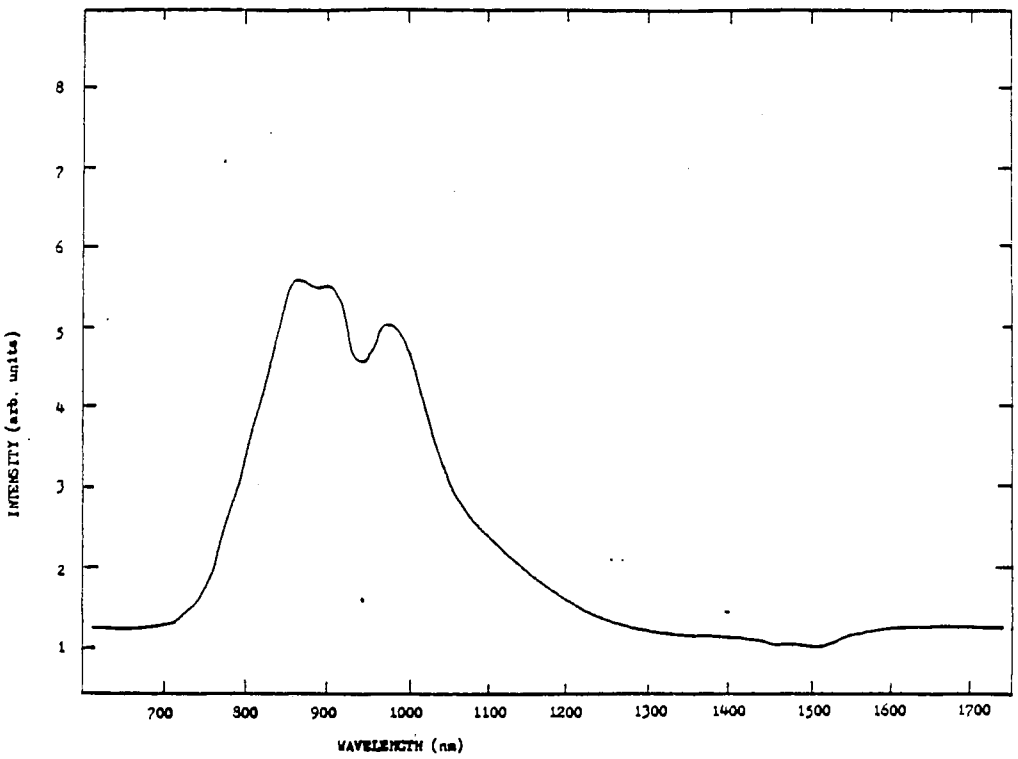

Figure 27. Room Temperature Fluorescence of $LiNbO_3$:MgO,Cr^{3+},Er^{3+}

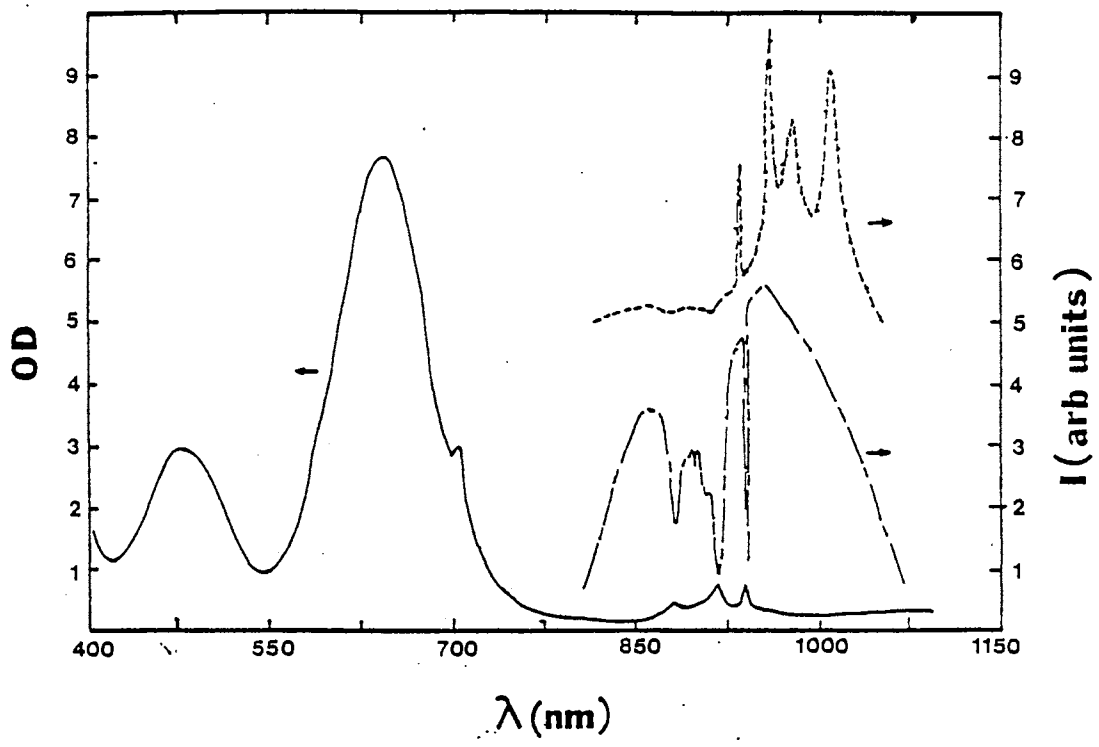

Figure 28. Absorption Spectrum (solid line) and Fluorescence Spectrum at Short (broken line) and Long (dashed line) After the Excitation Pulse of $LiNbO_3$:MgO,Cr^{3+},Yb^{3+}

of the absorption spectra and are given in Table XV. The absorption spectrum exhibits the characteristic transitions from the $^4A_2$ level to the $^4T_1$ level of Cr^{3+} peaked at 480 nm and the transition from the $^4A_2$ level to the $^4T_2$ level of Cr^{3+} peaked at 650 nm. The transition from the $^2F_{7/2}$ ground state to the $^2F_{3/2}$ excited state of ytterbium was located spectrally at 925 nm. The fluorescence spectrum of $LiNbO_3$:MgO,Cr^{3+},Yb^{3+} was measured after exciting the chromium $^4T_1$ level with the emission of a Coumarin 500 dye that is pumped with the emission of a N_2 laser.

The 1/e value of the fluorescence decay versus temperature of both $LiNbO_3$:MgO,Cr^{3+} and $LiNbO_3$:MgO,Cr^{3+},Yb^{3+} is shown in Fig. 29. The 1/e value of the decay was used because, as reported in the previous chapter, the lifetime of the $^4T_2$ state of Cr^{3+} was multi-exponential. A simple two-level model described by the equation

$$\frac{1}{\tau} = \frac{1}{\tau_L} + C\exp(\frac{-\Delta E}{kT}) \tag{33}$$

where τ is the fluorescence lifetime, τ_L is the lifetime at low temperatures, and ΔE was the energy difference between the $^4T_2$ level and the $^4A_2$ level was used to describe the change in lifetime with change in temperature. A ΔE of 618 cm^{-1} is found for both $LiNbO_3$:MgO,Cr^{3+} and $LiNbO_3$:MgO,Cr^{3+},Yb^{3+}, indicating that the Yb^{3+} ion does not alter the energy difference of the $^4T_2$ to the $^4A_2$.

Energy Transfer

Time-resolved site-selection spectroscopy (TRSSS) measurements were used to characterize the properties of short range energy transfer from the Cr^{3+} ions to the Yb^{3+} ions in $LiNbO_3$:MgO,Cr^{3+},Yb^{3+}. The absorption of Yb^{3+} occurs in the emission of Cr^{3+} and is shown in Fig. 22, indicating a direct absorption of the Cr^{3+} emission by the Yb^{3+} ions and making nonradiative energy transfer from Cr^{3+} to Yb^{3+} probable. The emission of a dye laser using Coumarin 500 dye was used to selectively excite the Cr^{3+} ions. The fluorescence was directed through a one-meter Spex monochromator and detected with an RCA 7102 photomultiplier

TABLE XV

ENERGY LEVEL ASSIGNMENTS OF Yb^{3+} IN
$LiNbO_3$:MgO,Cr^{3+},Yb^{3+}

λ (nm)	Energy (cm^{-1})	Energy Level Assignment
	0	$^2F_{7/2}$
925	10811	$^2F_{3/2}$

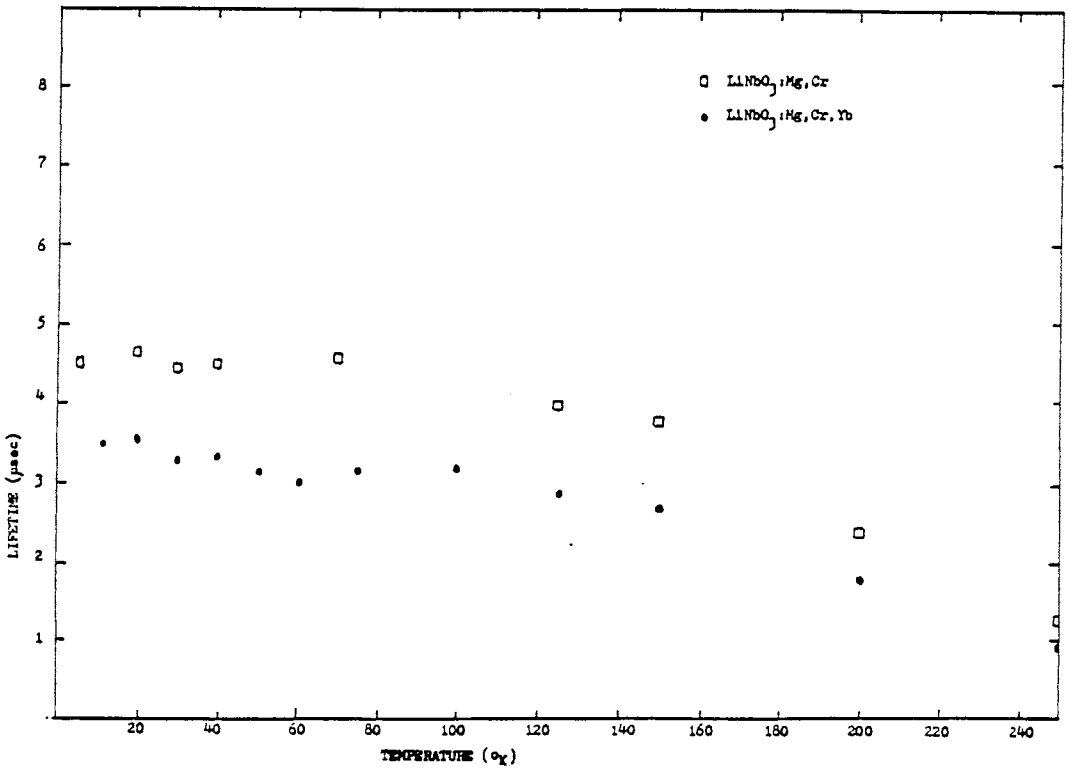

Figure 29. 1/e Value of the Fluorescence Decay as a Function of Temperature.

tube. A boxcar integrator was used and the results were printed onto a chart recorder.

Energy transfer occurred from Cr^{3+} to Yb^{3+} and this was seen by the Cr^{3+} emission band for short and long times after chromium excitation as shown in Fig. 28. At short times after excitation of the $^4T_2$ band of Cr^{3+}, the absorption of Yb^{3+} was seen in the Cr^{3+} band; however, at longer times when the emission of the chromium ion is relatively weak, the Yb^{3+} emission becomes apparent. It was important to determine the type and strength of the energy transfer mechanism and whether the energy transfer was a resonant or phonon-assisted process. The primary parameter of concern is the energy transfer rate W_{sa}.

The lifetime of the decay versus temperature for $LiNbO_3$:MgO,Cr^{3+},Yb^{3+} and $LiNbO_3$:MgO,Cr^{3+} was plotted to determine if the energy transfer rate was temperature dependent. The effective lifetime of $LiNbO_3$:MgO,Cr^{3+} can be described as

$$(\frac{1}{\tau})_{eff} = (\frac{1}{\tau})_f, \tag{34}$$

and the effective lifetime of $LiNbO_3$:MgO,Cr^{3+},Yb^{3+} can be described as

$$(\frac{1}{\tau})'_{eff} = (\frac{1}{\tau})'_f + W_{sa} \tag{35}$$

where $(\frac{1}{\tau})_f$ is the fluorescence lifetime which has a radiative and a nonradiative component. If the chromium ions are in the excited state, then the transfer of energy from the chromium to the ytterbium is an addition decay mechanism called the average energy transfer rate given as W_{sa} in Eq. (35). Assuming that the presence of the ytterbium does not introduce structural changes in the crystal and that

$$(\frac{1}{\tau})_f = (\frac{1}{\tau})'_f, \tag{36}$$

then the average energy transfer rate is given by

$$(W_{sa})_{avg} = (\frac{1}{\tau})'_{eff} - (\frac{1}{\tau})_{eff}. \tag{37}$$

By taking the measured fluorescence lifetime as the effective lifetime, the average energy transfer rate was determined and the results are shown in Fig. 30.

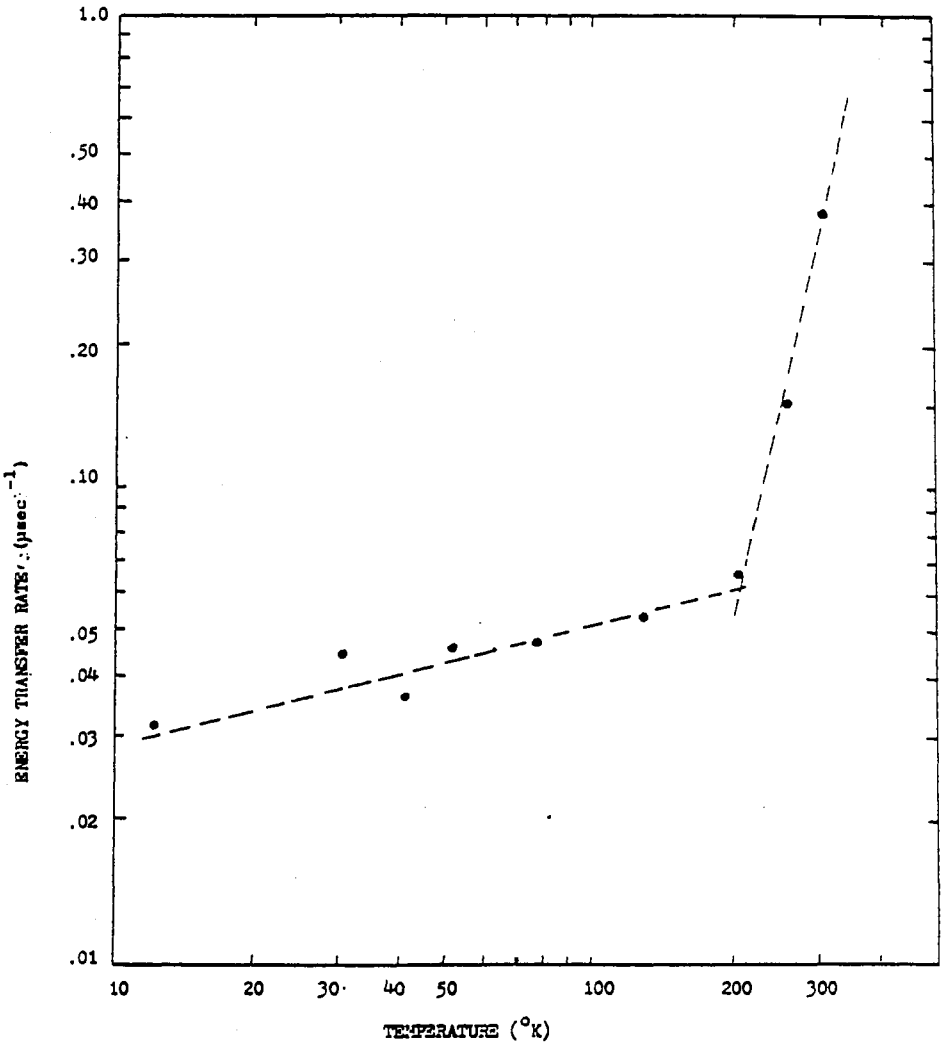

Figure 30. $(W_{sa})_{avg}$ Versus T

The average energy transfer rate increased dramatically at 200 K, indicating that this energy transfer process was a phonon-assisted process.

The energy transfer rate can also be approximated by [60]

$$(W_{sa})_{avg} = (\frac{1}{\tau})_{cr}(\frac{R}{R_o})^6, \tag{38}$$

where R is the distance from the chromium ion to the ytterbium ion in the crystal, and τ_{cr} is the lifetime of the chromium ion in the excited state. The value of R was determined to be 0.162 nm and using Eq. (38), the critical interaction distance, R_o, at which the energy transfer rate equals the intrinsic decay rate was calculated. These values are given in Table XVI.

The critical interaction distance can also be determined from spectral parameters for a dipole-dipole interaction mechanism by using [60,61]

$$R_o = [(\frac{3h^4c^4}{4\pi n^4}) \cdot \rho_A \cdot \int (f_e(E) f_a(E)/E^4 dE)]^{1/6}. \tag{39}$$

In this equation, n is the index of refraction of the material, $f_e(E)$ is the normalized emission lineshape, $f_a(E)$ is the normalized absorption lineshape, and $\rho_A = \int \sigma(\nu) d\nu$ is the integrated absorption cross section. The room temperature value for R_o obtained from spectral parameters was 1.16 nm which is 23 % smaller than R_o obtained from a lifetime analysis. The discrepancy between values for R_o comes from the error introduced when determining the absorption and emission lineshapes and the overlap integrals.

The time evolution of the fluorescence of the chromium and the absorption/fluorescence of the Yb^{3+} in $LiNbO_3$:MgO,Cr^{3+},Yb^{3+} at different times was also investigated. There was a change in the ratios of the integrated fluorescence intensities of the chromium sites (sensitizers) to that of the ytterbium sites (activators). The values of the integrated fluorescence intensities are listed in Table XVII. There was an initial buildup of the chromium emission along with absorption of the ytterbium in the chromium band. As the intensity of the chromium emission decreased, the ytterbium fluorescence intensity increased. At long times only ytterbium emission was seen, implying that there was no back transfer.

TABLE XVI

THE AVERAGE ENERGY TRANSFER RATE AND CRITICAL INTERACTION DISTANCE AS A FUNCTION OF TEMPERATURE AS DETERMINED FROM THE FLUORESCENCE LIFETIME

T (K)	$\tau'(\mu s)$	$\tau(\mu s)$	$(W_{sa})_{avg}$ (s^{-1})	$R_o(nm)$
12	7.02	9.06	0.032	1.32
30	6.55	9.31	0.045	1.40
40	6.68	8.90	0.037	1.35
50	6.35	9.04	0.047	1.40
75	6.33	9.11	0.048	1.41
125	5.73	7.96	0.049	1.39
150	5.39	7.58	0.054	1.39
200	3.62	4.78	0.067	1.34
250	1.81	2.60	0.150	1.39
295	1.06	1.78	0.382	1.52

TABLE XVII

TIME EVOLUTION OF THE INTEGRATED AREA OF THE ACTIVATOR AND SENSITIZER FLUORESCENCE VERSUS TEMPERATURE

	Time after the pulse					
T (K)	5	10	25	50	75	100
$\frac{I_{yb}}{I_{cr}}$						
12	0.0	0.0	2.87	9.70		24.56
50	0.0	0.0	1.53	4.06	9.97	
100	0.0	0.0	1.08	3.56		
200	0.0	0.0	3.06			

The time evolution of the ratios was modeled using a phenomenological rate parameter model illustrated in Fig. 31. The sensitizer ions were those in the site that are preferentially excited by the laser at a rate W_{sa}, whereas the activators were ions at sites that receive energy through energy transfer. n_a and n_s were the concentrations of the ions in the excited states, W_{sa} was the rate of energy transfer from sensitizer to activator, and β_s and β_a were the fluorescence decay rates associated with each type of site. Thus, the rate equations describing the time evolution of the populations of the excited states were written as

$$\dot{n}_s = W_s - \beta_s n_s - W_{sa} n_s, \tag{40}$$

$$\dot{n}_a = -\beta_a n_a + W_{sa} n_s. \tag{41}$$

The equations were solved assuming a delta-function excitation pulse, negligible back-transfer, and an explicit time dependence for the energy transfer rate. The best fits to the data for both low and high temperatures were obtained with an energy transfer rate which varies as $t^{1/2}$ indicating that a dipole-dipole interaction took place. The solutions to Equations (40) and (41) are given by

$$n_s(t) = n_s(0)\exp[-\beta_s t - 2\Omega t^{1/2}] \tag{42}$$

$$n_a(t) = n_s(0)[\exp[-\beta_s] - \exp[-\beta_s t - 2\Omega t^{1/2}]] + n_a(0)\exp[-\beta_a t] \tag{43}$$

where the time dependence of the energy transfer rate was written explicitly as $W_{sa} = \Omega t^{-1/2}$. The ratio of the integrated fluorescence intensities was proportional to the rate of the excited state populations and was written directly as

$$\frac{I_a(t)}{I_s(t)} = \left(\frac{\beta_{ar}}{\beta_{sr}}\right)\left[\left[\left(\frac{I_a(0)}{I_s(0)}\right)\left(\frac{\beta_{sr}}{\beta_{ar}}\right) + 1\right] \cdot \exp(2\Omega t^{1/2}) - 1\right] \tag{44}$$

where β_{ar} and β_{sr} are the radiative decay rates associated with the activator and sensitizer sites, respectively. As mentioned earlier, part of the transfer of energy

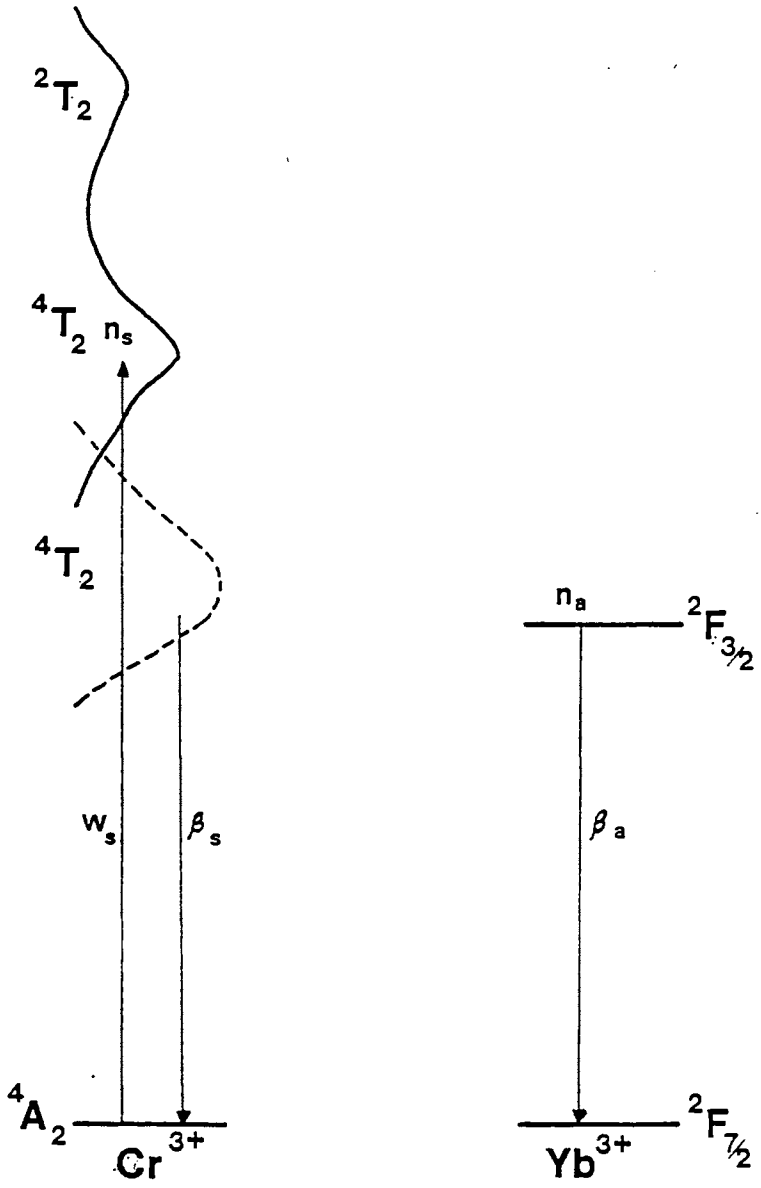

Figure 31. Rate Equation Diagram Used to Model the Energy Transfer Rate

from the Cr^{3+} to the Yb^{3+} was radiative and part of the energy transfer was nonradiative. Eq. (44) applies only to nonradiative energy transfer, so radiative energy transfer must be considered in order to be able to fit Eq. (44) to experimental data. At very short times when the fluorescence of the chromium was at a maximum, it was assumed that the amount of radiative transfer was at a maximum. The fraction f of radiative energy transfer was calculated by dividing the integrated intensity of the absorption of Yb^{3+} in the fluorescence of $LiNbO_3$3:MgO,Cr^{3+} by the integrated intensity of the fluorescence of $LiNbO_3$:MgO,Cr^{3+}. The correction for the ratio of integrated intensities when considering both radiative and nonradiative energy transfer is (1-f) and Eq (44) becomes

$$\frac{I_a(t)}{I_s(t)}(1-f) = (\frac{\beta_{ar}}{\beta_{sr}})[(\frac{I_a(0)}{I_s(0)})(\frac{\beta_{sr}}{\beta_{ar}} + 1] \cdot \exp(2\Omega t^{1/2}) - 1]. \tag{45}$$

The solid and broken lines in Figure 32 represent the best fits of Eq. (45) to the experimental data. Both $\frac{I_a(0)}{I_s(0)}$ and Ω were treated as adjustable parameters. The values for these parameters and for the fraction of radiative energy transfer are listed in Table XVIII.

It is possible to use the Forster-Dexter [60,61] expression for an electric dipole-dipole transfer rate and the rate equation model to find the value of the critical interaction distance, R_o. This expression is given by

$$R_o = [(\frac{\omega_{DD}}{N_a})(\tau_s^o)^{1/2}[(\frac{4}{3})\pi^{3/2}] - 1]^{1/3} \tag{46}$$

where $\omega_{DD} = W_{sa} = \Omega^{-1/2}$.

N_a is the total concentration of activators and τ_s^o is the lifetime of the sensitizer without the presence of activators. The values for R_o at different temperatures are given in Table XVIII. These values are even higher than the values for R_o reported previously in this chapter.

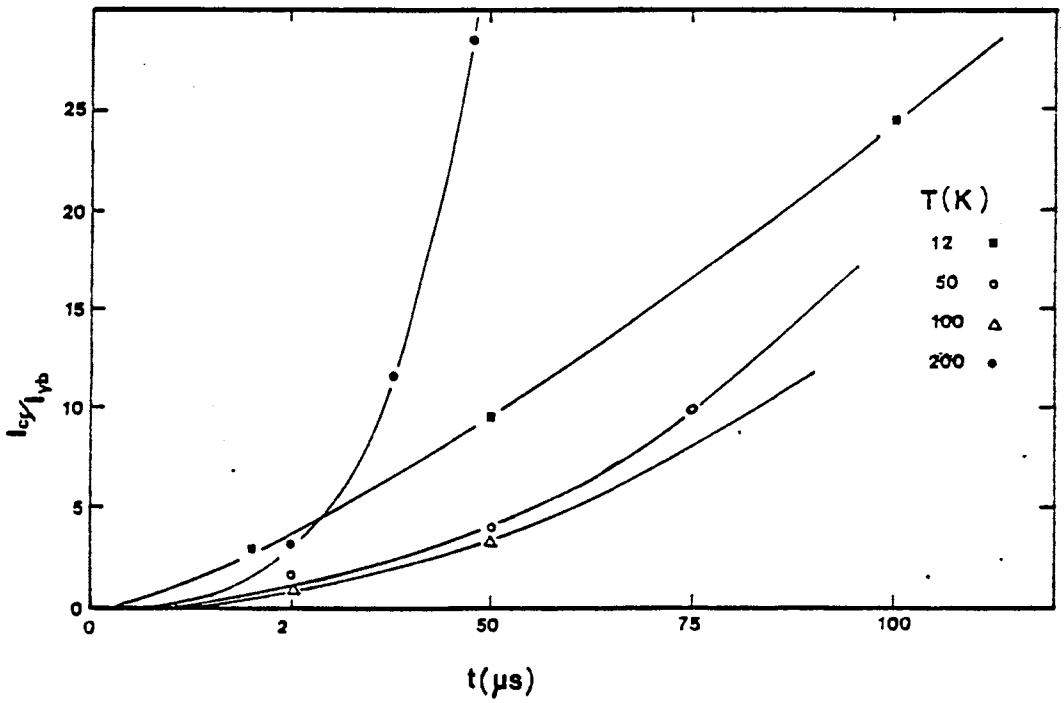

Figure 32. $\frac{I_a}{I_s}$ Versus Time

TABLE XVIII

ADJUSTABLE PARAMETERS USED IN FITTING OF SPECTRAL ENERGY TRANSFER RATE EQUATION MODEL

T (K)	f	$\frac{I_a(0)}{I_s(0)}$	Ω ($s^{-1/2}$)	R_o (nm)
12	0.185	391.4	173	1.72
50	0.056	110.0	272	1.98
100	0.067	227.3	325	2.09
200	0.042	7.3	496	2.18
295	0.060	3.3	1371	2.60

Discussion and Conclusions

Six rare earth ions were doped into $LiNbO_3$:MgO,Cr^{3+} in an attempt to identify a new solid state laser material. The Cr^{3+} absorption band enables flashlamp pumping of the material and the rare earth ions provide the sharp emission transition for laser action. Ions were pumped into the $^4T_2$ level of Cr^{3+} and the emission of the rare earth ion was monitored. There was no emission from the rare earth ion due to energy transfer in $LiNbO_3$:MgO,Cr^{3+} when doped with Tm^{3+}, Nd^{3+}, and Yb^{3+}. The absorption of Er^{3+} was observed in the $^4T_2$ emission of Cr^{3+} but no emission was observed from the transition of the $^4I_{11/2}$ level to the ground state of Er^{3+}.

Energy transfer was observed to occur between Cr^{3+} ions and Yb^{3+} ions in $LiNbO_3$:MgO,Cr^{3+},Yb^3 and the mechanisms for this process have been studied. Five to twenty percent of the energy transfer was radiative and this high percentage was due to the absorption of the Yb^{3+} ion lying spectrally at the peak of the Cr^{3+} emission. The critical interaction distance ranges from 1.1 to 2.6 nm depending upon which analysis technique is used. It is unclear if this material can be used as a new solid state laser material, but the high percentage of energy transfer through radiative mechanisms makes this material's chances as a new flashlamp pumped laser material very slim.

CHAPTER VI

EXCITED STATE ABSORPTION OF PUMP RADIATION AS A LOSS MECHANISM IN SOLID-STATE LASERS

Introduction

Selectively pumping rare earth doped solid state lasers in pump bands only slightly higher in energy than the lasing metastable state is desirable because there is less pump energy converted to heat than there is in broadband pumping throughout the spectral region much higher in energy. The small quantum defect associated with this type of low energy monochromatic pumping can increase the efficiency of laser operation and decrease problems arising from thermal lensing. The development of diode lasers as pump sources has led to the construction of compact, solid state laser systems [62–67]. However the powers and wavelengths presently available from diode laser pump sources are limited. Pumping with the output of an tunable alexandrite laser can be useful in simulating diode laser pumping and extending potential laser pumping to higher power and different wavelength regions. In addition, for some high power laser applications an alexandrite laser may be an ideal pump source for a rare earth doped solid state laser.

The results of an investigation of the spectral dynamics of an $Y_3Al_5O_{12}$:Nd^{3+} (Nd-YAG) laser pumped by the output of an alexandrite laser are presented in this chapter. These results show important differences between broadband frequency pumping and monochromatic pumping, demonstrate the importance of completely characterizing the pumping dynamics of laser systems, and show the effects of excited state absorption (ESA) of pump photons from levels above the lasing transition on the slope efficiency of the laser operation.

Alexandrite Laser Pumping of Nd-YAG

An alexandrite laser with an output tunable between 725 and 805 nm was used to pump a Nd-YAG crystal. The pulse width of the alexandrite laser emission was 60 μs FWHM and the maximum power obtainable was 20 W at a repetition rate of 20 Hz at the peak of the gain curve of the alexandrite laser. The spectral width of the alexandrite laser output was approximately 1 nm FWHM.

The crystal was mounted in a cavity of length of 24 cm consisting of a 100 % reflector with a 50 cm radius of curvature and a flat 85 % output coupler. Transverse pumping was employed with cylindrical and covex lenses used to focus the pump laser beam in the line the length of the Nd-YAG sample. In this way an efficient pumping configuration was achieved. Several spatial modes were present in the Nd-YAG laser output and the radius of the area encompassing these modes was measured to be 0.07 cm. This value was used for the cavity waist in the calculations of the absorbed power by the material and the pump beam was focused within this waist. The small beam waist insured uniform population inversion within the mode volume and that all of the pump energy entering the crystal will pass through the mode. The power incident on the Nd-YAG crystal and the power output from the Nd-YAG laser were measured simultaneously with two calibrated power meters. The Fresnel reflections and absorption of the material were considered when calculating the power absorbed by the crystal. The fluorescence emission from the sample was sent through a 1/4 meter monochromator, detected with an RCA C31034 photomultiplier tube, analyzed by a boxcar integrator, and recorded on a chart recorder. The experimental setup shown in Fig. 33 made it possible to measure the fluorescence emission both while the sample was lasing at 1.06 μm and in the absence of lasing. The sample was 0.28 cm long and contained approximately 10^{20} Nd^{3+} ions / cm^3.

Figure 34 shows the energy levels of Nd^{3+} and the relevant electronic transitions when pumping with 754 and 791 nm. Figure 35 shows the absorption spectrum of Nd^{3+} in YAG in the tuning region of the alexandrite laser. The struc-

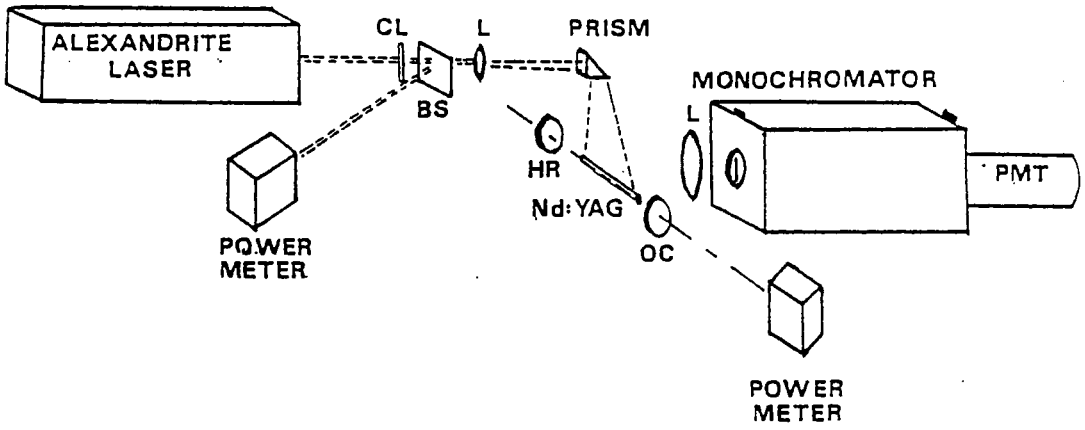

Figure 33. Experimental Set Up Used to Measure Slope Efficiencies and Room Temperature Fluorescence of Nd^{3+} in YAG

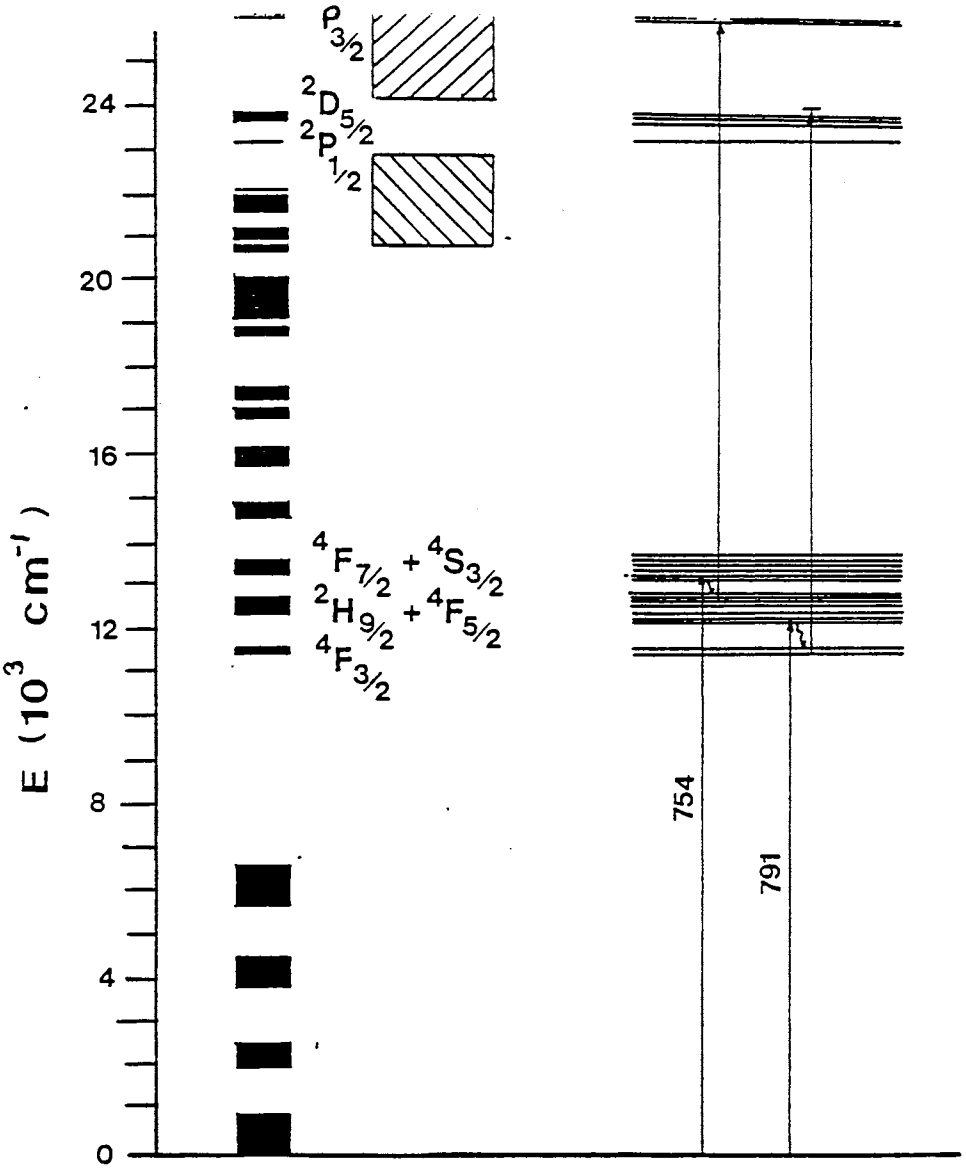

Figure 34. Energy Level Diagram of Nd^{3+} in YAG

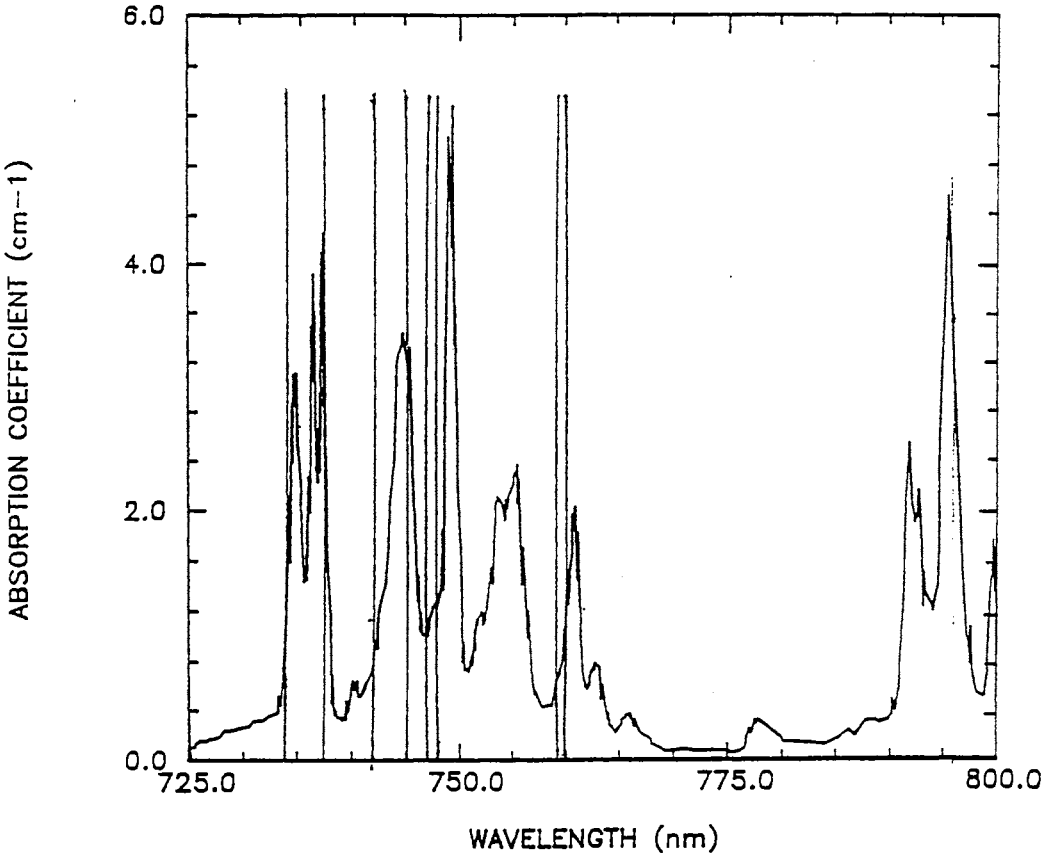

Figure 35. Absorption Spectrum of Nd-YAG in the Spectral Range of Alexandrite Pumping

ture is due to the transitions to various Stark components of the ${}^4S_{3/2} + {}^4F_{7/2}$ levels. The alexandrite laser output is tuned over the absorption transitions shown in Fig. 34 after which radiationless relaxation occurs to the ${}^4F_{3/2}$ metastable state. Fluorescence occurs from the ${}^4F_{3/2}$ level to the levels belonging to the ${}^4I_J$ terms and, above threshold, lasing occurs in the ${}^4F_{3/2} \rightarrow {}^4I_{11/2}$ transition.

Figures 36 and 37 show the room temperature fluorescence spectra between 300 and 900 nm of Nd-YAG pumped by an alexandrite laser at 734.0 and 748.6 nm, respectively. In recording these spectra, a filter was used to eliminate scattered laser light and this also eliminates from the recorded spectra some of the emission transitions occurring between 600 and 770 nm. A neutral density filter rated at 4.0 O.D. was used when recording the fluorescence emission in the spectral region from 770 to 900 nm. Along with the normal fluorescence from the ${}^4F_{3/2}$ level in the near infrared spectral region, strong emission lines appear at higher energies between about 380 and 600 nm. These transitions must be associated with multi-photon absorption processes. The specific transitions that appear in this spectral region and their relative intensities depend on the wavelength and the power of the pump pulse. It appears that these transitions producing the fluorescence of the 380 nm to 600 nm spectral range originate from the ${}^2P_{3/2}$, ${}^2D_{5/2}$, and ${}^2P_{1/2}$ levels and terminate on the various multiplets of the ground term. The spectrum shown in Fig. 37 is also a result of a multi-phonon excitation process and the fluorescence in the green is a result of transitions originating from the ${}^4G_{7/2}$ level and terminating on various components of the ground term.

In order to excite the higher lying fluorescence levels producing the emission shown in Fig. 36, it is necessary for two pump photons to be absorbed. For energy to be conserved, the energy of the transition from the ground state to the final level must match the sum of the energies of the two photons minus any energy lost through radiationless decay processes. There are only two paths for the required two-photon excitation process under these pumping conditions. The first path is for the required two-photon excitation process under these pumping conditions is for the first photon to be absorbed by a transition to one of the Stark

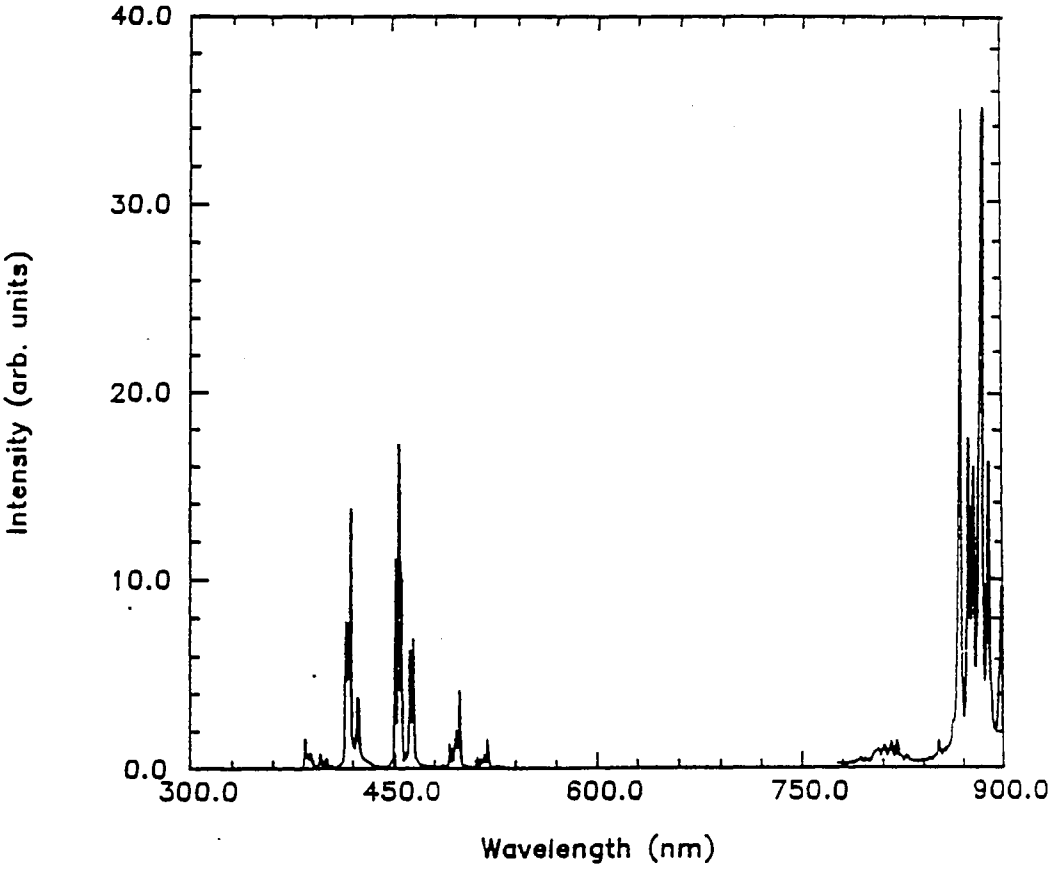

Figure 36. Fluorescence Spectrum of Nd-YAG When Pumped With 734 nm Emission of an Alexandrite Laser

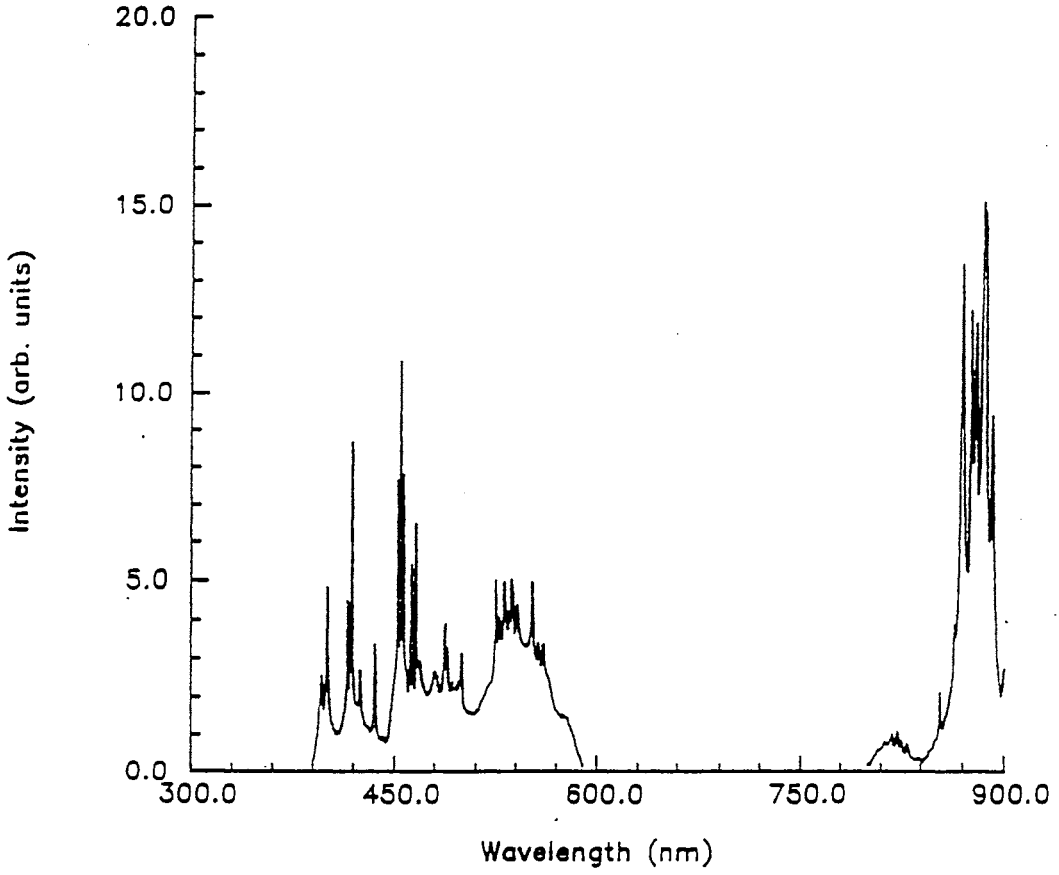

Figure 37. Fluorescence Spectrum of Nd-YAG When Pumped With 748 nm Emission of an Alexandrite Laser

components of the $^4F_{7/2}$+$^4S_{5/2}$ levels followed by radiationless relaxation to the levels of the $^2H_{9/2}$+$^4F_{5/2}$ manifold. The second photon is absorbed before the ion can continue relaxing down to the $^4F_{3/2}$ metastable state. Depending on the exact energy of the pump photons, there is a good energy match to transitions terminating on the two Stark components of the $^2P_{3/2}$ level. In this level there is a branching ratio for fluorescing and radiationless relaxation to the lower $^2D_{5/2}$ and $^2P_{1/2}$ levels from which some fluorescence also occurs.

The second path for two photon excitation has absorption of a pump photon occurring after relaxation to the $^4F_{3/2}$ metastable state. This is not completely unexpected considering the long lifetime of the level. For most host materials the energy difference between the $^4F_{3/2}$ metastable level and upper states of Nd^{3+} will not exactly match the energy of the pump photons; however, this energy mismatch can be compensated for with phonon energy of the lattice.

Excitation spectra of the emission in the 420 nm spectral region was taken in an attempt to verify the above interpretation and the results are shown in Fig. 38. The peaks in the 420 nm excitation spectrum are different from the absorption peaks in Fig. 35 and correspond spectrally to the energy differences between the different Stark components of the $^4F_{5/2}$ +^{2} $H_{9/2}$ manifold and the Stark levels of the $^2P_{3/2}$ multiplet. The excitation spectrum of the 870 nm emission was also measured and found to contain the same features as the absorption spectra shown in Fig. 35.

Theoretical Model Used to Describe Pump Photon ESA

Rate equations were used to model the pumping dynamics occurring when excited state absorption of pump photons takes place. The usual four-level laser system that is used to describe Nd^{3+} lasers[1] is expanded to include two additional levels for the modeling of ESA of pump photons. Figure 39 shows a schematic representation of the levels and the transitions considered. The alexandrite laser pumps ions from the ground state (N_1) to the N_5 manifold. Depletion of this level occurs due to relaxation to the metastable N_3 level. Spontaneous and stimulated

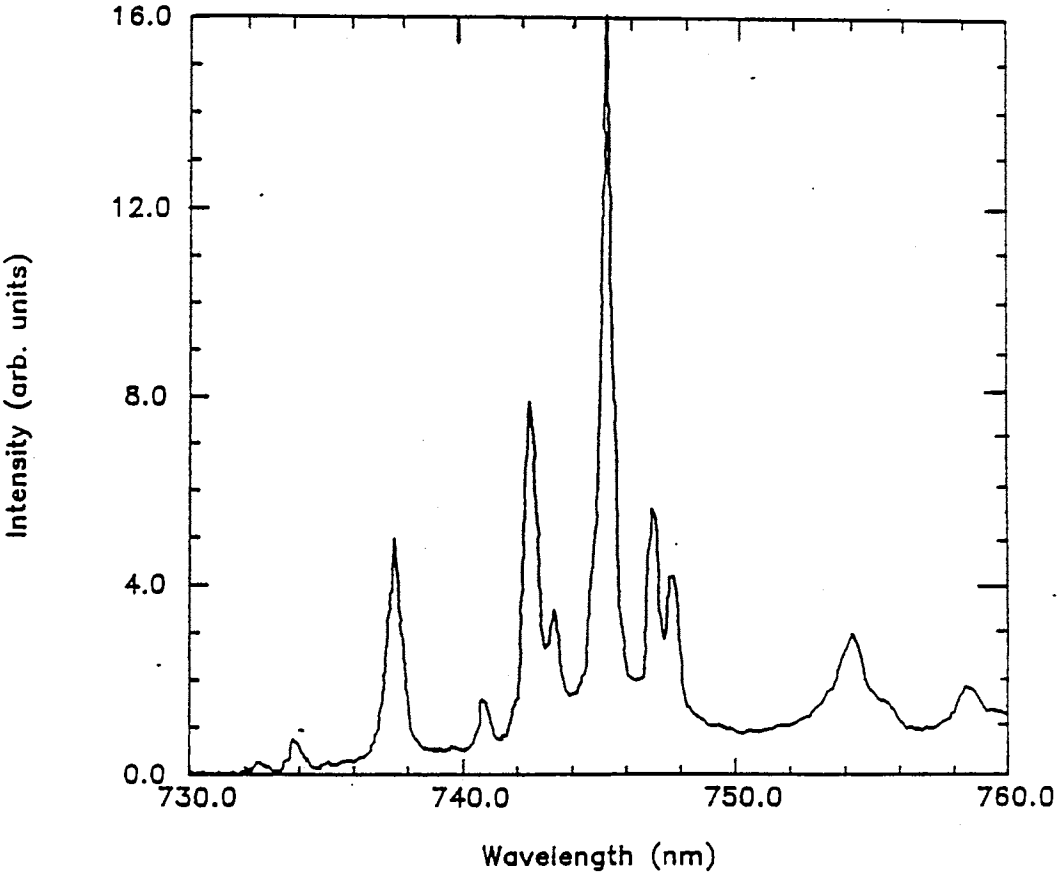

Figure 38. 420 nm Excitation of Nd-YAG When Pumped With the Emission of a Tunable Alexandrite Laser

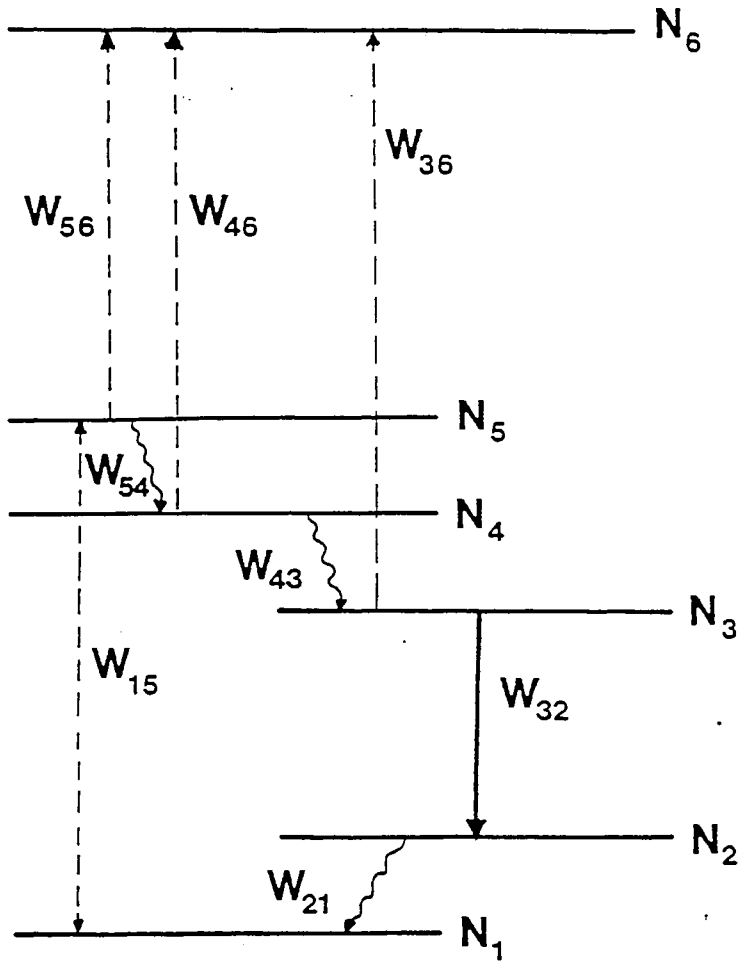

Figure 39. Schematic Used for Rate Equation Model

emission populate the N_2 manifold which then undergoes fast relaxation to the ground state. When there is an energy match between the pump photon and the difference in energy between N_5 and N_6 levels, excited state absorption of the pump photons populates N_6. There is also the situation of pumping into N_5, relaxation into N_4 where ESA of the pump photons occurs, and then further relaxation from N_4 into the metastable state N_3. For non-resonant processes, ESA of the pump photons will occur from the metastable state when there is an energy match between the pump photon and the difference in energy between the metastable state N_3 and an upper excited state N_6.

The rate equations describing the model are

$$\frac{dN_1}{dt} = -W_{15}N_1 + W_{61}N_6 + W_{21}N_2 + W_{51}N_5 \tag{47}$$

$$\frac{dN_2}{dt} = W_{32}N_3 - W_{21}N_2 \tag{48}$$

$$\frac{dN_3}{dt} = W_{43}N_4 - W_{36}N_3 - W_{32}N_3 \tag{49}$$

$$\frac{dN_4}{dt} = W_{54}N_5 - W_{46}N_4 - W_{43}N_4 \tag{50}$$

$$\frac{dN_5}{dt} = W_{15}N_1 - W_{54}N_5 - W_{56}N_5 - W_{51}N_5 \tag{51}$$

$$\frac{dN_6}{dt} = W_{56}N_5 + W_{46}N_4 + W_{36}N_3 - W_{61}N_6 \tag{52}$$

where W_{ij} is the rate of the transition from the i^{th} to the j^{th} level. For fluorescence transitions, W_{ij} is equal to the spontaneous emission rate β_{ij}; and for upward transitions, W_{ij} is equal to $I\sigma_{ij}$, where σ_{ij} is the absorption cross section and I is the peak intensity incident upon the lasing medium.

These equations can be solved for the concentration of ions in the various levels. The pump pulse duration was 60 μs and the nonradiative relaxation to the metastable state was on the order of 1 μs, so steady state conditions were reached in the system in less than 2 % of the pulse duration allowing steady state conditions to be imposed.

The slope efficiency is described by the expression [68]

$$\eta_s = \frac{\lambda_p}{\lambda_o} \cdot (1 - \frac{\sigma_{esa}}{\sigma_e}) \cdot \frac{C_o}{C + L} \cdot \eta_p, \tag{53}$$

where λ_p and λ_o are the pump and output wavelengths, C_o is the output coupler transmission, L is the loss per pass, C is the total transmission of the cavity mirrors, σ_e is the stimulated emission cross section, and σ_{esa} is the excited state absorption due to lasing photons. The pump efficiency is defined as the fraction of total photons absorbed by the ground state that are converted into excited ions in the metastable state (N_3) and contribute to the laser emission. The pumping efficiency is then written as

$$\eta_p = \eta_p^o \cdot (1 - \frac{d\sigma_{36}N_3 + d\sigma_{46}N_4 + d\sigma_{56}N_5}{d\sigma_{15}N_1}), \tag{54}$$

where d is the diameter of the cavity mode. η_p^o is defined as the pumping efficiency of the material without ESA of pump photons occurring and is usually taken to be unity under the assumption that one absorbed photon creates one excited state.

By applying steady state conditions to Eqs. (49), (50), and (51), the ratios $\frac{N_3}{N_1}$, $\frac{N_4}{N_1}$, and $\frac{N_5}{N_1}$ can be written as

$$\frac{N_3}{N_1} = \frac{\beta_{54}\beta_{43}}{(\beta_{32} + I\sigma_{36})(\beta_{43} + I\sigma_{46})} \cdot \frac{\beta_{15}}{(\beta_{15} + \beta_{54} + I\sigma_{56})}, \tag{55}$$

$$\frac{N_4}{N_1} = \frac{\beta_{54}}{(\beta_{43} + I\sigma_{46})} \cdot \frac{\beta_{15}}{(\beta_{15} + \beta_{54} + I\sigma_{56})}, \tag{56}$$

$$\frac{N_5}{N_1} = \frac{\beta_{15}}{(\beta_{15} + \beta_{54} + I\sigma_{56})}. \tag{57}$$

β_{32} can be written to incorporate both spontaneous and stimulated emission as [69]

$$\beta_{32} = \frac{I_L\sigma_e}{1 + \tau_f\sigma_e I_L}, \tag{58}$$

where τ_f is the fluorescent lifetime of the metastable state and I_L is the intensity of the lasing emission within the cavity. At threshold, $\tau_f\sigma_e I_L \ll 1$, so $\beta_{32} = I_L\sigma_e$, and well above threshold, $\tau_f\sigma_e I_L \gg 1$, so $\beta_{32} = 1/\tau_f$. Since we were considering the case of pumping above threshold, Eq. (58) was estimated with the radiative rate from the metastable level.

The slope efficiency can be rewritten by substituting Eqs. (54), (55), (56), and (57) into Eq. (53) as

$$\eta_s = \eta_s^o \cdot (1 - \frac{A}{I^2\sigma_{15}(\frac{\sigma_{36}}{\beta_{32}})(\frac{\sigma_{46}}{\beta_{43}}) + \sigma_{15} + I\sigma_{15}(\frac{\sigma_{46}}{\beta_{43}}) + I\sigma_{15}(\frac{\sigma_{36}}{\beta_{32}}) + \frac{\beta_{54}}{I} + A}) \tag{59}$$

where

$$\begin{aligned} A &= I^2\sigma_{56}(\frac{\sigma_{36}}{\beta_{32}})(\frac{\sigma_{46}}{\beta_{43}}) + I\sigma_{56}(\frac{\sigma_{36}}{\beta_{32}}) + I\beta_{54}(\frac{\sigma_{36}}{\beta_{32}})(\frac{\sigma_{46}}{\beta_{43}}) + \\ &\quad \beta_{54}(\frac{\sigma_{36}}{\beta_{32}}) + I\sigma_{56}(\frac{\sigma_{46}}{\beta_{43}}) + \beta_{54}(\frac{\sigma_{46}}{\beta_{43}}) + \sigma_{56}, \end{aligned} \tag{60}$$

and

$$\eta_s^o = \frac{\lambda_p}{\lambda_o} \cdot (1 - \frac{\sigma_{esa}}{\sigma_e}) \cdot \frac{C_o}{C + L} \cdot \eta_p^o. \tag{61}$$

η_s^o and η_p^o were assumed to have a constant value for the different pump wavelengths. All of the values in Eq. (61) are pump wavelength independent except for λ_p, but the change in the ratio $\frac{\lambda_p}{\lambda_o}$ is not significant when considering the range of 737 to 791 nm.

There are five simplifications of Eq. (59) to be considered.

Case (1) : If there is no ESA of pump photons, $\sigma_{36} = \sigma_{46} = \sigma_{56} = 0$,

$$\eta_s = \eta_s^o. \tag{62}$$

Case (2) : For the situation where $\sigma_{36} = \sigma_{46} = 0$ and $\sigma_{56} \neq 0$,

$$\eta_s = \eta_s^o \cdot (1 - \frac{1}{1 + \frac{\beta_{54}}{I\sigma_{56}} + \frac{\sigma_{15}}{\sigma_{56}}}). \tag{63}$$

Case (3) : For the situation where $\sigma_{36} = \sigma_{56} = 0$ and $\sigma_{46} \neq 0$,

$$\eta_s = \eta_s^o \cdot (1 - \frac{1}{1 + \frac{\beta_{43}}{I\sigma_{46}} + \frac{I\sigma_{15}}{\beta_{54}} + (\frac{\beta_{43}}{\beta_{54}})(\frac{\sigma_{15}}{\sigma_{46}})}). \tag{64}$$

Case (4) : For the situation where $\sigma_{46} = \sigma_{56} = 0$ and $\sigma_{36} \neq 0$,

$$\eta_s = \eta_s^o \cdot (1 - \frac{1}{1 + \frac{\beta_{32}}{I\sigma_{36}} + \frac{I\sigma_{15}}{\beta_{54}} + (\frac{\beta_{32}}{\beta_{54}})(\frac{\sigma_{15}}{\sigma_{36}})}). \tag{65}$$

Case (5) : For the situation where $\sigma_{36} = 0$ and $\sigma_{46} \neq \sigma_{56} \neq 0$,

$$\eta_s = \eta_s^o \cdot (1 - \frac{1 + (\frac{I\sigma_{56}}{\beta_{54}}) + (\frac{\beta_{43}}{\beta_{54}})(\frac{\sigma_{56}}{\sigma_{46}})}{(\frac{\beta_{43}}{\beta_{54}})(\frac{\sigma_{15}}{\sigma_{46}}) + (\frac{I\sigma_{15}}{\beta_{54}}) + (\frac{\beta_{43}}{I\sigma_{46}}) + 1 + (\frac{\beta_{43}}{\beta_{54}})(\frac{\sigma_{56}}{\sigma_{46}}) + (\frac{I\sigma_{56}}{\beta_{54}})}). \quad (66)$$

The effectiveness of loss in the system credited to ESA of pump photons depends on the relative rate of the nonradiative relaxation of the ions in the initial state of the transition compared to the rate of excited state absorption. The exponential energy gap law [70] predicts a multiphonon decay rate for the $^4F_{5/2}$ term on the order of 10^6 s^{-1}, whereas the ESA pump rate at threshold

$$W_{ESA} = \sigma_{ESA}(\frac{I}{\hbar\omega}) \quad (67)$$

is on the order of 10^7 s^{-1}. σ_{15} was determined from the absorption spectra and the values for multi-phonon decay rates are given in Table XIX.

The lasing characteristics were measured for three alexandrite pump wavelengths and the slope efficiencies determined. The experimental points are displayed in Fig. 40. The pump wavelengths chosen were characteristic of cases (1), (2), and (4) described previously.

The highest slope efficiency measured was 53 % at a pump wavelength of 787 nm and we assume this corresponds to case (1) of no ESA of pump photons. The energy level diagram (Fig. 34) reveals this wavelength falls outside the overlap region where ESA of pump photons can occur. The box with forward slashes in Fig. 34 is at energies where ESA of pump photons processes can occur and the box with back slashes is at energies where ESA of lasing photon processes can occur. For 754 nm excitation there was a decrease in the slope efficiency and from the energy level diagram it was determined that the resonant ESA process was the dominant process taking place at this pump wavelength. Equation (64) was applied for ESA resonant from a level above the metastable state and an excited state absorption cross section was determined by fitting Eq. (64) to the slope efficiency curve shown in Fig. 40. For 791 nm excitation it was determined that vibronic ESA of the pump photon was the dominant process and an excited state absorption cross section was determined by fitting Eq. (65) to the slope efficiency

TABLE XIV

SAMPLE PARAMETERS FOR Nd:YAG

N (cm^{-3})	1.0×10^{20}	
σ_{32} (cm^2)	7.8×10^{-19}	
λ_o (nm)	1064	
β_{54} (sec^{-1})	2×10^7	
β_{43} (sec^{-1})	7×10^6	
n	1.5	
η_s^o	53 %	
	λ_p=754 nm	
σ_{15} (cm^2)		1.2×10^{-20}
σ_{46} (cm^2)		$3 \pm 1 \times 10^{-18}$
η_s		28 %
	λ_p=791 nm	
σ_{15} (cm^2)		4.4×10^{-21}
σ_{36} (cm^2)		$8 \pm 3 \times 10^{-22}$
η_s		35 %

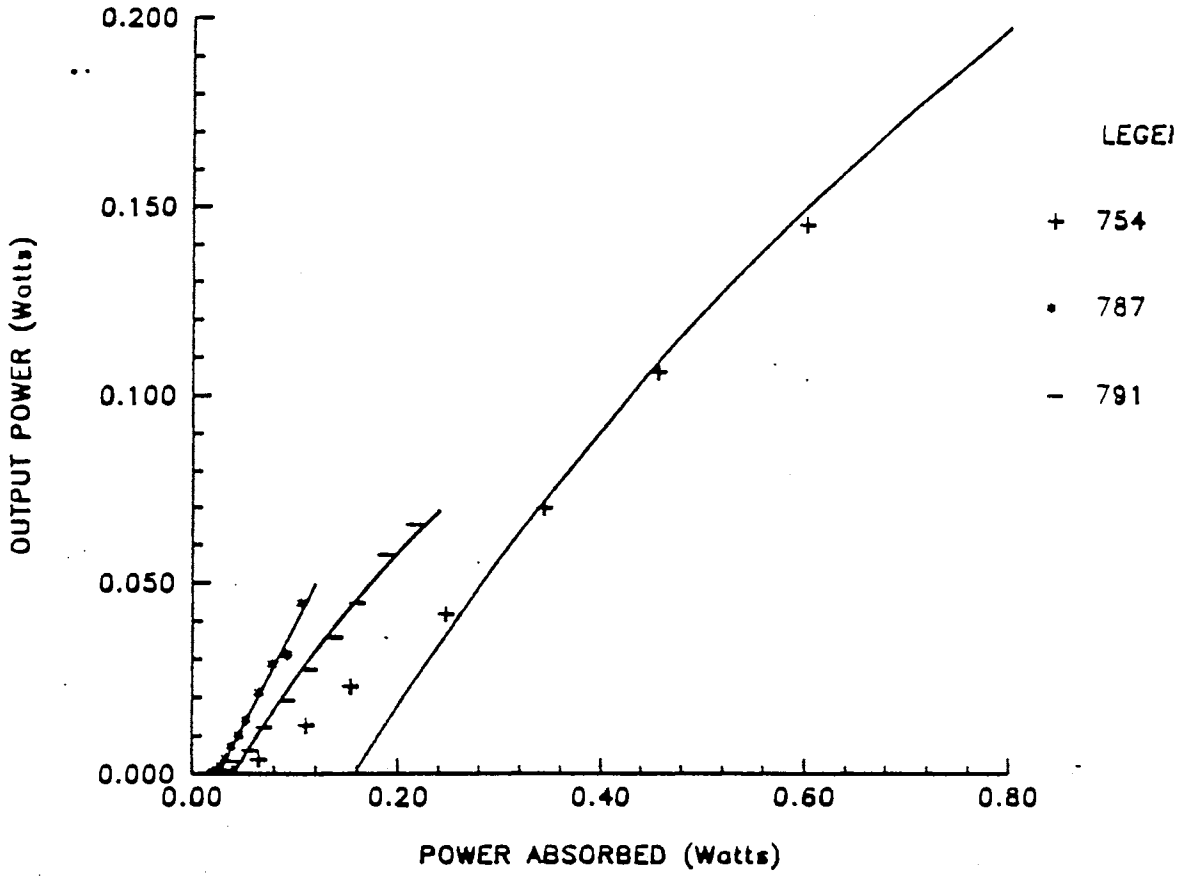

Figure 40. Power Threshold and Slope Efficiency for Nd-YAG Pumped by an Alexandrite Laser (the solid line is the fit to the slope efficiency curve for 754 and 791 nm pumping)

curve shown in Fig. 40. The ESA cross sections obtained from the fitting procedure and the values for the parameters used in the calculations are given in Table XIX. As expected the excited state absorption cross section for the vibronic process is smaller than that due to the resonant process.

The pumping efficiency discussed in the preceding section is not the same as the conversion efficiency. The pumping efficiency is defined as the ratio of power out to power absorbed by the ground state of the lasing medium, and the conversion efficiency is defined as the ratio of power out to the total power absorbed by the medium. In slope efficiency plots, the power output from the lasing medium is plotted versus the power absorbed by the crystal. When there is no ESA of pump photons, the power absorbed by the lasing medium is equal to the power absorbed by the ground state and the pumping efficiency is equal to the conversion efficiency. When ESA of pump photons is present, the power absorbed by the medium is greater than the power absorbed by the ground state and this absorbed power cannot be determined from the absorption coefficient of the medium at the specific pump wavelength. It is possible, however, to find a relationship between the pumping efficiency η_p and the conversion efficiency η_c. By considering a simple system, one can write the total number of ions that contribute to the laser emission as

$$N_L = N_g - N_{ESA}, \tag{68}$$

where N_g is the number of ions in the ground state that absorb a photon and move to an excited state, and N_{ESA} are the number of ions in the excited state that are lost to ESA of pump photon processes. Assuming that one photon absorbed will create one excited state, the pumping efficiency can be written as

$$\eta_p = \frac{N_L}{N_g} = 1 - \frac{N_{ESA}}{N_g}, \tag{69}$$

and this equation is in agreement with Eq. (54) used earlier. The total number of photons absorbed by the material is

$$N_{tot} = N_g + N_{ESA}. \tag{70}$$

Combining Eqs. (68) and (70) the conversion efficiency can be written as

$$\eta_c = \frac{N_L}{N_{tot}} = 1 - \frac{2N_{ESA}}{N_{tot}}. \tag{71}$$

The equation relating the two efficiencies is

$$\eta_c = \frac{\eta_p}{2 - \eta_p}. \tag{72}$$

The conversion efficiency is never greater than the pumping efficiency and the conversion efficiency is useful when determining the wallplug efficiency of the laser.

Discussion and Conclusions

The results discussed above show that alexandrite laser pumped Nd-YAG lasers can have a pump wavelength dependent loss mechanism associated with the excited state absorption of pump photons. This loss mechanism occurs with flashlamp pumping, but its consequences are magnified when pumping laser materials with monochromatic light. ESA of pump photons will occur for transitions resonant from upper levels and vibronic transitions from the metastable state. It will limit the slope efficiencies obtainable and may even quench the laser emission of rare earth doped laser materials and complete characterization of the pumping dynamics must be determined in order to limit this loss mechanism. It is also possible to obtain an estimate for the excited state absorption cross section from the rate equation model.

Different processes which affect the slope efficiency such as thermal lensing and ground state saturation were not accounted for in this rate equation model. ESA of the pump photons will cause the crystal to store heat and this may be one reason for the large heat load reported when flashlamp pumping Nd-YAG. Heat storage in the laser material will also cause a greater amount of thermal lensing in some materials and the thermal lensing will decrease the value of the slope efficiency further. The resulting excited state absorption cross section determined from the above method must be considered as an upper limit since it is assumed that only ESA of pump photons is causing the change and it might be a combination of ESA of pump photons and other processes.

An approximation that is made in this method is the calculation of the nonradiative relaxation rate from the Energy Gap law. The Energy Gap law fails as small energy gaps are approached because the approximation that the nonradiative relaxation rate follows an exponential is no longer a valid assumption. The calculation of the excited state absorption cross section is very dependent upon the nonrelaxation rate and any inaccuracies are carried through to the value of σ_{ESA}. It is difficult to use this technique to determine the excited state absorption cross section in disordered materials or in materials where the nonradiative relaxation rate is not known.

Figure 41 shows the energy levels of Nd^{3+} in various hosts. The resonances needed for ESA of pump photons to occur is very host dependent because of the shifts in energy levels and strengths of the transitions to the $^2D_{1/2}$, $^2P_{3/2}$, and $^2P_{1/2}$ levels. Thus by carefully choosing the host material, ESA of the pump photons can be maximized or minimized. If ESA of pump photons is maximized in solid state laser materials, it might be possible to lase the transition from the highest excited state to the ground state, thus producing a green or possibly a blue solid state laser using this type of pumping scheme. For example, the disordered hosts such as BMAG appear to have strong ESA of pump photons due to their broadened energy levels resulting in a greater probability of energy match with pump photons [71]. On the other hand, crystals such as Nd:YVO_4 appear to have a weak transition probability to the level needed for ESA of pump photons to occur when pumping into the $^4F_{7/2} +^4 S_{3/2}$ and $^2H_{9/2} +^4 F_{5/2}$ manifolds.[72]

This theory for ESA of pump photons presented is not limited to Nd^{3+}. Fluorescence observed in Er^{3+} and Ho^{3+} -doped laser materials when pumping with the emission of an alexandrite laser can be explained with this mechanism. The strength of this process will be determined by the resonance of the energy of the pump photons with the energy difference of energy levels of the impurity ion.

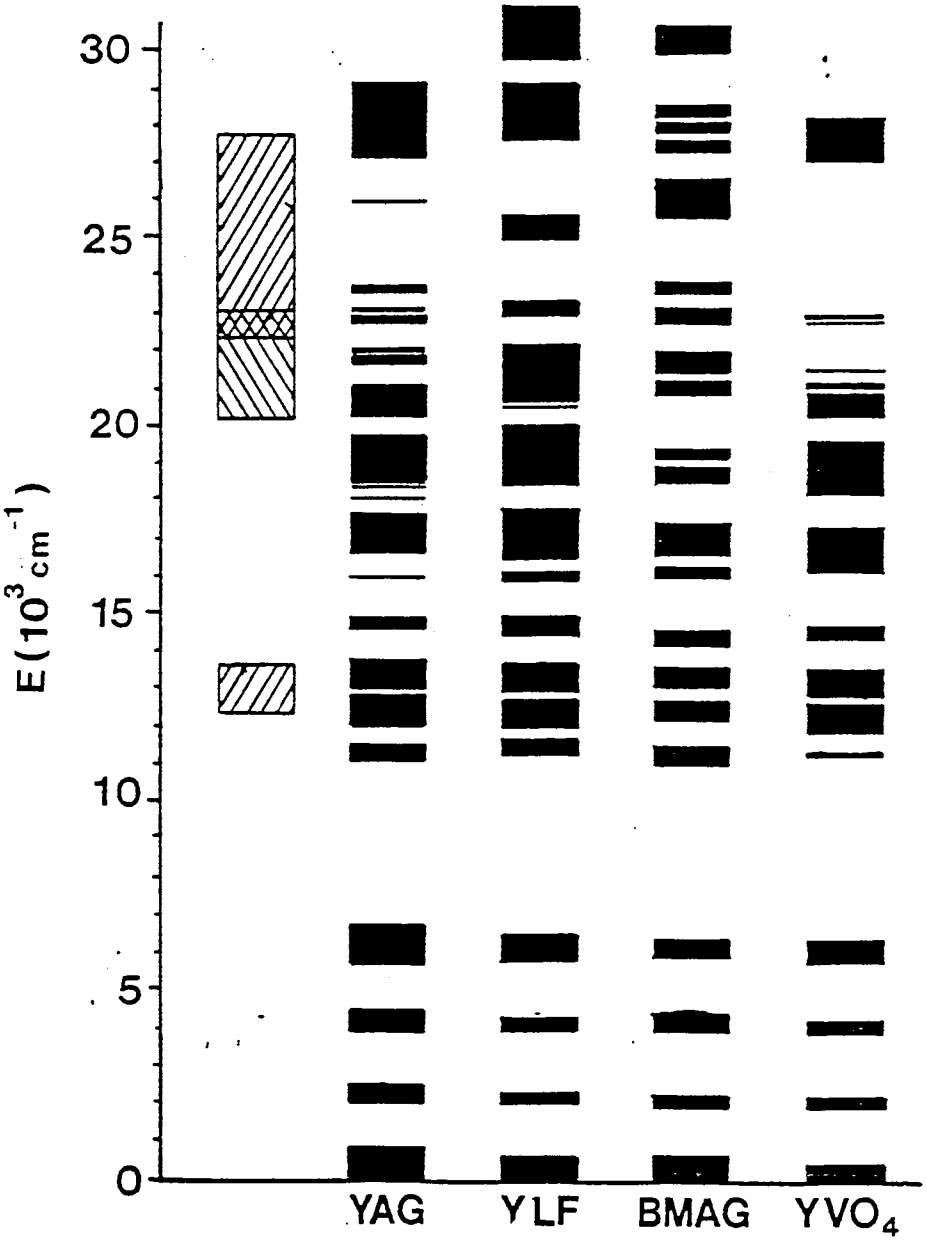

Figure 41. Energy Levels of Nd^{3+} in $Y_3Al_5O_{12}$ (YAG), $LiYF_4$ (YLF), $Ba_2MgGe_2O_7$ (BMAG), and YVO_4

CHAPTER VII

SUMMARY AND CONCLUSIONS

Summary

The characterization of different processes that occur in solid state laser materials has been discussed in the previous chapters. The use of laser spectroscopy and laser pumping has provided a better understanding of energy migration, multiphonon and multiphoton processes, and excited state absorption of both pump and lasing photons in these materials. All of these processes are important when investigating the dynamics of solid state laser crystals.

In Chapter II a comparison was made of the use of three techniques for determining the effects of stimulated emission on the spectra of solid-state vibronic laser materials: peak single-pass gain, fluorescence band narrowing, and lifetime shortening. Each of these was used to obtain the pump energy density and the population inversion at threshold, the stimulated emission cross section, and the gain coefficient for two potential vibronic laser materials. The difficulty and accuracy of each technique is discussed. Lifetime shortening is the easiest experimental measurement to make. The results were analyzed by using numerical techniques to solve the coupled set of rate equations describing the concentration of photons and population of excited states of ions in an optically pumped material under δ-function pulsed excitation. The solutions predict an effective shortening of the fluorescence lifetime at high excitation levels with a distinct threshold where stimulated emission processes become important. The observed band narrowing for the same type of pumping conditions is shown to be consistent with the theoretical predictions of the model developed by McCumber.

In Chapter III a comparison of two potential solid state laser materials were made to Ti:Sapphire. The spectral properties of Ti:Chrysoberyl and Ti:BA were measured and compared to the spectral properties of Ti:Sapphire and found to be very similar. The results of the spectra and laser pumping measurements was that Sapphire is still the material of choice for Ti^{3+} ions.

In Chapter IV $LiNbO_3$ is examined as a laser host for different transition metal ions. Cr^{3+} was more promising as a dopant ion than either Ni^{2+} or Co^{2+} for room temperature laser operation, but attempts to observe laser emission from $LiNbO_3$:MgO,Cr^{3+} failed due to thermal buildup in the material.

In Chapter V energy transfer from Cr^{3+} doped in $LiNbO_3$ to a rare earth ion was investigated. The rare earth ions investigated were Tm^{3+}, Ho^{3+}, Nd^{3+}, Er^{3+}, and Yb^{3+}. The first four materials investigated produced negative results due to either low concentration of the rare earth ion or a small overlap between the absorption band of the rare earth ion and the emission band of Cr^{3+}. Energy transfer was observed in $LiNbO_3$:MgO,Cr^{3+},Yb^{3+} but no lasing of the Yb^{3+} was seen.

In Chapter VI the characteristics of the optical pumping dynamics occurring in laser-pumped rare earth-doped, solid-state laser materials were investigated by using the emission of a tunable alexandrite laser to pump $Y_3Al_5O_{12}$:Nd^{3+} in an optical cavity. It was found that the slope efficiency of the Nd laser operation depends strongly on the wavelength of the pump laser. A model was developed to explain the observed variation in the slope efficiencies with pump wavelength. Excited state absorption of pump photons was found to be an important loss mechanism involving two types of transitions: resonant transitions originating on levels above the metastable state producing a blue-green emission and non-resonant vibronic transitions originating on the metastable state producing a green emission. The theoretical fits of the experimental data provide information on the excited state absorption cross sections and the rates of these transitions.

Future Work

There is much more work that needs to be done to fully understand the dynamics of solid state laser crystals and to identify new solid state laser materials. $LiNbO_3$ should not be disregarded as a laser host. The crystal field of this material shifts the emission band of Cr^{3+} to a very desirable spectral region for laser operation and the absorption band of Cr^{3+} provides an efficient means of pumping the material. $LiNbO_3$ has recently been shown to cause different shifts in the absorption and emission bands of Cr^{3+} when the Cr^{3+} ions occupy different sites in the material. Further investigation of the possible lasing of this material with Cr^{3+} occupying the different sites is needed to better understand the dynamics of this material. Further investigation of energy transfer from the broad emission band of $LiNbO_3$:Mgo,Cr^{3+} to rare earth ions should also be pursued in an attempt to observe laser emission from the rare earth ions. The preliminary results from this investigation were very promising and lasing of the rare earth ion can be expected using the flashlamp pumping the broad absorption band of Cr^{3+}.

By far the most exciting work and research that needs to be pursued lies in the area of excited state absorption of pump photons when monochromatically pumping laser materials. This is the first time ESA of pump photons has been reported to affect the value of the slope efficiency and ESA of pump photons becomes very important when trying to optimize laser pumped laser systems. This will also make a great impact on the use of diode lasers to pump laser systems. It is important to better understand both the processes involved and determine the effect of resonance versus nonresonance energy level gaps with the energy of the pump photons and this can be done with low temperature studies. Low temperature studies would eliminate thermal population of upper states in the manifolds and would eliminate thermal broadening of the levels. The work described in this thesis examines ESA of pump photons in Nd:YAG and should be expanded to include other host materials for neodymium. The work should also be expanded

to include other rare earth ions because preliminary results show ESA of pump photons to occur in Er^{3+} and Ho^{3+} doped materials.

BIBLIOGRAPHY

1. A.E.Seigman, *Lasers*, University Science, Palo Alto, 1986.

2. R.C.Powell, J.L.Caslavsky, Alshaieb, and J.M.Bowen, J.Appl.Phys. **58**, 2331 (1985).

3. G.M.Loiacono et al., Appl.Phys.Lett. **48**, 622 (1986).

4. D.E.McCumber, Phys. Rev. **134**, A299 (1964).

5. J.C.Walling, O.G.Peterson, H.P.Jenssen, R.C.Morris, and E.W.O'Dell, IEEE J.Quantum. Electron. **QE-16**, 1302 (1980).

6. L.F.Johnson, H.J.Guggenheim, and R.A.Thomas, Phys.Rev **149**, 179 (1966).

7. R.C.Powell, R.H.Schweitzer, J.J.Martin, G.E.Venikouas, and C.A.Hunt, J.Chem.Phys. **81**, 1178 (1984).

8. L.W.Casperson, J.Appl.Phys. **48**, 256 (1977).

9. K.Thyagarajan and A.K.Ghatak, *Lasers: Theory and Applications*, Plenum, New York, 1981.

10. G.J.Quarles and R.C.Powell, none, unpublished.

11. K.L.Schepler, Spectroscopy and laser performance of ti^{3+} and cr^{3+},nd^{3+} co-doped crystals, Technical report, Air Force Wright Aeronautical Laboratories, Wright Patterson Air Force Base, Ohio, 1988.

12. P.F.Moulton, Optics News **Nov./Dec.**, 9 (1982).

13. P.F.Moulton, J.Opt.Soc.Am.B. **33**, 123 (1986).

14. L.G.DeShazer, G.F.Albrecht, and J.F.Seamans, SPIE High Power and Solid State Lasers **622**, 133 (1986).

15. A.Sanchez, R.E.Fahey, A.J.Strauss, and R.L.Aggarwal, Opt.Let. **11**, 363 (1986).

16. P.Albers, E.Stark, and G.Huber, J.Opt.Soc.Am.B. **3**, 134 (1986).

17. P.Lacovara, L.Esterowitz, and M.Kokta, IEEE J. of Quantum Electronics **QE-21**, 1614 (1985).

18. G.F.Albrecht, J.M.Eggleston, and J.J.Ewing, Optics Com. **52**, 401 (1985).

19. R.C.Powell, G.E.Venikouas, L. Xi, and J.K.Tyminski, J.Chem.Phys. **84**, 622 (1986).

20. C.E.Byvik and A.M.Buonchristaini, IEEE J.Quant.Electron. **QE-21**, 121 (1985).

21. B.K.Sevast'Yanov et al., Sov.Phys.Dokl **30**, 508 (1985).

22. R.R.Joycw and P.L.Richards, Phys.Rev **179**, 376 (1969).

23. R.Rai, phys.stat.sol(b) **52**, 671 (1972).

24. B.F.Gachter and J.A.Koningstein, J.Chem.Phys. **60**, 2003 (1974).

25. E.D.Nelson, J.Y.Wong, and A.L.Schawlow, *Optical Properties of Ions in Crystals*, Wiley Interscience, New York, 1967.

26. B.DiBartolo, editor, *Optical Interactions in Solids*, John Wiley and Sons, Inc., New York, 1986.

27. A.von.Hippel, Z.Physik **101**, 689 (1936).

28. F.Seitz, Trans.Faraday Soc. **35**, 79 (1939).

29. F.E.Williams and M.H.Hebb, Phys.Rev. **84**, 1181 (1951).

30. M.Lax, Phys.Rev. **86**, 660 (1951).

31. C.C.Klick and J.H.Shulman, J.Opt.Soc.Am. **42**, 910 (1952).

32. M.L.Kliewer, A.Suchocki, and R.C.Powell, Appl.Opt. **27**, 5016 (1988).

33. Y.Segawa et al., Jap.J.Appl.Phys. **26**, L (1987).

34. B.Perner, J. Kvapil, and J. Kvapil, Czech.J.Phys.B **38**, 181 (1988).

35. L.E.Bausa, F.Jaque, J. Sole, and A.Duran, Photoluminescence of ti^{3+} in p_2o_5 - na_2o - al_2o_3 glass, to be published.

36. W.Strek, P.J.Deren, and B.Jezowska-Trzebiatowska, Optical properties of ti^{3+} in $mgal_2o_3$ spinel, to be published.

37. L.E.Bausa, F.Jaque, J. Sole, R.Cases, and A.Duran, Photoluminescence of ti^{3+} in phospate glasses, to be published.

38. A.A.Kaminskii, phys.stat.sol(a) **1**, 573 (1970).

39. I.P.Kaminow and L.W.Shultz, IEEE J.Quantum.Electron. **QE-11**, 306 (1975).

40. A.A.Kaminskii, Sov.Phys.-Crystallog. , 17.

41. K.G.Belabeav, A.A.Kaminskii, and S.E.Sarkisov, phys.stat.sol(a) **28**, K17 (1975).

42. L.I.Ivleva, A.A.Kaminskii, Yu.S.Kuzminov, and V.N.Shpkov, Sov.Phys.-Dok. **13**, 1185 (1969).

43. G.Zhong, J.Jian, and Z.Wu, Measurements of optically induced refractive index damage of lithium niobate doped with different concentrations of mgo, in *Proceedings of the 11th International Quantum Electronics Conference, IEEE catalog No 80CH 1561-O*, page 631, New York, 1980, Institute of Electrical and Electronic Engineers.

44. E.F.Weller, editor, *Ferroelectricity*, page 259, El Sevier Publ.Co., Amsterdam, 1967.

45. P.F.Moulton and A.Mooradian, Appl.Phys.Lett. **35**, 838 (1979).

46. P.F.Moulton, IEEE J.Quant.Electron. **QE-18**, 1185 (1982).

47. L.F.Johnson, R.E.Dietz, and H.J.Guggenheim, Appl.Phys.Lett. **5**, 21 (1964).

48. S.Sugano, Y.Tunabe, and H.Kamimura, *Multiplets of Transition Metal Ions in Crystals*, Academic Press, New York, 1970.

49. L.F.Johnson, R.E.Dietz, and H.J.Guggenheim, Phys.Rev.Lett. **11**, 318 (1963).

50. S.C.Abrahams, J.M.Reddy, and J.L.Bernstein, J.Phys.Chem.Solids **27**, 997 (1966).

51. S.C.Abrahams and J.L.Bernstein, J.Phys.Chem.Solids **28**, 1685 (1967).

52. A.M.Glass, J.Chem.Phys. **50**, 1501 (1969).

53. T. Allick, private communications.

54. L.F.Johnson and A.A.Ballman, J.Appl.Phys. **40**, 297 (1969).

55. J.A.Caird, L.G.DeShazer, and J.Nella, IEEE J.Quantum.Electron. **11**, 874 (1975).

56. T.Y.Fan, A.Cordova-Plaza, M.J.Digonnet, R.L.Byer, and H.J.Shaw, J.Opt.Soc.Am.B. **3**, 140 (1986).

57. A.Cordova-Plaza, M.J.F.Diggonnet, and H.J.Shaw, IEEE J.Quant.Electron. **QE-23**, 262 (1987).

58. A.A.Kaminskii, Soviet Physics-Crystallography **17** (1972).

59. V.T.Gabrielyan, A.A.Kaminskii, and L.Li, phys.stat.sol.(a) **3**, K37 (1970).

60. D.L.Dexter, J.Chem.Phys. **22**, 836 (1953).

61. T.Forster, Ann.Phys. **2**, 55 (1948).

62. B.Zhou, T.J.Kane, G.J.Dixon, and R.L.Byer, Opt.Lett. **10**, 62 (1985).

63. F.Hanson and D.Haddock, Appl.Opt. **27**, 80 (1988).

64. R.L.Byer, Science **239**, 742 (1988).

65. T.Y.Fan and R.L.Byer, IEEE J.Quantum.Electron. **QE-24**, 895 (1988).

66. G.T.Maker, S.J.Keen, and A.I.Ferguson, Appl.Phys.Lett. **53**, 1675 (1988).

67. J.Berger, D.F.Welch, and D.R.Scifres, Appl.Phys.Lett. **51**, 212 (1987).

68. J.A.Caird et al., IEEE J.Quantum.Electron. **QE-24**, 1070 (1988).

69. A.Yariv, *Quantum Electronics*, Wiley, New York, 1989.

70. L.A.Riseberg and M.J.Weber, Progr.Opt. **14**, 89 (1977).

71. M.J.Ferry, R.J.Reeves, M.L.Kliewer, T.Allick, and R.C.Powell, to be published.

72. M.L.Kliewer, L.G.DeShazer, and R.C.Powell, to be published.

73. T.H.Maiman, Nature **187**, 493 (1960).

74. T.H.Maiman, R.H.Hoskins, I.J.D'Haenens, C.K.Asawa, and V.Evtuhuv, Phys. Rev. **123**, 1151 (1961).

75. M.L.Shand, J.C.Walling, and H.P.Jenssen, IEEE J. Quantum Electron. **QE-18**, 167 (1982).

76. J.C.Walling et al., IEEE J. Quantum Electron. **QE-21**, 167 (1982).

77. D.E.McCumber, Phys. Rev. **136**, A954 (1964).

78. B.S.Neporent, Sov.Phys. **3**, 337 (1958).

79. Y.B.Band and D.F.Heller, On the relationship between the absorption and emission for the modulation spectra of polyatomic molecules, to be published.

80. A.Einstein, Physik Z. **18**, 121 (1917).

81. D.H.Menzel, editor, *Fundamental Formulas in Physics*, Dover Publications, New York, 1960.

APPENDIX

A DISCUSSION OF McCUMBER'S THEORY OF PHONON-TERMINATED LASERS

A DISCUSSION OF McCUMBER'S THEORY OF PHONON-TERMINATED LASERS

Introduction

Ever since the invention of the ruby laser in 1960 [73,74], the technology of lasers has been rapidly advancing and models used to describe their operation have been examined. At present two simplified models can be used to describe solid state lasers. They are the multi-level model and the lattice relaxation model shown in Fig. 42. The multi-level model is used for systems involving more than two energy levels where the energy levels are themselves discrete electronic states. Three- and four-level laser systems involving a purely electronic lasing transition fall into this category. The multi-level model can be used to describe the case when population of an upper state occurs followed by depopulation of that state (usually by nonradiative decay) to a metastable level, and then followed by a subsequent radiative transition to the ground state or to a terminal level above the ground state.

The lattice relaxation model describes vibronic lasers where the lower laser level is actually a band of energy levels. This band is a single electronic energy level that has a continuum of sublevels arising from vibrations of the crystalline lattice. An isolated, excited impurity ion can decay from the upper electronic state to its electronic ground state by means of a vibronic transition which results in the emission of one or more phonons as well as the emission of a photon. The differences between vibronic and non-vibronic transitions are shown in Fig. 43. In this figure the potential energy of the crystal field manifold is plotted versus a vibrational distorting coordinate. Both diagrams show an absorption transition

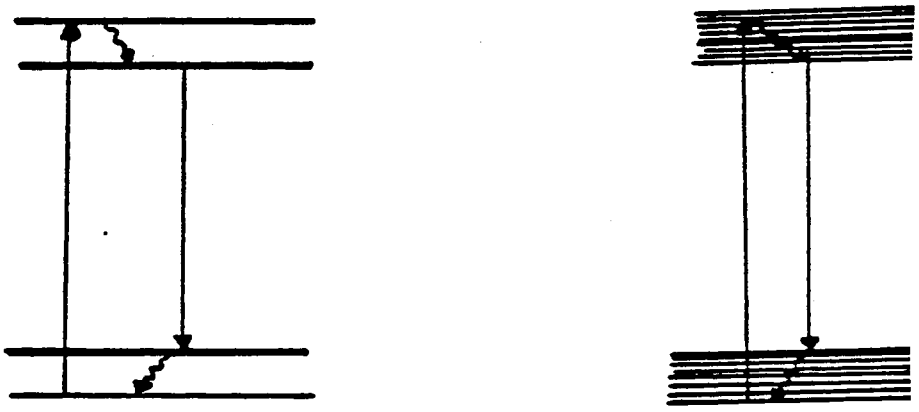

Figure 42. Multi-Level and Lattice Relaxation Model Used for Describing Laser Action in Laser Materials

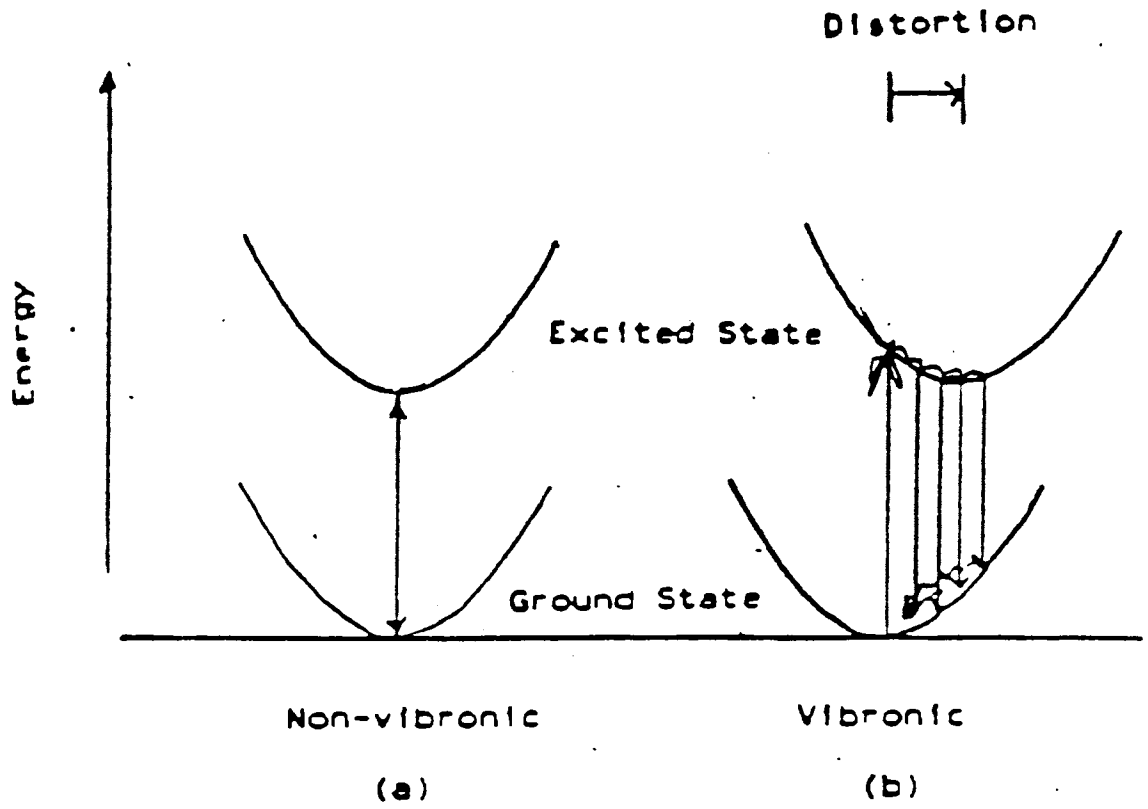

Figure 43. Single Configurational Coordinate Diagrams Depicting (a) Nonvibronic and (b) Vibronic Transitions

from a ground state minimum to an excited state followed by a decay to the ground state. In Fig. 43(a), the transition between the excited state minimum to the ground state minimum is purely electronic, resulting in the emission of only a photon. The optical spectra from this transition will show a sharp "zero-phonon" line. In Fig. 43(b), the transition is an electronic transition from the relaxed excited state to a vibrationally excited component of the ground state and finally the emission of a phonon to the ground state minimum. The optical spectra of this material will show a broadband absorption and emission depicting the phonon assisted transitions and zero-phonon lines depicting the electronic transitions (see Fig 44.).

This appendix is a discussion of McCumber's theory (1964) for vibronic lasers [4] with its application to the $MgF_2 : Ni^{2+}(1\%)$ laser and the phonon-terminated laser emission from alexandrite [5,75,76].

McCumber's Theory of Phonon-Terminated Lasers

McCumber pointed out in 1964 [4] that the electron-phonon interaction between the impurity ion and lattice may influence the lasing characteristics of a solid state laser. When this occurs the lasing ion's fluorescence spectrum usually has a sharp purely-electronic (zero-phonon) line accompanying adjacent sidebands due to phonon-assisted photon emission or absorption. These phonon-assisted sidebands have a rather broad fluorescence spectrum as was seen earlier in Fig. 44. Gain may occur in these sidebands and vibronic lasers will emit light at the wavelength where they have the highest gain. By incorporating tuning optics in the laser cavity, the cavity optics can be adjusted so only certain wavelengths can oscillate in the laser cavity and in this manner a vibronic laser can be tuned to various wavelengths within its gain bandwidth. This continual tunability is the property that makes vibronic lasers unique and important as a special class of solid state lasers.

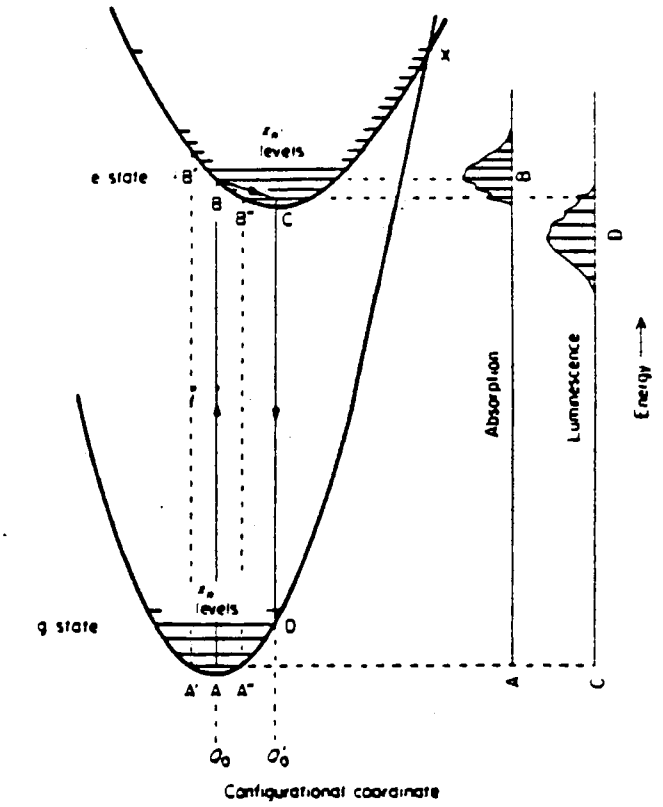

Figure 44. Configuration Coordinate Diagram Used to Analyze Transitions Between two Electronic States g and e (the theoretical shapes and energies of the absorption and luminescence transitions are shown to the right)

McCumber's theory considers two sets of energy levels that are in thermal equilibrium at temperature T. McCumber [77] and Neporent [78] obtained a relationship between the absorption cross section and the emission cross section by assuming that the entire multilevel system was in thermal equilibrium. Band and Heller [79] derived the same relationship by assuming only that the populations within both the ground and excited states are at the same temperature T. In their derivation the ground and excited state manifolds are not in thermal equilibrium with each other. Band and Heller showed that McCumber's relationship holds independent of state degeneracies or couplings or dipole matrix elements or nature of the potential energy surfaces or any other microscopic detail of the system. All that is required is microscopic reversibility and thermal equilibrium of the internal degree of freedom (at a common temperature T) within the optically coupled electronic states [78]. Their derivation proves that McCumber's and Neporant's equation describing the relationship between absorption and emission of multilevel systems in thermal equilibrium hold even for the case when the initial and final states are not in thermal equilibrium with each other. Band and Heller also showed that if more than one excited electronic state participates in the dynamics and if these electronic states are themselves in equilibrium with each other during the time scale of the fluorescence, then McCumber's relationship between absorption and emission does not hold. The relationship turns into a summation over the states at different temperatures and different populations. The remaining portion of this paper is the development and application of McCumber's theory for vibronic lasers.

McCumber has modeled lasers with a simple dielectric theory. In this theory, the active laser medium has a frequency-dependent gain over a finite bandwidth. The most important properties of the material in a small macroscopic neighborhood of the space-time point $(\vec{r},t)$ are reflected in the gain characteristic $g_\lambda(\vec{k},\omega;\vec{r},t)$. The indices $(\vec{r},t)$ are omitted in the remaining discussing when they are not relevant. The gain characteristic $g_\lambda(\vec{k},\omega;\vec{r},t)$ describes the gain per unit length at a certain point in time in space for radiation having

(1) frequency ω,

(2) wave vector parallel to the vector $\vec{k}$, and

(3) polarization index λ.

The polarization index ranges from one to three depending on if we are considering either π (E $\parallel$ c) or σ (E $\perp$ c) polarizations.

The gain coefficient of an active medium in the absence of any losses (e.g., scattering) can be described as the difference between the stimulated emission term $e_\lambda(\vec{k},\omega;\vec{r},t) = N_i\sigma_{i1}$ and the absorption coefficient of the pumped laser material $a_\lambda(\vec{k},\omega;\vec{r},t) = N_1\sigma_{1i}$:

$$g_\lambda(\vec{k},\omega;\vec{r},t) = e_\lambda(\vec{k},\omega;\vec{r},t) - a_\lambda(\vec{k},\omega;\vec{r},t) \quad (73)$$

$$= N_i\sigma_{i1} - N_1\sigma_{1i} \quad (74)$$

where N_i and N_1 are the total populations of the upper and lower states, respectively, and σ_{1i}, σ_{i1} are the cross sections for absorption and stimulated emission transitions at frequency ω. The absorption and stimulated emission cross sections are defined as the absorption or stimulated emission coefficient divided by the impurity ion population.

Experimental Technique

The direct measurement of the gain characteristic $g_\lambda(\vec{k},\omega)$ of an optically pumped material is very difficult to do accurately. The experimental setup for obtaining gain values is shown in Figure 45. A monochromatic "probe" beam of light passes through the medium as population inversion takes place. Population inversion is a condition needed for lasing to occur in a crystal and occurs when there are more ions in the excited state than in the "ground" state of the lasing transition. The probe beam transmission is observed while the material is being pumped and compared to the transmission when the material is unpumped for signs of an increase in the intensity indicating gain in the medium. The gain characteristic can be determined experimentally through

$$g(cm^{-1}) = \frac{[ln(G+1)]}{d}, \quad (75)$$

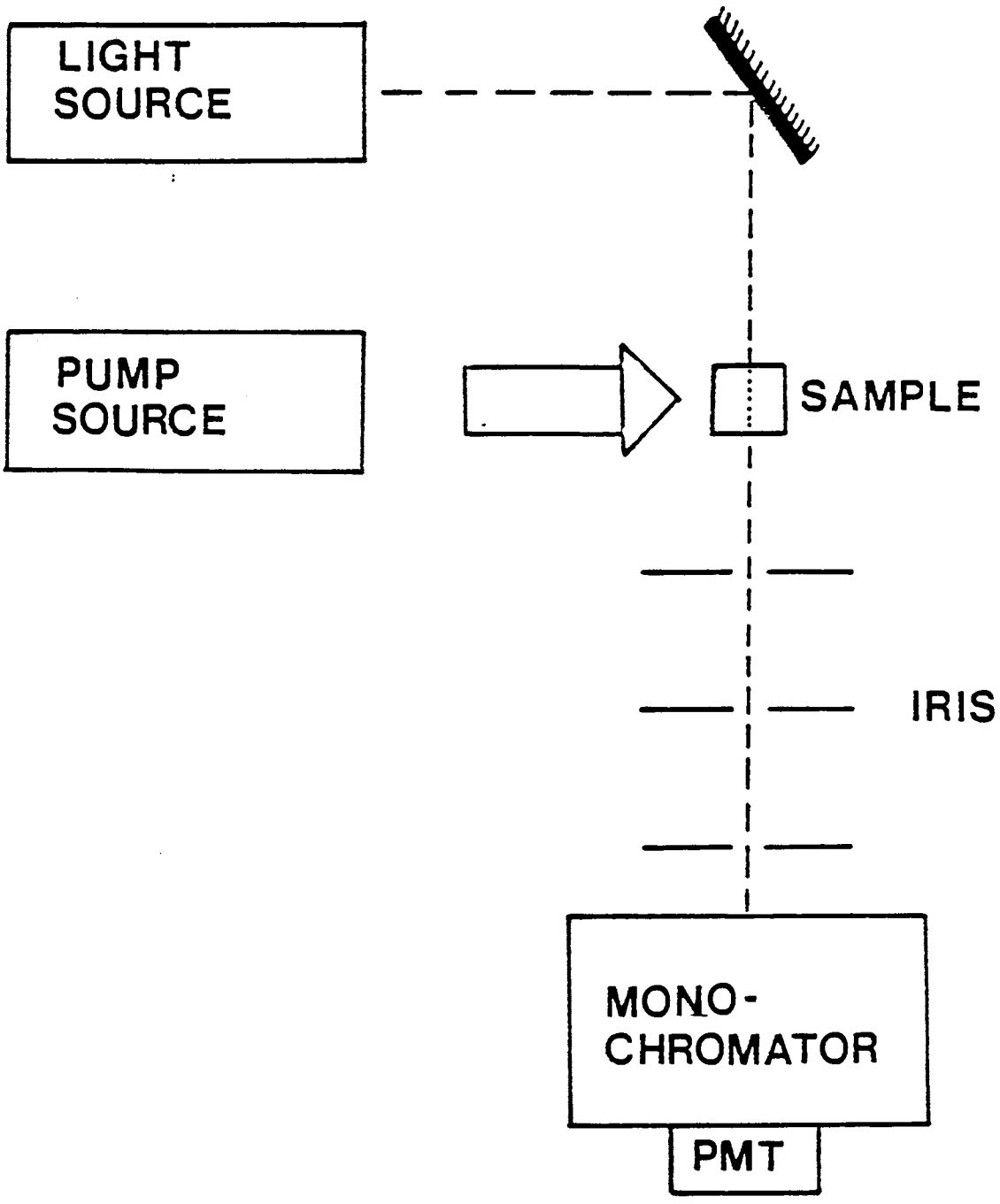

Figure 45. Experimental Set Up Used for Measuring Gain in a Laser Medium

where $G = \frac{(I_p - I_o)}{I_o}$. I_o is the intensity of the probe beam transmission passing through the unpumped material, I_p is the intensity of the probe beam transmission passing through the pumped material, and d is the thickness of the material. Any error in measuring the intensities is transmitted to the gain coefficient so it becomes of considerable importance to be able to relate the gain characteristic to the more accurately measured absorption and fluorescence spectra.

The greatest problem that arises when making gain measurements is the small signal appearing on a big background that is characteristic of these measurements. Since gain occurs in the fluorescence band of the laser medium, it is difficult to separate the fluorescence intensity from the intensity due to the gain of the probe beam of frequency ω passing through the material. In order to separate the gain intensity from the fluorescence intensity, a detector must be placed a large distance from the material with a set of irises along the path. A laser would be good to use as a probe beam because of its high directionality, but its monochromatic property limits the number of places in the fluorescence band that the gain can be experimentally measured.

Relationship Between the Gain and the Fluorescence and Absorption Spectra

McCumber considered a simple model for an insulating crystal that is lightly doped with impurity ions and that there is no Stoke's shift between the absorption and emission spectrum of the inpurity ions. The impurities have their energy levels grouped in two sets, as shown in Fig. 42. Each set has an energy spread on the order of the largest phonon energy. This phonon energy is approximately 10^3 cm^{-1} for oxides and 10^2 cm^{-1} for fluorides. The two sets are also separated by an optical energy of 10^4 cm^{-1}. The population of the upper state is N_2 and the population of the lower state is N_1. It is assumed that within the two sets that the distribution of the upper and lower state populations are described by a single-lattice temperature T. It is also assumed that the probability for nonradiative transitions between the two sets of levels is negligible in a radiative spontaneous emission lifetime and that the time for thermal equilibration within

each set is very short compared to that lifetime. This insures that the phonon processes do not play a role in depopulating the levels and that the sets of levels are also in thermal equilibrium.

The absorption, stimulated emission, and spontaneous emission transitions are connected by detailed-balance equations. Einstein [77,80] considered a simple two-state system and showed that when such a system is in thermal equilibrium with a radiation field, then the principle of detailed-balance leads to an expression for the spontaneous emission probability per unit time. If N_2 atoms are maintained in the upper level of a transition of frequency μ_{21}, then the number of spontaneous downward transitions per cm^3 per sec will be

$$N_{sdt} = N_2 A_{21} \tag{76}$$

where A_{21} is the Einstein coefficient of spontaneous emission. If radiation of intensity I_μ is present there will also be induced emissions. The number of induced emissions from level 2 to 1 is given by [81]

$$N_{ie} = N_2 B_{21} I_{\mu(21)} \tag{77}$$

where B_{21} is the Einstein coefficient for induced emission. The number of induced transitions from level 1 to 2 produced by the absorption of a photon by the atoms in the lower level is

$$N_{ia} = N_1 B_{12} I_{\mu(21)}. \tag{78}$$

Eqs. (77) and (78) have the same general form because both are stimulated processes. The mathematical expressions connecting these coefficients are

$$\sigma_{21} B_{21} = \sigma_{12} B_{12}, \tag{79}$$

$$A_{21} = B_{21}(\frac{\hbar \mu^3}{2\pi^2 c^2}), \tag{80}$$

where σ_{21} is the stimulated emission cross section and σ_{12} is the absorption cross section for the impurity ion.

The absorption and stimulated emission cross sections given in Eq. (79) are defined as

$$\sigma_{12} = \sigma_{a\lambda}(\vec{k}, \mu) = \frac{a_\lambda(\vec{k}, \mu)}{N_1}, \tag{81}$$

$$\sigma_{21} = \sigma_{e\lambda}(\vec{k}, \mu) = \frac{e_\lambda(\vec{k}, \mu)}{N_2}. \tag{82}$$

If the system is in equilibrium, then the rate of upward transitions is equal to the rate or downward transitions

$$N_{ia} = N_{sdt} + N_{ie} \tag{83}$$

$$N_1 B_{12} I_{\mu(21)} = N_2 A_{21} + N_2 B_{21} I_{\mu(21)}. \tag{84}$$

$$I_{\mu(21)} = \frac{A_{21}}{B_{21}[(\frac{\sigma_{12}}{\sigma_{21}})(\frac{N_1}{N_2}) - 1]}. \tag{85}$$

From a Boltzmann distribution

$$\frac{N_2}{N_1} = \exp(\frac{\hbar\mu}{k_B T}), \tag{86}$$

so

$$I_{\mu(21)} = \frac{A_{21}}{B_{21}[(\frac{\sigma_{12}}{\sigma_{21}}) \exp(\frac{\hbar\mu}{k_B T}) - 1]}. \tag{87}$$

The dependence of intensity upon frequency for blackbody radiation is given by the Planck formula [81]

$$I_{\omega(21)} = (\frac{\hbar\omega^3}{2\pi^2 c^2}) \cdot \frac{1}{\exp(\frac{\hbar\omega}{k_B T}) - 1}. \tag{88}$$

Using Eqs. (80) and (88), Eq. (87) can be rewritten as

$$\sigma_{12} = \sigma_{21} \exp[\frac{\hbar(\omega - \mu)}{k_B T}]. \tag{89}$$

Eq. (89) is the same relationship derived by Band and Heller. In the above expression $\hbar\mu$ is a weak temperature-dependent excitation potential. It fixes the scale factor connecting the two spectral functions. In a more physical sense, $\hbar\mu$ can be thought of as the net free energy required to excite the impurity while maintaining the initial lattice temperature T.

Rewriting Eq. (89) yields the expression

$$\frac{\sigma_{12}}{\sigma_{21}} = \exp \frac{\hbar(\omega - \mu)}{k_B T} \tag{90}$$

where $\exp(\frac{-\hbar\mu}{k_BT})$ equals the ratio $\frac{N_2^o}{N_1^o}$ where N_i^o is the population N at thermal equilibrium of the unpumped material.

In the limit of zero temperature for general systems and at arbitrary temperatures for simple "mirror-image" two level impurity systems, μ is equal to the frequency ω_o of the no-phonon line. In the above cases, $(\omega - \mu) = (\omega - \omega_o)$ is the frequency measured from the zero-phonon line and it is assumed that $\exp(\frac{\hbar\mu}{k_BT})$ can be approximated by $\exp(\frac{\hbar\omega_o}{k_BT})$ to a reasonable degree of accuracy.

By substituting Eq. (89) into (74), it is possible to obtain an expression describing Fig. 42.

$$g_\lambda(\vec{k},\omega) = \sigma_{21}N_2 - \sigma_{12}N_1, \tag{91}$$

$$g_\lambda(\vec{k},\omega) = \sigma_{21}N_2 - \sigma_{21}\exp[\frac{\hbar(\omega-\omega_o)}{k_BT}]N_1, \tag{92}$$

$$g_\lambda(\vec{k},\omega) = \sigma_{21}[N_2 - N_1\exp[\frac{\hbar(\omega-\omega_o)}{k_BT}]], \tag{93}$$

$$g_\lambda(\vec{k},\omega) = \sigma_{12}\exp[\frac{-\hbar(\omega-\omega_o)}{k_BT}]N_2 - \sigma_{12}N_1, \tag{94}$$

$$g_\lambda(\vec{k},\omega) = \sigma_{12}[N_2\exp[\frac{-\hbar(\omega-\omega_o)}{k_BT}] - N_1]. \tag{95}$$

Either Eq. (93) or Eq. (95) could be used to determine $g_\lambda(\vec{k},\omega)$, but Eq. (93) is of greater practical importance because the stimulated emission cross section σ_{21} can be readily inferred from the fluorescence spectrum.

In order to relate the stimulated emission cross section to the fluorescence spectrum, McCumber has introduced a dimensionless function $f_\lambda(\vec{k},\omega)$ as the fluorescence intensity in photons/sec per unit frequency interval of radiation of polarization λ and frequency ω. If τ is the spontaneous emission lifetime of an excited fluorescence center, then

$$\frac{1}{\tau} = \frac{1}{2\pi}\sum_\lambda \int_0^{4\pi} d\Omega \int_0^\infty f_\lambda(\vec{k},\omega)d\omega. \tag{96}$$

Dexter [60] has also related the stimulated emission cross section to the shape of the fluorescence spectrum. He began by first considering Einstein's model for the interaction of radiation with matter and then modifying this to describe the interaction of radiation with atomic systems embedded in a dielectric medium.

The expression for the Einstein A coefficient for dipole allowed transitions can be written as [60]

$$A_{21} = (\frac{1}{\tau})_{21} = \frac{4\omega_{21}^3}{3\hbar c^3} \cdot |r_{21}|^2 \tag{97}$$

As a function of energy, the emission probability can be written as

$$W_{21}(E) = \frac{1}{\tau} \cdot S_{21}^e(E) = \frac{4E_{21}^3}{3\hbar^4 c^3} \cdot |r_{21}|^2 S_{21}^e(E) \tag{98}$$

where $S_{21}^e(E)$ is the shape function of the emission line such that

$$\int_0^\infty S_{21}^e(E)dE = 1. \tag{99}$$

The emission cross section σ_e can be written as

$$\sigma_e(E) = \frac{4\pi^2}{3\hbar c} \cdot E_{21}|r_{21}|^2 S_{21}^e(E). \tag{100}$$

Eqs. (98) and (100) can now be modified for interaction of radiation with matter in a dielectric medium. The modifications become simple when (a) the relative transitions of the centers are not in resonant with transitions of the host medium, and (b) the impurities are so far apart in the medium that the interactions between impurities can be neglected. When these conditions occur then the prescence of other impurities can be ignored and each impurity ion can be considered as an isolated atom in the medium characterized by its (real) index of refraction and an "effective" field. In Eq. (100), the transition amplitude is proportional to the field at the impurity. Thus, the transition probability must be multiplied by $(\varepsilon_{eff}/\varepsilon_o)$, where ε_{eff} is the magnitude of the field effective in inducing the transition, and ε_o is the average field in the medium. The emission cross section is obtained by dividing the transition probability by the energy flux corresponding to one photon per unit volume, that is by $\epsilon_o \varepsilon_o^2 \nu/4\pi$. In this expression ϵ_o is the dielectric constant and ν is the velocity of the photons in the medium. In a transparent medium, $\epsilon_o = n^2, \nu = c/n$, and n is the (real) index of refraction, so for a dielectric medium the absorption cross section must be divided by n. Using the above corrections, Eqs. (98) and (100) can be modified by the presence of a dielectric medium as

$$W_{21}(E) = [(\frac{\varepsilon_{eff}}{\varepsilon_o})^2 n] \cdot \frac{4E_{21}^3}{3\hbar^4 c^3} \cdot |r_{21}|^2 S_{21}^e(E), \tag{101}$$

$$\sigma_e(E) = [(\frac{\varepsilon_{eff}}{\varepsilon_o})^2 \cdot \frac{1}{n}] \cdot \frac{4\pi^2}{3\hbar c} \cdot E_{21}|r_{21}|^2 S^e_{21}(E). \tag{102}$$

Combining Eqs. (101) and (102) yields

$$\sigma_{21} = W_{21} \cdot (\frac{\pi^2 c^2 \hbar}{\omega^2 n^2}). \tag{103}$$

The connection between $f_\lambda(\vec{k},\omega)$ and W_{21} is

$$W_{21} = (\frac{1}{2\pi\hbar}) \sum_\lambda \int_0^{4\pi} d\Omega_{k,\lambda} f_\lambda(\vec{k},\omega) \tag{104}$$

so it follows that

$$\sigma_{21}(\vec{k},\omega) = f_\lambda(\vec{k},\omega)[\frac{2\pi c}{\omega n_\lambda(\vec{k},\omega)}]^2. \tag{105}$$

where $n_\lambda(\vec{k},\omega)$ is the index of refraction of the laser material. Using Eq. (93) and Eq. (105), the expression for the gain characteristic in terms of the experimentally measurable fluorescence spectrum is

$$g_\lambda(\vec{k},\omega) = [N_2 - N_1 \exp[\frac{\hbar(\omega-\omega_o)}{k_B T}]] f_\lambda(\vec{k},\omega)[\frac{2\pi c}{\omega n_\lambda(\vec{k},\omega)}]^2. \tag{106}$$

The ω^{-2} factor in Eq. (106) causes an asymmetric narrowing of the gain curve compared to the emission band. If the absolute strength of the function $f_\lambda(\vec{k},\omega)$ is not measured directly, it can be estimated through Eq. (96) from the spontaneous emission lifetime. Let C_1 be the absolute strength of $f_\lambda(\vec{k},\omega)$. The integral $\int_0^\infty f_\lambda(\vec{k},\omega)d\omega = C_1 \cdot A$, where A is the integrated intensity of the fluorescence spectrum after the intensity has been normalized to one. As a first approximation assume that the fluorescence spectrum is not polarization dependent so that $\sum_\lambda = 3$. The integral $\int_0^{4\pi}$ of the solid angle $d\Omega$ is equal to 4π and is the integral over all real space. Using the above approximations, the absolute strength of $f_\lambda(\vec{k},\omega)$ can be determined from

$$C_1 = \frac{1}{6A\tau}. \tag{107}$$

C_1 can also be determined from a single-frequency calibration measurement of $g_\lambda(\vec{k},\omega)$ with known electronic populations in the two levels.

Threshold Properties of a Vibronic Laser

The fluorescence spectrum of $MgF_2 : Ni^{2+}$ (1%) for π- polarization is shown in Fig. 46. If it is assumed that the impurity levels other than the ground state and the excited state are negligibly occupied and that the excitation potential μ in Eq. (106) equals the frequency ω_o of the no-phonon line, then Eq. (106) can be used with the fluorescence spectrum of the material to compute the gain characteristic $g_\pi(\omega)$ for different values of the ratio $p_+ = \frac{N_2}{N_2+N_1} = \frac{N_2}{N}$, where N is the total number of impurity ions and p_+ is the population inversion at threshold of laser emission. Eq. (106) can be rewritten in terms of p_+ as

$$g_\lambda(\vec{k},\omega) = N[p_+ - (p_+ - 1)\exp[\frac{\hbar(\omega-\omega_o)}{k_BT}]]f_\lambda(\vec{k},\omega)[\frac{2c\pi}{\omega n_\lambda(\vec{k},\omega)}]^2. \qquad (108)$$

If the gain characteristic curve is known, it is possible by treating p_+ and μ as adjustable parameters and using the measured value of the fluorescence emission to fit Eq. (108) to the experimentally measured gain curves. A good fit is established when the predicted maximum in the calculated gain curve corresponds with the experimentally measured maximum gain in both location in magnitude [32].

If the total round trip cavity losses in $MgF_2 : Ni^{2+}$ are characterized for π-polarized radiation of frequency ω by the function $l_\pi(\omega) > 0$, and if L is the effective length of the gain region, then the condition for laser oscillation is when the gain begins to overcome the losses, or in other words,

$$Lg_\pi(\omega) = l_\pi(\omega). \qquad (109)$$

If the total cavity losses are frequency independent such that $l_\pi(\omega) = l$, then the operating frequency of the laser occurs, for a suitable excitation p_+, when the gain characteristic has its maximum value, $g_\pi(max) = \frac{l_\pi}{L}$. In Figure 47, the frequency $\omega_\pi(max)$ as a function of that gain for the $MgF_2 : Ni^{2+}(1\%)$ system at 77 K is plotted. As the value of the zero-phonon line is moved to a higher energy the theoretical gain curve shifts to a higher energy, the peak gain increases, and the slope of the calculated gain curve on the high energy side decreases. As

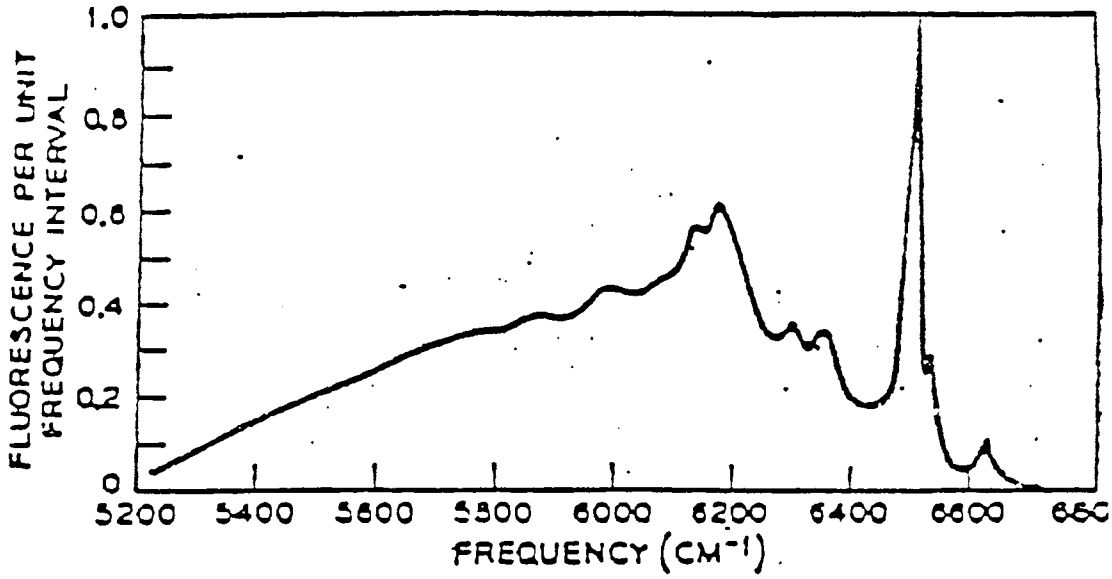

Figure 46. Fluorescence Spectrum of MgF_2:Ni^{2+} (1%) for π-Polarization

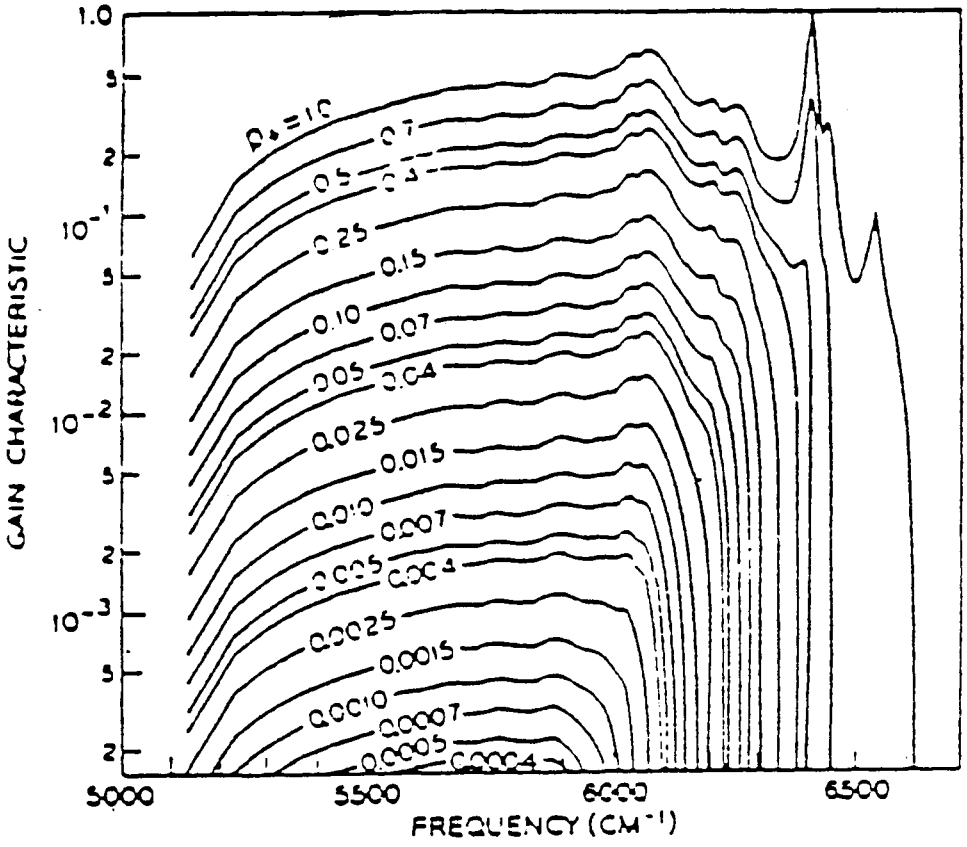

Figure 47. Gain Charactistic Versus ω for $MgF_2 : Ni^{2+}(1\%)$

the inversion parameter p_+ increases, the theoretical gain curve shifts to a higher energy, the peak increases, and the slope of the calculated gain curve on the high energy side increases. The slope of the gain curve on the low energy side does not change significantly with changes in either the inversion parameter or the location of the no-phonon line. The shift in $\omega_\pi(max)$ as $g_\pi(max)$ decreases can be better understood from Eq. (106). $g_\pi(\omega)$ is a monotonically increasing function of p_+. For $\hbar(\omega_o - \omega) \gg k_B T$, the factor $\exp[\hbar(\omega - \omega_o)/k_B T]$ in Eq. (106) is small. If for that case $N_2 \approx N_1$, the absorption term (N_1) in Eq. (106) will be much smaller than the emission term (N_2). However, if $N_2 \ll N_1$, then the two terms can be of comparable magnitude even if $\exp \frac{\hbar(\omega-\mu)}{k_B T}$ is small.

To find the crossover point of zero gain, set Eq. (106) equal to zero.

$$0 = [N_2 - N_1 \exp \frac{\hbar(\omega_{co} - \omega_o)}{k_B T}] f_\pi [\frac{2\pi c}{\omega n_\lambda}]^2, \tag{110}$$

$$0 = N_2 - N_1 \exp \frac{\hbar(\omega_{co} - \omega_o)}{k_B T} \tag{111}$$

$$\ln \frac{N_2}{N_1} = \frac{\hbar(\omega_{co} - \omega_o)}{k_B T} \tag{112}$$

$$\omega_{co} = \omega_o + [\frac{k_B T}{\hbar}] \ln \frac{N_2}{N_1} \tag{113}$$

This is important for lasers whose losses are small because their threshold populations N_2 will also be small.

The value for the gain in Eq. (108) is for vibronic lasers and can be modified for non-vibronic solid-state lasers. The definition for p_+ of $p_+ = \frac{N_2}{N}$ will remain the same and will appear in the definition for the gain. For non-vibronic systems, the gain will occur at the no-phonon line where $\omega = \omega_o$, $f_\lambda(\vec{k}, \omega)$ becomes the magnitude of the fluorescence at which gain occurs and $f_\lambda(\vec{k}, \omega)$ and $n_\lambda(\vec{k}, \omega)$ no longer have a strong frequency dependence. The gain for non-vibronic solid-state lasers becomes

$$g_\lambda = N f_\lambda [\frac{2\pi c}{\omega n_\lambda}]^2, \tag{114}$$

and using Eq. (105), Eq. (114) can be rewritten as

$$g_\lambda = N\sigma_{21}. \tag{115}$$

The gain will occur in non-vibronic lasers at the peak of the emission band.

The crossover-point for zero-gain occurs at the no-phonon line for non-vibronic lasers and is predicted in Eq. (113). At threshold for a non-vibronic laser, $N_2 = N_1$ and recalling that $\ln 1 = 0$, Eq. (113) reduces to

$$\omega_{co} = \omega_o. \tag{116}$$

Application of McCumber's Theory to the Alexandrite Laser

McCumber's theory has been modified to specifically describe the lasing characteristics of the alexandrite laser [76]. The three levels considered for room temperature operation of an alexandrite laser are the pump level ($^4T_1$) and the effective upper ($^4T_2$) lasing level and lower ($^4A_2$) ground state. At low temperatures lasing is due to the $^2E \rightarrow ^4 A_2$ transition and operates at the no-phonon line. The levels for the d^3 free ion are shown in the Tunabe-Sugano diagram in Fig. 48. The Tunabe-Sugano diagram plots the normalized energy state E/B versus the normalized crystal field strength Dq/B. The crystal field strength characterizes the strength of the coupling between the coulombic field of the lasing ion and the crystal field. The parameter B is the Racah parameter and represents the effect of electron-electron interactions. Defining ΔE as the difference between the energy of the $^4T_2$ and ^2E levels ($\Delta E = ^4 T_2 - ^2 E$), high crystal field is defined as (Dq/B)>2.3(ΔE >0), low crystal fields as (Dq/B)<2.3(ΔE <0), and "intermediate" crystal fields as (Dq/B) $\approx$ 2.3 ($\Delta E \approx 0$).

Figure 49 depicts the three different cases of ΔE in single configuration coordinate diagrams as they apply to the $^4T_2$, ^2E, and $^4A_2$ levels of chromium. For the case of a high crystal field there is a large degree of coupling of the lattice to the lasing ion and a seperation of the two upper levels. As a result only electronic transitions occur since the energy difference between the two excited states is

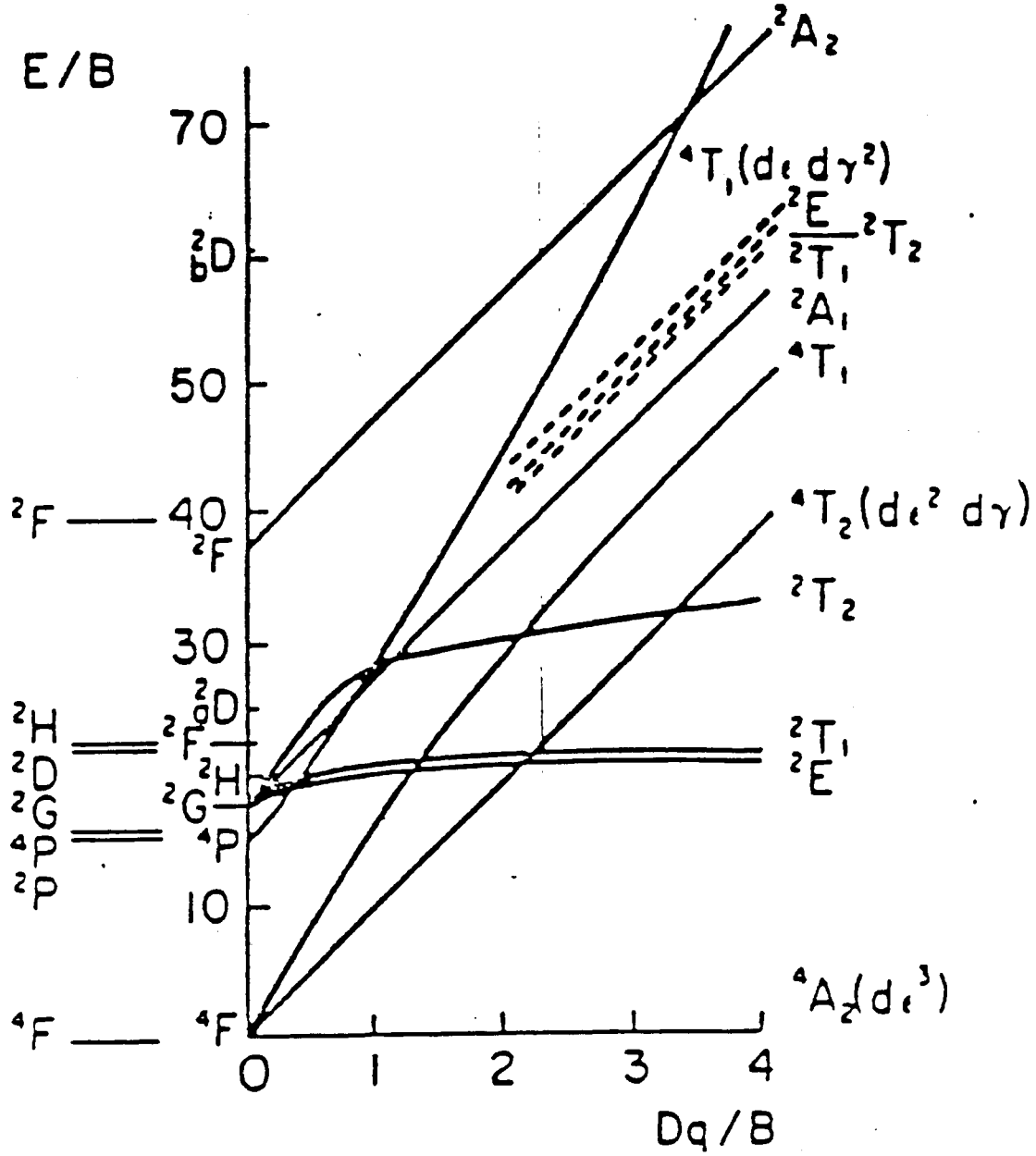

Figure 48. Tunabe-Sugano Diagram for Cr^{3+}

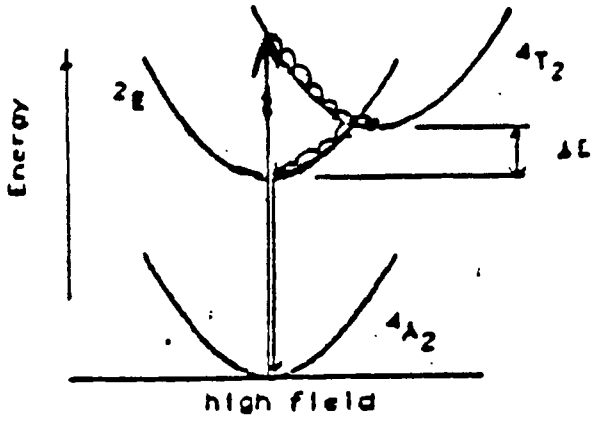

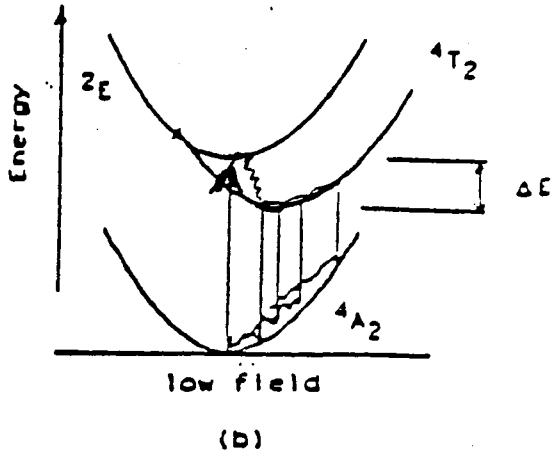

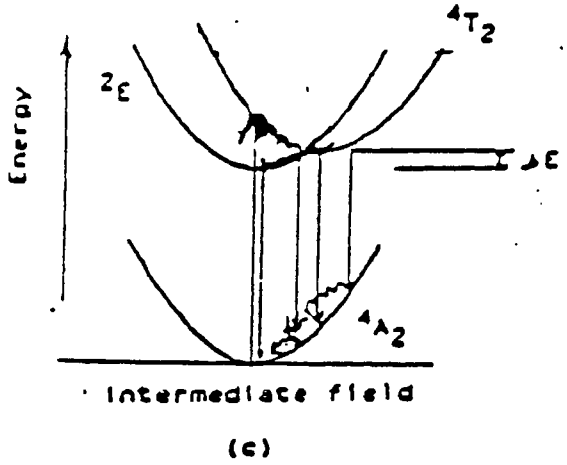

Figure 49. Single Configuration Coordinate Diagrams Depicting (a) High, (b) Low, and (c) Intermediate Crystal Field Energy Levels

sufficiently large enough so that no phonons can bridge the energy gap. In the low crystal field case the $^4T_2$ level lies below the ^2E level and zero phonon processes from the ^2E level are not observed and the fluorescence will exhibit the broad band vibronic emission. For the intermediate crystal field case, $\Delta E \approx 0$ and positive and the ^2E level lies just below the $^4T_2$ level. In this case there is relaxation into both the minima and the transitions between the ^2E and the $^4A_2$ ground state are between minima and are purely electronic. The transitions between $^4T_2$ and the ground state are vibronic transitions from the minima of $^4T_2$ to some excited vibrational state within $^4A_2$. The lifetime of $^4T_2$ is very short compared to ^2E and for sufficiently small ΔE, roughly 800 cm^{-1} in alexandrite, the ^2E level acts as a storage level to further populate the $^4T_2$ level via thermal energy to maintain Boltzmann distribution. As a result of these properties emission spectra show a zero-phonon line accompanied by broad vibronic emission at high temperatures and at low temperatures the system behaves as a three-level laser and operates at the zero-phonon line of the ^2E level.

The key assumption in applying McCumber's theory is that the population distribution within the metastable electronic manifold is in quasi-thermodynamic equilibrium during lasing (as it is during the measurement of the fluorescence spectrum). The relaxation time within this manifold is expected to be subnanosecond, making this assumption valid for laser pulse durations which are long compared to the relaxation time. A second important assumption is that the crystal field split components of the electronic ground state multiplet are nearly degenerate (within kT). This near degeneracy is necessary in order for the effective ground state absorption cross section to be derived from the emission cross section.

Figure 50 shows the fluorescence of alexandrite at 300 K. The phonon broadened spectral characteristics of vibronic laser materials can be seen to the left of the zero phonon lines ($\approx 14600 cm^{-1}$).

Generalizations to McCumber's theory can be made and the theory then applied to alexandrite. There are multiple, well separated upper electronic levels that contribute to the vibronic laser gain in alexandrite. The lower electronic

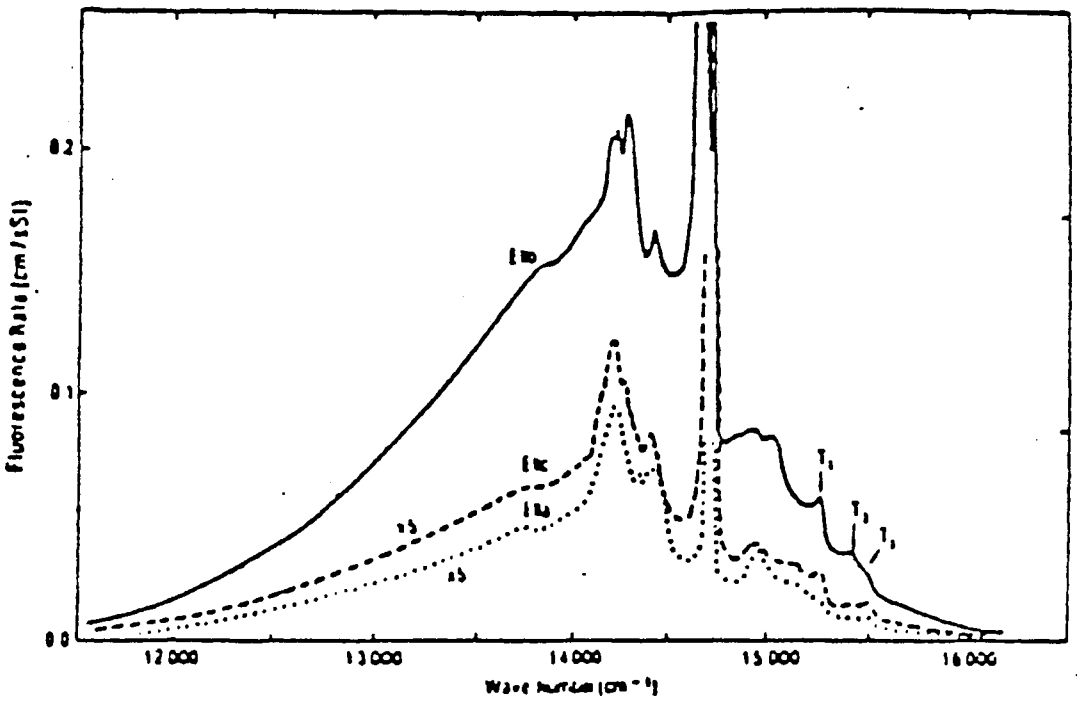

Figure 50. Fluorescence Spectra at 300 K of Cr^{3+} Ions in Alexandrite

level $^4A_2$ is split into four components that are unresolved at room temperature. Involved in the vibronic transition, therefore, is a set of upper electronic states j and a set of lower states i, the latter of which are essentially degenerate in energy.

The laser gain per unit length $g_\lambda(\vec{k}, E)$, for radiation with energy E, unit wave vector $\vec{k}$, and polarization λ, can be rewritten from Eq. (106) as

$$g_\lambda(\vec{k}, E) = \sum_{i,j}(N_j - N_i \exp^{[(E-\hbar\mu_{ji})/kT]} f^*_\lambda(\vec{k}, E)_{ji}[\frac{c^2h^3}{E^2n^2_\lambda(\vec{k}, E)}] \qquad (117)$$

where N_i and N_j are the average number of ions per unit volume that occupy that specific state, μ_{ji} is the chemical potential difference between the lower and upper states, and $\hbar\mu_{ji}$ is the net free energy required for a no-phonon excitation from the i^{th} to the j^{th} state. The function $f^*_\lambda(\vec{k}, E)_{ji}$ is the total emission rate that photons of polarization λ are emitted in a unit solid angle about $\vec{k}$, per unit energy E, as a result of an electronic state change from j to i. Both vibronic and no-phonon transitions are included in this function. The transition rate $f^*_\lambda(\vec{k}, E)_{ji}$ is related to an effective stimulated emission cross section $\sigma_{e\lambda}(\vec{k}, E)_{ji}$ by rewriting Eq. (105) as

$$\sigma^*_{e\lambda}(\vec{k}, E)_{ji} = f^*_\lambda(\vec{k}, E)_{ji}\frac{h^3c^2}{E^2n^2_\lambda(\vec{k}, E)}. \qquad (118)$$

In the event that the j^{th} states are in quasi-thermodynamic equilibrium with one another and the ground states are all degenerate, it is possible to derive a simpler expression for g_λ. Under these assumptions, the population of the j^{th} state is given by

$$N_j = \frac{N^* exp(-E_{jg}/kT)}{\sum_j exp(-E_{jg}/kT)}. \qquad (119)$$

Here, N^* is the total concentration of excited-state ions and i=g for all j. This is based on the assumption of ground state degeneracy.

By carrying out the summations indicated in Eq. (117) and by letting N be the total ion concentration, the gain assumes the simplified form

$$g_\lambda(\vec{k}, E) = [N^* - (N - N^*)\exp[(E - E^*)/kT] \cdot f^*_\lambda(\vec{k}, E)_{ji}[\frac{c^2h^3}{E^2n^2_\lambda(\vec{k}, E)}]. \qquad (120)$$

In the above equation, E^* is an effective no-phonon level and is equal to 14698 cm−1 at 300 K for alexandrite. f_λ^* is given by

$$f_\lambda^* = \frac{\sum_{ji} f_\lambda(\vec{k}, E)_{ji} exp(-E_{jg}/kT)}{\sum_j exp(-E_{jg}/kT)}, \tag{121}$$

where the right-hand side represents the summation of the fluorescence rate between indvidual electronic levels (and the associated individual sidebands) weighted accordingly to the Boltzmann occupation probability function.

The measured fluorescence spectrum is proportional to $f_\lambda^*(\vec{k}, E)$ and can be determined from the radiative lifetime τ by the relation

$$\frac{1}{\tau} = \frac{8\pi}{3h} \sum_\lambda \int_0^\infty dE f_\lambda^*(\vec{k}', E) \tag{122}$$

where $\vec{k}'$ is perpendicular to the λ component of the electric field vector. This expression, as written, is valid for pure electric dipole emission, which has been observed to be strongly dominant in the alexandrite room-temperature vibronic spectrum.

The above relations allow the laser gain to be computed from the measured values of fluorescence lifetime, quantum yield, and electronic energy levels. It is not necessary, therefore, to know how much each electronic energy level contributes to vibronic lasing or the number of vibrational quanta emitted in order to calculate the laser gain. The effective emission cross section in the vibronic mode as determined from the theory is presented in Fig. 51 as a function of temperature.

The increase in effective emission cross section and, hence, the laser gain with temperature, is caused by a thermally induced increase in the occupation probability of the $^4T_2$ levels compared to the lower lying metastable ^2E levels. Since these upper states provide a major contribution to the vibronic laser gain, a strong, positive temperature dependence of gain occurs.

The intrinsic laser gain from Eq. (120) has been plotted in Fig. 52 for several values of $p^+ = N^*/N$. Excluded from this computation are losses attributed to sources other than ground-state vibronic absorption, such as excited-state absorption and scattering losses which may be present. An increase in the operating

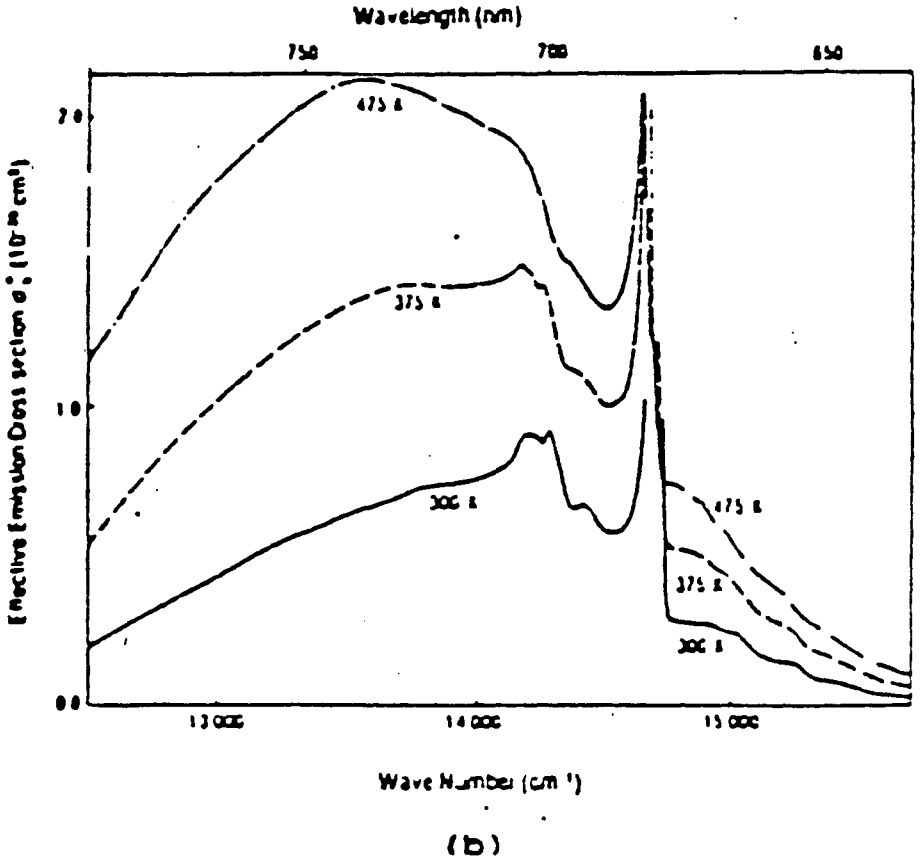

Figure 51. Effective Stimulated Emission Cross Section Versus Wavelength and Temperature

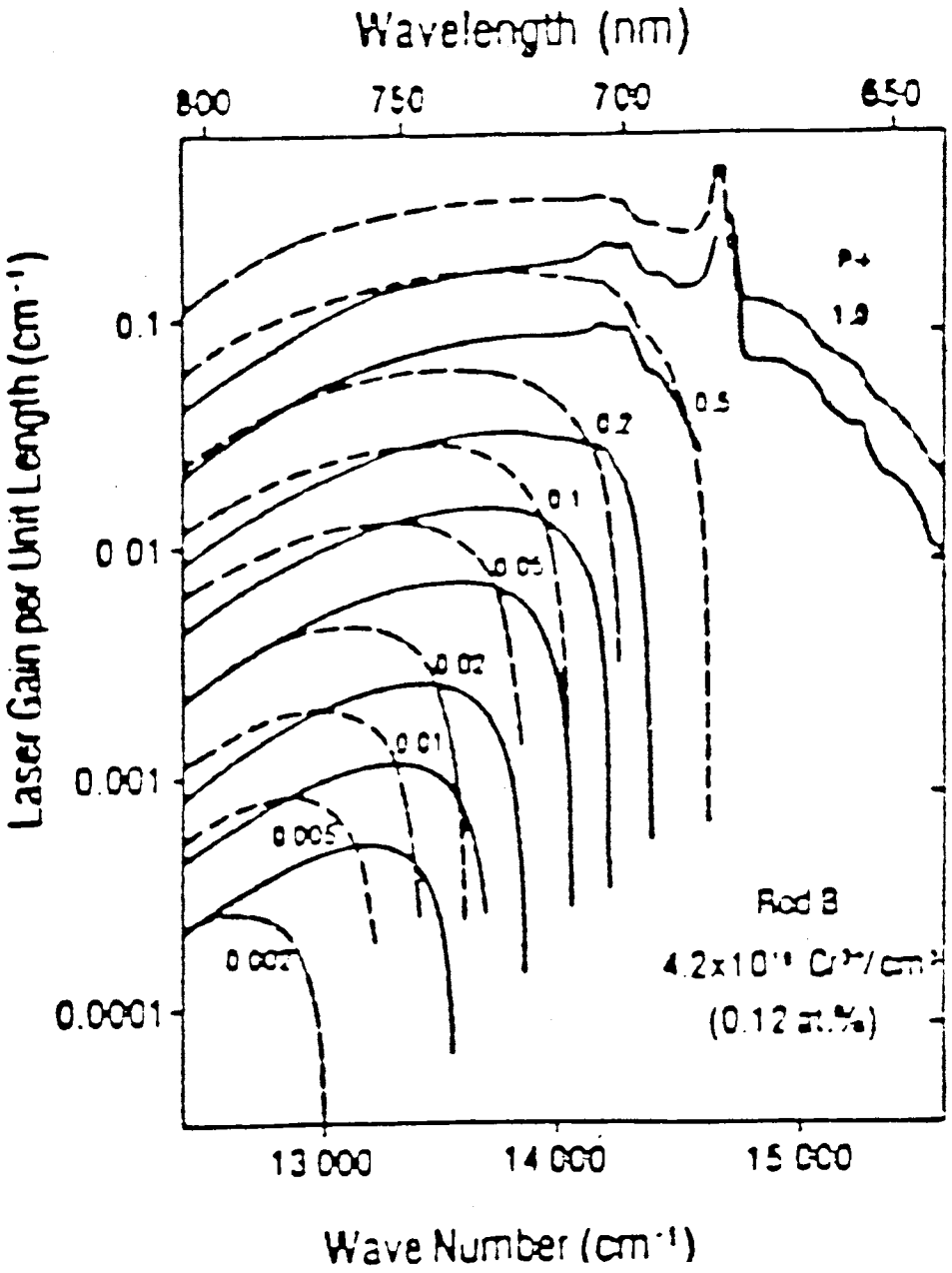

Figure 52. Alexandrite Lasing Gain Computed from Eq. 120
(solid lines are for 25°, dashed lines for 75° C)

temperature causes the free-running laser wavelength, which occurs at the gain peak, to shift to the red as Fig. 52 illustrates. There are three contributions to the red shift. One is the increased phonon population with temperature which reduces the effective population inversion at the shorter wavelength. This is manifest in the explicit temperature dependence of Eq. (120). A second contribution is the shift of the no-phonon lines with temperature and the enhancement of the long wavelength vibronics. Finally, a third contribution is the reduction with temperature of the excitation level required to reach threshold that is a result of the fact that the laser gain has increased. The result of this reduction in the threshold excitation level is the increased ground-state population and associated increased ground-state absorption which shifts the laser gain curve to the red.

The cross section for excited-state absorption subtracts from the stimulated emission cross section. Thus, if the excited state absorption cross section equals or exceeds the emission cross section, no gain can occur regardless of the excitation level. It is necessary, therefore, to determine the excited state absorption in order to compute the laser gain correctly. This cross section can be inferred from the laser performance characteristics.

Importance and Use in Field

As shown in the previous section it is possible using McCumber's theory to describe the gain and model the operation of a 1% $Ni2+$ MgF_2 laser and an alexandrite laser. Errors can be introduced in the analysis when such things as different valences of the impurity ion (as is the case for Ti^{4+} in Sapphire) or ESA (as is the case for alexandrite) change either the absorption or fluorescence spectra. These effects can be identified with an extension of the previous theory.

Equations (82) and (89) can be combined to give the absorption coefficient in terms of the concentration and the stimulated emission cross section,

$$\alpha = N_1 \sigma_{21} \exp\left[\frac{\hbar(\omega - \mu)}{k_B T}\right] \tag{123}$$

For materials with a large Stokes shift between the absorption and emission band, the stimulated emission cross section is given by [32]

$$\sigma_{21} = [\frac{1}{4\pi^2 \tau_R \Delta\nu}](\frac{\lambda_{em}}{\lambda_{ab}})[\frac{g_\mu}{g_l n_{ab} n_{em}}](\frac{|M_{ab}|}{|M_{em}|})^2(\frac{\epsilon_{em}}{\epsilon_{ab}})^2 \tag{124}$$

where λ_{em} is the wavelength of the peak of the emission band and λ_{ab} is the wavelength of the peak of the absorption, $\Delta\nu$ is the full width at half-maximum of the absorption band, n_{em} and n_{ab} are the indices of refraction of the material at emission and absorption, respectively, τ_R is the radiative lifetime of the material, g_μ and g_l are the degeneracies of the upper and lower levels of the transition, ϵ_{em} and ϵ_{ab} are the effective fields surrounding the ion in the host at the wavelengths of the emission and absorption transitions, and M_{ab} and M_{em} are the matrix elements of the emission and absorption transitions. For zero-phonon lines, $\lambda_{ab} = \lambda_{em}$ and Eq. (124) becomes the familiar expression for the emission cross section [1]. Even with no zero-phonon lines, Eq. (124) can be used to obtain an estimate for σ_{21} by approximating the radiative lifetime by the measured fluorescence lifetime, approximating the halfwidth of the absorption band by the measured halfwidth of the emission band, assuming that the effective fields, refractive indices, and matrix elements are the same for absorption and emission wavelengths, and assuming that the degeneracies of the upper and lower levels of the transition are equal. Making these assumptions, Eq. (123) becomes

$$\alpha = \frac{N_1 \lambda_{em}^3}{4\pi^2 n^2 \lambda_{ab} \Delta\nu \tau_f} \exp[\frac{\hbar(\omega - \mu)}{k_B T}] \tag{125}$$

Knowing only the emission spectra and lifetime, and sample parameters, it is possible to calculate the shape of the absorption curve using Eq. (125). If the radiative lifetime of the transition is not known, then Eq. (105) can be combined with Eq. (125) to give

$$\alpha = N_1 f[\frac{2\pi c}{\omega n}]^2 \exp[\frac{\hbar(\omega - \mu)}{k_B T}] \tag{126}$$

Both Eq. (125) and Eq. (126) allow for the absorption to be determined from the emission.

It is also possible to determine the shape of the emission spectrum from the absorption spectra. Equation (126) can be rewritten in terms of the absorption coefficient as

$$f = (\frac{\alpha}{N_1})[\frac{\omega n}{2\pi c}]^2 \exp^{-\hbar(\omega-\mu)/kT} \tag{127}$$

As mentioned earlier, the value of Eqs. (126) and (127) comes in determining any unusual features in either the absorption or emission spectra.

Summary

A simple dielectric theory has been developed by McCumber to describe the gain curve of phonon-terminated lasers. The expression derived by McCumber to related the absorption cross section to the stimulated emission cross section need only assume that there is no Stoke's shift between the absorption and emission spectrum and that the ground state and excited state manifolds are in thermal equilibrium with themselves. Two vibronic lasers, MgF_2:Ni^{2+} and alexandrite, can be predicted with McCumber's theory to a good degree of accuracy. By extending McCumber's theory, unusual features in either the absorption or emission can be determined from the emission or absorption spectra, respectively.

VITA 2

MICHAEL L. KLIEWER

Candidate for the Degree of

Doctor of Philosophy

Thesis: INVESTIGATION OF THE DYNAMICS OF SOLID-STATE LASER CRYSTALS

Major Field: Physics

Biographical:

Personal Data: Born in Lincoln, Nebraska, May 21, 1960, the son of Donald L. and Edna M. Kliewer.

Education: Graduated from Putnam City High School, Oklahoma City, Oklahoma, in May, 1978; attended Oklahoma State University and received the Bachelor of Science Degree in May, 1983, with a major in Mechanical Engineering; completed the requirements for the degree of Master of Science at Oklahoma State University in May, 1986; completed the requirements for the degree of Doctor of Philosophy in Physics at Oklahoma State University in December, 1989.

Professional Experience: Graduate Teaching Assistant, Oklahoma State University, August, 1983 to May, 1984; Graduate Research Assistant, Oklahoma State University, January, 1986 to Present; Scientist, Spectra Technology, May, 1986 to August, 1986; Consultant, Solidlite Corporation, January, 1986 to Present; Member of the American Physical Society, Optical Society of America, National Society of Professional Engineers, and Sigma Pi Sigma.